Understanding LeTID degradation : a DFT study of point defects in silicon.

Elisa Tejeda Zacarias

INSTITUT POLYTECHNIQUE DE PARIS

NNT : 2023IPPAX036

Thèse de doctorat

Understanding LeTID degradation: a DFT study of point defects in silicon

Thèse de doctorat de l'Institut Polytechnique de Paris
préparée à École Polytechnique,

École doctorale n°626 École doctorale de l'Institut Polytechnique de Paris (EDIPP)
Spécialité de doctorat : Physique de la matière condensée

Thèse présentée et soutenue à Palaiseau, le 14/04/2023, par

ELISA TEJEDA ZACARIAS

Composition du Jury :

Claudine Crépin-Gilbert Directrice de recherche, Université Paris-Saclay (UMR 8214)	Présidente
Thierry Belmonte Directeur de recherche, Université Lorraine (7198)	Rapporteur
Khaled Hassouni Professeur des universités, Université Sorbonne Paris Nord (CNRS-UPR 3407)	Rapporteur
Anne Hemeryck Chargée de Recherche, Laboratoire d'analyse et d'architecture des systèmes (UPR 8001)	Examinatrice
Holger Vach Directeur de recherche, École Polytechnique (UMR 8214)	Directeur de thèse
Philippe Baranek Dr. Ingénieur-Chercheur, EDF R&D	Co-encadrant de thèse

Abstract

Currently, the research and development of photovoltaic technologies that improve both their efficiency and production cost are priorities for the solar industry. In particular, a significant amount of research is focused on the aging mechanisms of solar panels, which have a major impact on their efficiency and durability. Decrease in their performance can be directly related to different degradation mechanisms coming from the exposure of solar cells into weather changes, ambient conditions, or the aging of the components.

Silicon is, by far, the most common semiconductor material used in solar cells, representing approximately 90%of the modules sold today. One of the main causes of the decrease in performance of silicon-based panels that remains to be understood is related to light and temperature induced degradation (LeTID). This phenomenon appears after several months of use and can be responsible for up to a 16% reduction in cell efficiency.

Experimental studies show that various defects in silicon, such as metal impurities and hydrogen, are involved in the mechanisms underlying LeTID. In particular, the study of the dependence of lifetime on wafer thickness has provided valuable insights into the diffusion coefficients of impurities implicated in LeTID. Notably, the diffusion coefficients of common impurities in silicon modules, such as hydrogen, cobalt, and nickel, were determined to fall within the same range. This observation suggests that these defects potentially contribute to the degradation associated with LeTID. Nevertheless, LeTID has also been identified in high-purity silicon materials, indicating that it may be induced by intrinsic silicon defects including vacancies or self-interstitial silicon atoms.

While experimental studies have revealed the involvement of impurities, such as hydrogen, metal impurities, and self-Si defects, in the mechanisms underlying LeTID, their specific contributions remain poorly understood. This problematic arises due to the complexity of predicting the interaction of these defects with charge carriers in large-scale silicon systems, which is essential for a comprehensive understanding of the LeTID degradation phenomenon. Experimentally, it is extremely complicated to measure the structural and electronic properties of these defects when they are isolated, leading to an important lack of information about their characterization properties and the exact influence they have in charge carrier recombination within different silicon materials.

In this context, theoretical atomic methods, based on the first-principles of quantum mechanics calculations such as DFT, can retrieve the quantum electronic interactions of these defects and therefore represent powerful tools to try to understand this degradation at the nano-scale. By analyzing the stability and impact of hydrogen, silicon vacancies, silicon interstitial silicon as well as metallic impurities (such as Ni and Co) on the properties of silicon, this study proposes a theo-

retical approach, based on the use of hybrid functionals, to model the precursor mechanisms of LeTID.
It suggests that that hydrogen-bonded impurities can act as recombination centers that characterize LeTID. In addition, it is shown that interstitial hydrogen-bonded nickel and cobalt can induce LeTID, providing valuable insights into the dynamics of this type of aging. The approach proposed in this work offers the possibility to improve the strategies for inhibiting this type of degradation and to identify the risks of LeTID under different operating conditions.

Résumé

Actuellement, la recherche et le développement de technologies photovoltaïques qui améliorent à la fois leur efficacité et leur coût de production sont des priorités de l'industrie solaire. En particulier, une part non négligeable des études portent sur les mécanismes de vieillissement des panneaux solaires qui ont un impact déterminant sur leur efficacité et durabilité. La diminution de leur performance peut être directement liée à différents mécanismes de dégradation résultant de l'exposition des cellules solaires aux changements climatiques, aux conditions ambiantes ou au vieillissement des composants.

Le silicium est de loin le matériau semi-conducteur le plus couramment utilisé dans les cellules solaires, représentant environ 90

Les études expérimentales montrent que divers défauts dans le silicium, tels que les impuretés métalliques et l'hydrogène, sont impliqués dans les mécanismes sous-jacents au phénomène de dégradation LeTID. En particulier, l'étude de la dépendance de la durée de vie en fonction de l'épaisseur de la cellule solaire a fourni des perspectives précieuses sur les coefficients de diffusion des impuretés impliquées dans le LeTID. Notamment, les coefficients de diffusion des impuretés courantes dans les modules en silicium, tels que l'hydrogène, le cobalt et le nickel, ont été déterminés dans la même plage de coefficients de diffusion. Cette observation suggère que ces défauts pourraient potentiellement contribuer à la dégradation associée au LeTID. Néanmoins, le LeTID a également été identifié dans des matériaux en silicium de haute pureté, indiquant qu'il pourrait être induit par des défauts intrinsèques du silicium, notamment des lacunes ou des atomes de silicium auto-interstitiels.

Bien que des études expérimentales montrent que différents défauts dans le silicium, tels que l'hydrogène, les impuretés métalliques et les défauts intrinsèques du Si, sont impliqués dans les mécanismes sous-jacents au LeTID, leurs contributions restent encore mal comprises. Ce problème découle de la complexité de prédire l'interaction de ces défauts avec les porteurs de charge dans des systèmes en silicium à grande échelle, ce qui est essentiel pour une compréhension complète du phénomène de dégradation LeTID. Expérimentalement, il est extrêmement compliqué de mesurer les propriétés structurelles et électroniques de ces défauts lorsqu'ils sont isolés, entraînant un manque important d'informations sur leurs propriétés de caractérisation et l'influence exacte qu'ils exercent sur la recombinaison des porteurs de charge dans différents matériaux en silicium.

Dans ce contexte, les méthodes atomiques théoriques, basées sur les premiers principes de la mécanique quantique de type DFT, représentent des outils intéressants pour essayer de comprendre cette dégradation aux niveaux nano et microscopiques. En analysant la stabilité et l'impact de l'hydrogène, des lacunes du silicium, du silicium interstitiel ainsi que des impuretés métalliques

(telles que Ni et Co) sur les propriétés du silicium, cette étude propose une approche théorique, basée l'utilisation de fonctionnelle hybride, afin de modéliser les mécanismes précurseurs de la LeTID. Elle suggère que les impuretés liées à l'hydrogène peuvent agir comme des centres de recombinaison caractérisant la LeTID. En outre, il est démontré que le nickel et le cobalt interstitiels liés à l'hydrogène peuvent provoquer la LeTID, ce qui donne des indications précieuses sur la dynamique de ce type de vieillissement. L'approche proposée dans ce travail offre la possibilité d'améliorer les stratégies d'inhibition de ce type de dégradation et d'identifier les risques de LeTID dans différentes conditions d'exploitation.

Acknowledgments

After these three years of research (and mostly questions), I would like to express my gratitude to all the people who have crossed my path and contributed to my growth during this journey.
First and foremost, I want to thank Philippe Baranek, who provided me with invaluable guidance and technical expertise throughout my PhD. I am particularly grateful because he always showed interest in my work and was always willing to discuss about it. I would also like to thank Holger Vach for his scientific insights regarding my PhD work, for sharing his contagious excitement about research with me and for all his support. Our engaging discussions have been a source of joy and enrichment during these years. ¡Muchas amistades!
I am deeply thankful to all members of the jury as well as for their keen interest in my research, which has motivated me to excel in my work.
I wish to express my gratitude as well to all my friends at IPVF and beyond. Our talks, laughs, and coffee breaks have been an integral part of my scientific journey. I am grateful for the support and encouragement that I have received from all of you, whether it was related to my research or not. You hold a special place in my heart and memories.
Last but not least, I want to thankk my parents who have been a source of inspiration, they encouraged me to get to know the world and it is thanks to them that I love sciences and physics.
I want to thank the ANRT (French national association for research and technology) for its financial support within the CIFRE agreement 2019/1185 (industrial convention for training through research)

TABLE OF CONTENTS

Introduction

EDF R&D and IPVF (Institut Photovoltaque d'Ile de France) are engaged in the research and development of novel components for various photovoltaic (PV) technologies. Their primary objective is to enhance the performance and cost-effectiveness of PV technologies. Though the development of new materials that can more efficiently convert sunlight into electrical power is one of the key priorities, it is equally essential to gain a comprehensive understanding of the reliability and lifetimes of the already operational technologies.

Reliability and lifetimes of solar technologies are closely related to the electrical and chemical properties of semiconductors. The type of dopants and defects introduced or formed during the synthesis of materials have a profound impact on these properties [1]. These defects are difficult to characterize experimentally and are the source of numerous metastabilities that will strongly degrade the efficiency and durability of solar cells [2]. The understanding of these different effects is thus necessary for the optimization and improvement of materials for photovoltaics.

One of the research areas being pursued at IPVF is the investigation of the degradation of photovoltaic materials using both theoretical and experimental methods. Specifically, one of the subjects of study is the degradation of silicon-based modules as the PERC (Passivated Emitter Rear Cells) type. Indeed, silicon is the most common semiconductor material used in solar cells, accounting for approximately 90% of module sales today. The aging of these modules is a significant issue, with accelerated degradation impacting up to 15% of the modules within 6 to 12 months of operation and resulting in a decrease in their performance of several percent.

Changes in the performance can be related to different degradation mechanisms coming from the exposure of solar cells into weather changes, ambient conditions, or the aging of the components. The degradation mechanisms can be categorized as intrinsic or extrinsic. Extrinsic mechanisms are caused by the infiltration of external substances, such as air, oxygen, or water, and include corrosion and cracking cells. Intrinsic mechanisms regard changes in the structures of the interfaces between layers or within the bulk material.

Light and elevated temperature induced degradation (LeTID) is one of the most common intrinsic degradation mechanisms occurring in almost all types of silicon-based photovoltaic devices and is observed in solar cells exposed to working conditions in the long-term. LeTID is an important issue responsible for the reduction of PERC efficiency, which may lead to up to 16% relative performance losses in multicrystalline silicon solar cells. This process significantly impacts the conversion efficiency and stability of solar modules, resulting in an increased cost of electricity generated by solar cells. Despite having been initially observed a decade ago, the underlying mechanisms of this degradation are still not well understood.

Experimental studies have suggested that metallic impurities coming from the synthesis of the sil-

icon material, or hydrogen in the solar cell might be the cause of LeTID. In particular, hydrogen plays an important role in LeTID as it can passivate a variety of defects in solar cells, but excessive hydrogen may also cause hydrogen-induced defects and cause LeTID. PERC solar cells are easily affected by LeTID in industrial production. First of all, choosing suitable starting materials and choosing suitable doping materials in the manufacture of solar cells have an important influence on LeTID. Using gallium doped silicon can reduce boron-oxygen defects and is a way to inhibate LeTID. Secondly, it is also very important to control the hydrogen contained in the solar cell and remove excess impurities. Phosphorus gettering can reduce impurities in solar cells and reduce LeTID. Using proper post-processing methods can reduce LeTID. Light, current injection or annealing in the dark can effectively reduce LeTID. Even if the LeTID extent can partially be controlled by these mitigation strategies, a better understanding of the most fundamental mechanisms of LeTID is needed to mitigate it to the greatest possible extent and to be able to prevent LeTID in upcoming solar technologies.

In order to comprehend the mechanisms underlying the LeTID in silicon, it is imperative to understand the electronic properties and stability of silicon vacancies, self-silicon defects, hydrogen, and metallic impurities. Due to the complexity of measuring the structural and electronic properties of these defects when they are isolated, there is a significant lack of information regarding their characterization properties and their influence on charge carrier recombination within different silicon materials. Atomistic modeling is an powerful tool to study this issue because ab initio models, such as density functional theory (DFT), can retrieve the quantum electronic interactions of these defects. This work proposes to analyze the electronic interactions and stability of point defects in crystalline silicon using a DFT approach, and to deepen the understanding of the dynamic evolution of these defective structures with respect to available experimental information. Despite previous ab initio studies that have addressed the issue of hydrogen, self-silicon defects, and metallic impurities, a first-principles analysis to understand the complete LeTID mechanism has not yet been presented.

The present thesis begins with an introduction of the basics physics fundamentals to understand LeTID in Chapter 1. This chapter discusses how solar cells work, covering from charge carrier generation to their extraction and current production, the different types of solar cells, and what causes them to degrade. Finally, the chapter gives insight into LeTID, including the most important hypotheses and strategies to prevent it.

In Chapter 2 a brief methodological background to understand the basics of DFT simulations is presented, followed by the methodological aspects of our simulations. Although several *ab initio* studies have addressed the problem of hydrogen, self-silicon defects, and metallic impurities, they present important inconsistencies among each others in the description of the thermodynamic and electronic properties of such defects. We attribute these inconsistencies to the choice of the Hamiltonian and correction scheme adopted to compensate for the drawbacks of the DFT methodology. Such corrections are often not clearly described and include fitting the simulated results to the experimental values in an inconsistent and unjustified manner. To compare our results with those of previous studies and evaluate their differences, the correction scheme considered in our calculations is presented in detail in the last section of Chapter 2.

In Chapter 3 the electronic and structural properties of hydrogen, silicon vacancies, and self-

silicon interstitial atoms are analyzed in order to corroborate their role in LeTID. First, hydrogen-induced recombination is studied. It requires the analysis of hydrogen as a monoatomic impurity in its three different charge states: H^+, H^0, and H^-, along with the case of hydrogen as a diatomic molecule, which can be found in two forms, as H_2 or as a dissociated H_2^* molecule. Subsequently, single silicon vacancies and interstitial silicon defects are analyzed. Similarly, to understand the role of the single vacancy V and self-interstitial Si_i in LeTID degradation, and their different charge states are considered.

With the objective of substantiating the hypothesis that metal-hydrogen complexes are responsible for LeTID, the study of nickel and cobalt impurities and their respective hydrogen complexes is addressed in Chapter 4. In the first part of the chapter, an analysis of metals in both interstitial and substitutional positions is presented. Subsequently, different cases of metal-hydrogen complexes are analyzed. Finally, to investigate the potential diffusion of metal-hydrogen complexes towards grain boundaries or interfaces, the study was extended to consider three different types of simple dislocations: simple dislocations, dislocation edges, and twin-type grain boundaries.

Th concluding chapter summarizes the outcomes of this research along with a proposition regarding the dynamics of LeTID, involving both hydrogen and metallic impurities. This chapter also outlines the potential industrial applications and prospects of this investigation.

CHAPTER 1

Understanding LeTID in silicon modules

In a world where daily life requires more and more electrical energy, the seek of energy sources that are cleaner than oil and gas has become of great importance. Nowadays, different technologies are applied as renewable energies, offering the possibility to reduce the energy consumption coming from non-green sources. Among them, photovoltaic technologies hold an important place in the renewable energy market. In 2022, 5.2% of the European electricity generation came from photovoltaic devices, which placed it as the third-largest renewable electricity technology behind hydropower and onshore wind [3].

Silicon is, by far, the most common semiconductor material used in solar cells, representing approximately 90% of the modules sold today. Their high efficiencies and low cost of the components makes them highly demanded. But, in the quest of high-performance photovoltaic modules, the development of new materials that will convert more efficiently sunlight to electrical power is one of the priorities. Nevertheless, understanding of the reliability and lifetimes of already operational technologies is necessary. The comprehension of degradation mechanisms of photovoltaic systems is important because it directly leads to not efficient devices that present losses on the power output. Experimentally, the performance of solar cells is investigated by measuring the change of the output energy. Changes in the performance can be directly related to different degradation mechanisms coming from the exposure of solar cells into weather changes, ambient conditions or the aging of the components.

One of the main degradation modes of silicon solar cells that remains to be understood is light and elevated temperature induced degradation (LeTID). Such degradation can decrease up to 15% the electricity production of the solar panel in one or two decades. In order to explore the insights of this phenomenon, the functioning of solar cells, the different types of solar cells and degradation processes are described along this chapter. The description of the working principle of photovoltaic modules, from charge carrier generation to their extraction and current production, is presented in this first part. The main types of PV modules along with the most common characterization techniques and degradation mechanisms are discussed, along with insights behind LeTID, the most important hypotheses, and mitigation strategies.

1.1 Basic mechanisms in photovoltaic technologies

A solar cell is a device which converts photons coming from solar radiation into electric current. Such a cell is built with semiconductors, in which current production starts when a photon excites an electron in a module atom. Semiconductors are materials in which energy bands are separated by an energy gap of width ϵ_G lower than 3 eV. The energy range below the gap, called the valence band, is nearly completely occupied with electrons and its maximum value is defined by ϵ_v. The energy range above the gap, called the conduction band is nearly empty, its minimum is defined by ϵ_c.

Excitation of an electron from the valence band to the conduction band can occur by the absorption of a photon γ with energy $\hbar\omega$. Due to the excitation, the conduction band has an extra electron while the valence band has an additional hole. For solar cells, the generation of electrons and holes by the absorption of photons is the most important process.

Doping is a process used to change the charge carrier density in the material in order to modify its electronic properties. The introduction of impurity atoms can change the electron or hole density in the material. In the simplest case, these impurities replace the atoms of the semiconductor at their lattice positions. The incorporation of donnors gives free electrons to the semiconductor (n-type semiconductor) while the incorporation of acceptors gives free holes (p-type semiconductor).

The principle of a solar cell is to separate the electron-hole pairs in order to produce an electric current. Nevertheless, the totality of the mechanisms behind the current generation is complex. It involves the efficient generation and extraction of charge carriers to produce an electrical current. The basics of these are presented in this first section.

1.1.1 Charge carrier generation and recombination

In order to produce an electron-hole pair, it is necessary to supply at least the minimum generation energy ϵ_G to an electron in the valence band. This process can occur in different manners, either by photon absorption, by lattice vibrations (phonons) supplying the energy or by impact ionization. The last one refers to an electron (or hole) with enough kinetic energy knocking a bound electron out of its bound state (in the valence band) and promoting it to a state in the conduction band.

In the case of solar cells, the main generation process of electron-hole pairs is by photon absorption. Photons with $\hbar\omega < \epsilon_G$ are not absorbed by electron–hole generation and they are either reflected or transmitted.

> The probability for the absorption of a photon of energy $\hbar\omega$ is defined by the **absorption coefficient** $\alpha(\hbar\omega)$, which is an intrinsic material property. Related to it we have the **penetration depth** of the photons, defined as $L_\gamma = \frac{1}{\alpha}$ [4].

Since absorption requires that an electron–hole pair is generated, $\alpha(\hbar\omega)$ is directly related to the density of occupied states in the valence band in which a hole can be generated, and unoccupied states in the conduction band in which an electron can be generated.

It is important to recall that if the generation of electron-hole pairs by absorption of a photon con-

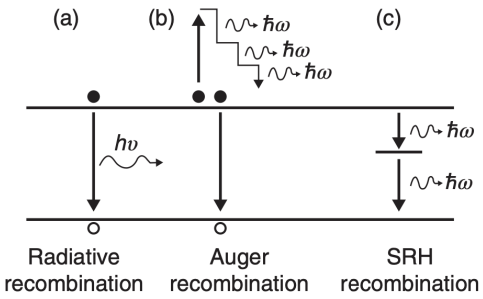

Figure 1.1: Overview of basic recombination mechanisms of photgenerated charge carriers in a semiconductor.

serves both momentum and energy, the transition is therefore direct. Direct semiconductors, such as GaAs have a large absorption coefficient, therefore a small penetration depth of the photons. A solar cell made from these materials does not have to be thicker than only a few μm in order to absorb the part of the solar spectrum with photon energies $\hbar\omega > \epsilon_G$.

In an indirect semiconductor, a transition between the maximum of the valence band ϵ_v and the minimum of the conduction band ϵ_c is not possible with only the absorption of a photon, therefore coupling with a phonon is needed. Due to the large mass of the atoms, phonons with even small energies $\hbar\Omega$ (with Ω the phonons frequency) have a large momentum p_Γ.

The participation of the phonons allows photon-induced transitions from any state of the valence band to any state of the conduction band for which the energy is conserved. The transition probability into one state of the conduction band is then proportional to the number of all states in the valence band separated from this conduction band state by the photon energy $\hbar\omega$ plus or minus the phonon energy $\hbar\Omega$. Because of the small value of α for indirect transitions, the penetration depth for photons in an indirect semiconductor is large. To absorb all photons with $\hbar\omega > \epsilon_G$, which can be absorbed from the solar spectrum, an indirect semiconductor in the geometry of a plane-parallel plate must be more than $100\mu m$ thick. Along with silicon, germanium is also an indirect semiconductor.

Contrary to charge carrier generation we have recombination:

Recombination is the process in which an electron, which has been excited from the valence band to the conduction band, falls back into an empty state in the valence band (hole) or in an empty state induced by an impurity.

With the recombination of an electron and a hole, the energy set free must always be taken up by other particles, therefore either photons, phonons or both are produced simultaneously. The main recombination processes that occur in solar cells are radiative recombination, Auger recombination, and Shockley–Read–Hall (SRH) recombination [4], described schematically in figure 1.1. In the case of radiative recombination (figure 1.1a), a hole reacts with an electron and produces a photon, the exact reverse process of absorption. For non-radiative recombination there are primarily other electrons or holes (Auger recombination) or phonons (impurity recombination) that absorb the generated energy. In general radiative generation of charge carriers is compensated by radiative recombination processes and, in the same manner, non-radiative electron-hole pair

generation is compensated by non-radiative recombination of electron-hole pairs.
Auger recombination is the reverse of impact ionization, in which an electron or a hole with high kinetic energy knocks another electron out of its bond, thereby creating a free electron and a free hole. In the reverse process, the energy set free during recombination is transferred to an electron or a hole as kinetic energy that is subsequently lost to the lattice through the generation of phonons.
In case of Shockley–Read–Hall recombination, the emission of photons becomes possible by the existence of states in the forbidden gap, which are induced by impurities in the semiconductor. In real solar cells, recombination via impurities is the predominant recombination process as they might induce electron states with energies in the forbidden zone. Such energy levels can be located in the middle of the band gap, near to the conduction band or near to the valence band. Photons that are absorbed are more likely to excite electrons from the valence band to these energy levels. Impurities that give rise to energy levels in the forbidden gap are found in large concentrations on the surface of the semiconductor. Here, the neighboring atoms constitute the adjacent layers in the solar cell, and also in these regions impurities are adsorbed. Often, these surface states have a continuous distribution over energy in the forbidden gap.
High efficiency solar cells will require a high generation rate of electron-hole pairs along with low recombination. Electric current will be produced after separating the electron - hole pairs. Their separation and collection will strongly depend on the average time that it takes for charge carries to recombine, i.e., the charge carrier lifetime. In indirect band gap semiconductors, the carrier lifetime strongly depends on the concentration of impurities, as they induce non radiative recombination.
The upper limit for the lifetime of electrons is if all recombination mechanisms are avoided, except for radiative recombination, which is unavoidable. Since the maximum obtainable concentrations of electrons and holes occur if there is only radiative recombination, the knowledge of radiative recombination and of the emitted photon currents is of great importance for the determination of maximum efficiencies.

In general the charge carrier lifetime τ_e will depend on their velocity v_e, the concentration of impurities n_{imp}, and the capture cross-section σ_e

$$\tau_e = \frac{1}{\sigma_e n_{imp} v_e} \tag{1.1}$$

1.1.2 Charge carrier extraction and current production

In order to generate a photocurrent, the charge carriers must be extracted from the photon absorber layer after an electron–hole pair is generated. If we put two contacts in opposite sides of the semiconductor, the electron must leave the device at the opposite contact than the hole.

We define the **bulk material** as the photon absorber layer of the device.

What happens if we bring a n-type layer into direct contact with a p-type layer? Electrons will

diffuse from the region of high electron concentration into the region of low electron concentration. During this diffusion, electrons will accumulate on the region of the p-type layer in contact with the n-type layer, while holes will do the opposite. It will create the so called depletion region, which will induce an electric field. Such an electric field will produce a charge flow, known as drift current, in the opposite direction of the diffusion until equilibrium is reached.
The photo-generated free electrons will move to the p-type layer while the generated holes will move to the n-type side. When the free electrons reach the n-type side, they cannot further cross the junction because of the barrier potential generated. In the same way, holes are confined once they reach the p-type side. As the concentration of electrons becomes higher in one side and concentration of holes becomes more in the other side, a voltage difference is created. If we connect a load across the junction, a current will flow through it. This is the process to convert sunlight in electric current by the means of the easiest solar cell structure, which is a p-n junction. A simple diagram of the operating mechanism of a solar cell is shown in figure 1.2.
Once an electron-hole pair is generated by a photon absorption, it is not sure that it will be collected by the p-n junction and contribute to the photo-generated current, the probability that this happens will depend on the surface properties of the device, the distance that the charge carriers must travel, and the diffusion length of the material.

Diffusion length is the average length a charge carrier travels before it recombines. Semiconductor materials with high recombination rates, for example, heavily doped materials, have short diffusion lengths.

In the depletion region electrons move to the n-type side of the junction while holes move to the p-type one. Due to the electric field present in this region, charge carriers move away from each other fast enough to be collected; therefore the collection probability in the depletion zone is one. If charge carriers are generated far from the junction and at a distance higher than the diffusion length, the probability of them being collected will be zero. The same will happen if they are generated close to a region with a high recombination rate, such as a surface. When they are treated in such way that such defects are “filled” so they cannot recombine, we say that the surface has been passivated. Figure 1.3 illustrates the impact of surface passivation and diffusion length on collection probability. The photon-generated current of a solar cell will be therefore determined by the

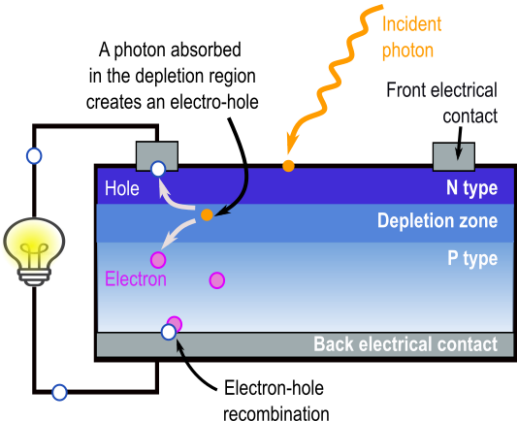

Figure 1.2: Operation mechanisms in a pn solar cell.

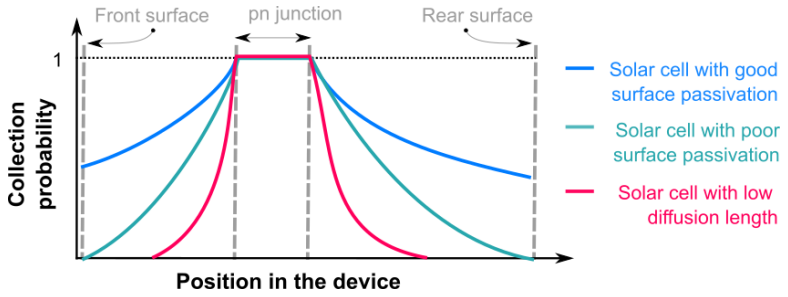

Figure 1.3: Collection probability comparison between solar cells with good and poor surface passivation, and solar cells with low diffusion length. With high surface recombination, the collection probability at the surface is low. We observe that for carriers generated at the pn junction, the collection probability is 1.

charge carrier generation rate along with the collection probability. The light-generated current is the integration over the entire device thickness of the generation rate at a particular point in the device, multiplied by the collection probability at that point.
The collection probability is directly related to the spectral response of the device. If we consider a solar cell where the bulk has a collection probability higher than the surfaces, photons absorbed near the surface will be likely to recombine and will barely or not contribute to the photogenerated current.
We recall that photons with energies lower than the band gap are not absorbed by the semiconductor. The probability for the absorption of a photon of energy $\hbar\omega$ is proportional to the density of occupied states in the valence band in which a hole can be generated, and unoccupied states in the conduction band that can be occupied by an electron. Photons with higher energy will be absorbed near the semiconductor surface, while photons with energies closer to the band gap will penetrate deeper.

1.2 Silicon solar cells

The importance of the main material in solar cells resides first in its absorption properties. The generation and collection properties are more impacted by the purity of the material and the structure of the device. Solar cells can be made of only one single layer of light-absorbing material (single-junction) or use multiple layer configurations (multi-junctions) to take advantage of various absorption and charge separation mechanisms. In general, they are named after the semiconducting material they are made of and they are commonly classified into first, second, and third generation cells.
The first generation cells are made of crystalline silicon, the commercially predominant photovoltaic technology (around 90% of the produced solar cells are silicon-based).
Second generation cells are thin film solar cells, which are made of amorphous silicon, cadmium telluride (CdTe) or copper indium gallium selenide (CIGS) cells. They represent around 10% of commercial solar cells.
The third generation of solar cells includes a number of thin-film technologies often described as emerging photovoltaics. Many use organic materials, often organometallic compounds as well as

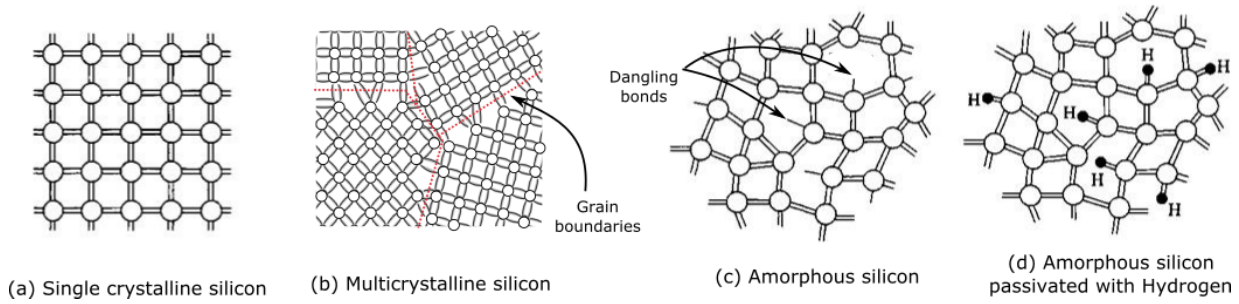

Figure 1.4: Atomic structure of different types of silicon materials.

inorganic substances. They also include solar cells based on III-V semiconductors.
Single and poly-crystalline silicon solar cells represent the first generation. These solar cells are used worldwide and about 80% of the solar cell market is based on single crystalline solar cells and they have the one of the highest commercial efficiencies. The varieties of silicon used for solar cells can be single crystalline (sc-Si), multicrystalline (mc-Si), polycrystalline (pc-Si) or amorphous (a-Si).
The main difference between them is the purity of the crystalline structure. Their main characteristics are presented in table 1.1.

1.2.1 Degradation of solar cells

Photovoltaic modules have a high probability of performing adequately for about 30 years, working under typical operating conditions. Their reliability and lifetime depend mainly on different degradation mechanisms. Temperature and humidity are common factors on almost all solar cell degradation types, along with corrosion, mechanical shocks and light exposure. Such mechanisms can be divided into extrinsic and intrinsic degradation. Extrinsic mechanisms are caused by the infiltration of external substances, such as air, oxygen or water, for example. The main extrinsic degradation types are corrosion, discoloration, delamination, breakage, and cracking cells [6]. The damage of such external mechanisms becomes more important under light exposure.
On the other hand, intrinsic mechanisms regard changes in the structures of the interfaces between layers or within the bulk material. Therefore, they will depend strongly on the material of the solar cell; semiconductors that are less stable will have more issues regarding power loss. Light and elevated temperature induced degradation (LeTID) is an example of a common intrinsic degradation type in silicon based solar cells. It is believed that during LeTID, the exposure to sunlight and temperatures around 70ºC over some years changes the structure of defects inside the bulk material, which activate them to capture electrons and therefore reduce the power outcome.

	Grain size	**Common growth techniques**
Single crystal	$> 10cm$	Czochralski (CZ) float zone (FZ)
Multicrystalline	$1mm - 10cm$	Cast, sheet, ribon
Polycrystalline	$1\mu m - 1mm$	Chemical vapor deposition
Microcrystalline	$< 1\mu m$	Plasma deposition

Table 1.1: Different types of silicon materials used in photovoltaics technologies [5].

Nevertheless, the precise phenomena and defects behind remain unknown.
Detecting the cause and determining the mechanisms of a specific type of degradation might not be straightforward. Different techniques and testing methods are used to study solar cell performance and to determine the mechanisms behind a specific degradation in a particular solar cell type. However, it is difficult to reproduce the "real conditions" to which solar cells are exposed, because their degradation requires long periods of time, over months or even years. For this reason, accelerated tests are an alternative but most of the results obtained are not always consistent on the degradation rates of solar modules.

1.2.2 Point defects in silicon

Intrinsic degradation mechanisms are strongly related to the atomic structure of the interfaces or bulk material of the device. It is well known that impurities and dislocations can cause significant deterioration in the conversion efficiency of solar cells. In the case of LeTID, it has been observed that is related to the point-like defects in the silicon bulk material.

> **Point-like** defects are crystalline imperfections of the order of one to few atoms. They introduce constant energy levels in the electronic structure of the crystal.

Figure 1.5 shows the most common point-like defects in silicon: self silicon defects, including vacancies and self interstitial silicon atoms; and extrinsic defects or impurities. Defects that introduce energy levels within the band gap can be classified as shallow or deep level defects.
Shallow defects induce energy levels near the edges of the band gap. Such energy levels, ϵ_n and ϵ_p, lie near the bottom of the conduction band (BCB) and the top of the valence band, respectively, as shown in figure 1.6. If an impurity induces a level ϵ_n in the vicinity of the conduction band, captured electrons are easily released to the conduction band, contributing with a negative carrier to the host, and the impurity is said to be a donor center. On the other hand, if the impurity level ϵ_p is near the valence band, it can capture electrons from the valence band while captured holes are emitted back to the valence band before they can recombine by electron capture. These centers are therefore typically referred to as acceptors. Therefore, shallow defects are also called dopant impurities, they are intentionally introduced in the crystal during the device manufacturing process to increase the free carrier concentration.
Impurities that offer energy states in the middle of the band gap play the most important role. As they capture electrons and holes over a series of excited states, the recombination energy can be

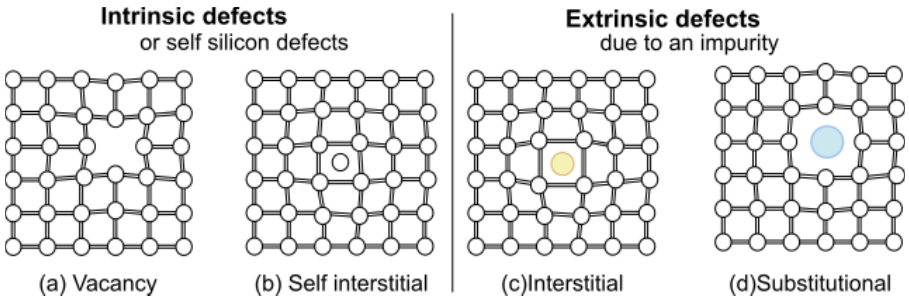

Figure 1.5: Schematic two dimensional representation of point defect types in crystalline silicon

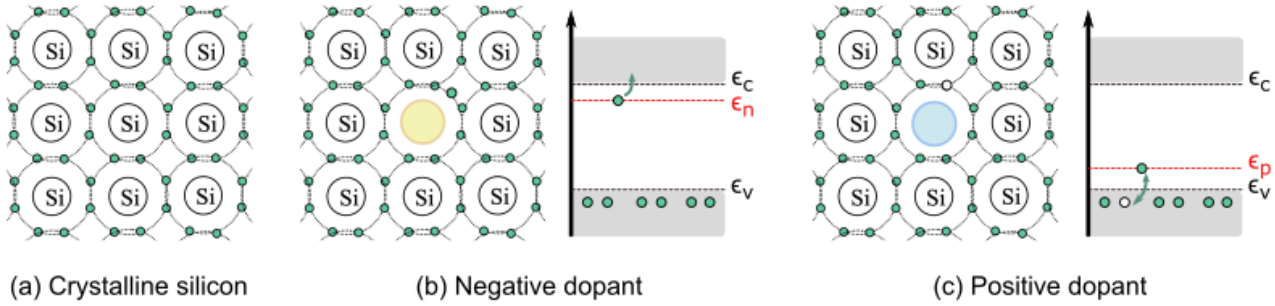

Figure 1.6: Substitutional impurities used as negative and positive dopants in crystalline silicon.

dissipated in small portions through the production of several phonons. Therefore, the capture of an electron and a hole by an impurity can take place much more easily. These are known as deep level defects. Deep level defects are typically undesirable side effects of the manufacturing or doping process and they might strongly affect the performance of microelectronic devices. If such impurities are capable of trapping free carriers deep into the semiconductor band gap are said to be electronically active, since they modify the electronic properties of the material.

The type and content of impurities in bulk silicon in the solar cell largely depends on three main factors: the choice of method for producing silicon, the doping process, and the solar cell manufacturing process. Light elements, such as hydrogen, carbon and oxygen, are three of the major impurities present in silicon materials [8]. In the specific case of solar silicon, its large scale production requires cheap growth methods which translates into higher concentrations of metallic impurities with respect to other silicon semiconductor components. Iron is one of the a dominant metal impurities coming from the synthesis process. Along with chromium and nickel, they are components of steel, widely employed as construction materials for equipment, often resulting in significant silicon contamination[9]. Other metallic impurities coming from the manufactur-

Metallic impurity	**Concentration** $[cm^{-3}]$
Aluminum	3.72×10^{15}
Zirconium	8.19×10^{14}
Silver	3.97×10^{14}
Titanium	3.26×10^{14}
Iron	2.02×10^{14}
Tungsten	1.58×10^{14}
Copper	8.30×10^{13}
Yttrium	7.72×10^{13}
Nickel	4.26×10^{13}
Chromium	1.17×10^{13}
Vanadium	7.26×10^{12}
Molybdenum	6.45×10^{12}
Cobalt	5.27×10^{12}
Manganese	3.07×10^{12}

Table 1.2: List of metal impurities with a total concentration of more than $10^{-12} cm^{-3}$[7].

ing processes of solar cells are also present in the silicon bulk material. Table 1.2 summarizes the metallic impurities with highest concentrations in mc-Si solar cells. Experimental and theoretical studies have pointed out that specific attention must be devoted to transition metal impurities, particularly those in the *3d* series, as they affect the minority-charge-carrier lifetime, and therefore the solar cell efficiency [10].

1.2.3 How to spot deep level defects during solar cell degradation?

In order to understand the role of point defects in silicon solar cells degradation, in particular regarding LeTID, it is necessary to discuss not only degradation testing methods but also deep defect characterization techniques. In general, all these measurements require standardized testing, in order to properly compare the behavior of different silicon cells that might have been manufactured with different processes. They include standardized cell temperature, light intensity, pressure, and a spectral range of light. In particular, to standardize the units of incident light for degradation measurements, it is convenient to define the *number of suns*.

> The light intensity that strikes a solar cell is referred to **number of suns**, where 1 sun corresponds to standard illumination at AM1.5, or $1 kW/m^2$.

Experimental measurements of degradation mechanisms are very vast and might vary depending on the degradation type to which they are related. Some of them simply consider the power loss of a solar cell along time with respect to the maximal power output. In other cases, they account the solar cell efficiency relative change with time.
Considering intrinsic degradation mechanisms, measurements must be related to defects in the bulk material or surfaces. A common quantity to be measured is the charge carrier lifetimes. There are two basic approaches to measure the lifetime: one possibility is to maintain a steady-state generation rate of known value, and to obtain the lifetime value considering that the generation and recombination rates are completely balanced. A second possibility is to terminate the generation abruptly and measure the rate at which carriers disappear. Since the photogeneration is zero, the change of charge carriers concentrations due to recombination [11]:

$$\frac{\mathrm{d}n}{\mathrm{d}t} = \frac{-\Delta n}{\tau} \tag{1.2}$$

In particular, the charge carrier lifetime of the bulk material (τ_B) depends on the recombination rates due to radiative recombination, Auger recombination and Shockley–Read–Hall recombination [4]:

$$\frac{1}{\tau_B} = \frac{1}{\tau_{rad}} + \frac{1}{\tau_{Auger}} + \frac{1}{\tau_{SRH}} \tag{1.3}$$

For the case of indirect semiconductors, radiative recombination is very rare so the term containing τ_{rad} can be neglected. The Auger lifetime can be determined according to the specific type of silicon material with semi-empirical methods. Another common quantity to be obtained is the normalized defect density (NDD) [12]:

$$NDD(t) = \left(\frac{1}{\tau_{eff}(t)} - \frac{1}{\tau_{eff}(t=0)} \right) \tag{1.4}$$

The measurement of such quantities allows us to know the amount of defects causing the degradation, nevertheless it does not provide information related to the defect distribution nor their composition. For this aim, defect characterization techniques are required. Defects in the bulk material or surfaces can be characterized according to their structure, their optical or electrical properties or their migration mechanisms.

The fact that point defects in semiconductors induce one or several states in the band gap, allows the occurrence of electronic excitations due to light absorption or spontaneous emission of photons or luminescence after an electron decay. Therefore, a photocurrent might be measurable if the electronic transitions involve a localized defect state and one of the bands (ϵ_c or ϵ_v)of the semiconductor material. As a result, optical absorption and photoconductivity measures are of great interest to characterize optical and electronic properties of point defects.

The use of experimental techniques, such as transmission electron microscopy (TEM) and electron paramagnetic resonance (EPR), the structure and chemical configuration of point defects in silicon might be determined. Concerning the optical properties of defects, such as local vibrational modes, they are usually measured by Fourier transform infrared spectroscopy (FTIR). Binding energy and migration can be studied by performing annealing experiments.

In order to study their electrical properties, common techniques are electroluminiscence, photoluminescence (PL) and Deep Level Transient Spectroscopy (DLTS)

Electroluminescence is the emission of light in response to the application of an electrical current or a strong electric field. In electroluminescence measurements, current is injected to a solar cell and radiative recombination of carriers causes light emission.

For indirect band gap semiconductors, most of the recombination is due to Auger recombination or defects in the bulk material and surfaces. However, the small amount of radiative recombination can be sensed using an external detector.

This characterization method can only be performed once the metallization of the module has been applied because it requires electrical contact for the current injection. It is a technique that

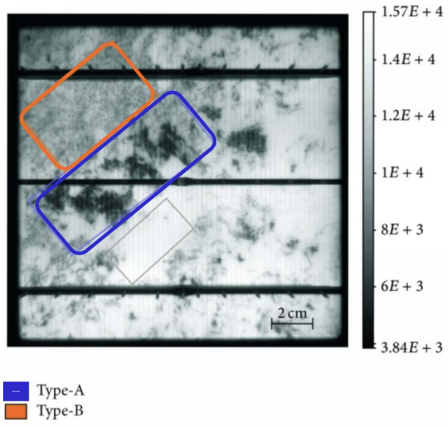

Figure 1.7: Electroluminescence measurement in a mc-Si module [13].

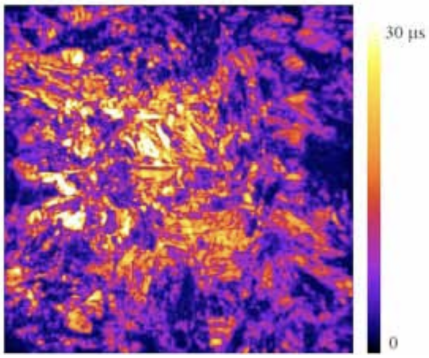

Figure 1.8: Effective minority carrier lifetime from a PL image on a 6 inch SiN passivated multicrystalline silicon wafer [14].

provides information about the distribution of charge carriers in the solar cells and modules. The main advantages of electroluminescence imaging is that it is a fast and non-destructive measurement.

Solar panel electroluminescence can be used to spot defects via a rapid scan of a panel. Darker areas indicate module faults or defects. For example, in figure 1.7, recombination defects can be distinguished into type A and B by an image processing procedure [13].

Photoluminescence is a process in which a photon excites one electron to a higher electronic excited state. A photon is radiated as the electron returns to a lower energy state. In the case of a semiconductor, by absorbing incident light whose energy is higher than the energy band gap.

This type of imaging allows us to obtain spatially resolved data on bulk lifetime, as observed in figure 1.7. Parameters as impurity rich, low lifetime regions or dislocation densities can be extracted from photoluminescence images [14].

The main advantage of photoluminescence over electroluminescence is that it can be observed in any stage of solar cell processing. This is because charge carriers are generated by photon absorption; i.e. contacts are not required. Therefore, photoluminescence is particularly promising at an early stage of production. It allows early detection of production problems. The disadvantage is that the generated luminescence signal has a much lower intensity compared to the intensity of the light used to generate the electron-hole pairs. As the measurement is performed while illuminating the samples, the incident light wavelength is restricted to a narrow wavelength interval. In this way, it can be easily filtered from the measurement of the photoluminescence [4].

On the other hand, the Deep Level Transient Spectroscopy (DLTS) technique estimates the relative position of a trap level with respect to the bulk material bands, by monitoring its capacity for emitting electrons at a given temperature. DLTS therefore measures the activation energy required for a trap to release an electron and the probability of such thermal process to occur. Results of DLTS measurements give an approximation of the temperature regime for which a given defect is electronically active.

1.3 Light and elevated temperature induced degradation

The operating properties of solar cells are affected by the change of ambient conditions such as temperature and the amount of incident light. The increase of the light intensity incident on a solar cell increases the temperature operation of the solar cell. Such devices are sensitive to temperature as increases in temperature reduce the band gap of the semiconductor material. These phenomena and their impact in the properties of the photovoltaic module are well known. Nevertheless, it has been recently found that silicon- based solar panels are affected by light and elevated temperature degradation (LeTID) after some years of use. Such degradation occurs on time scales of decades and it can result in up to 16% of relative efficiency losses in multicrystalline silicon solar cells. It occurs in almost all types of silicon wafers, including next-generation silicon solar cells [12]. After reaching the maximal degradation extent, the solar devices present a recovery phase, which means that, if we take a look at the evolution of the efficiency of the solar cell over time, it would look like in figure 1.9. This behavior is observed in cells when exposed to light with operating temperatures between 50ºC and 85ºC [15].

This type of aging causes a large amount of losses on the electrical output over the years because degradation and regeneration cycles require decades to take place. Some laboratory tests show that a duration of 15 years out in the field could be required before maximum degradation is reached, with regeneration expected to occur on a much longer time scale [12, 16]. As silicon modules have a designated warranty of 25 to 30 years, this could pose significant issues for manufacturers, energy suppliers, and consumers.

Considering that nowadays silicon based solar cells represent 90% of the photovoltaic market, the study of the mechanisms causing LeTID is of great importance for the development of photovoltaic technologies. Even though there are several treatments to reduce or eliminate the impact of LeTID in the solar cell performance, the root cause remains to be understood. It is believed that LeTID is caused by point defects in the bulk material. Exposure to sunlight and temperatures over 50ºC may change the structure of the "LeTID defect" so it is activated to capture electrons. After reaching a state of maximum degradation, the continuous exposure to these conditions inhibits the active LeTID defects and leads to a recovery phase . So far, the defects involved in this

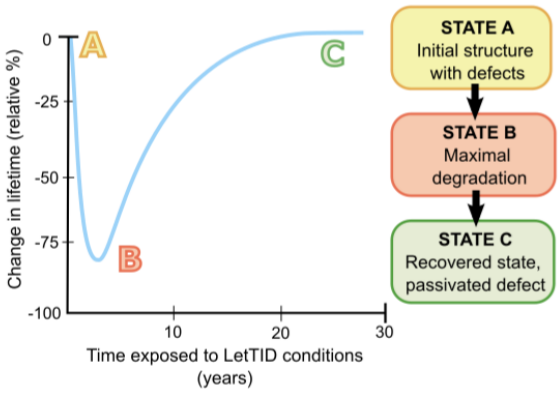

Figure 1.9: Evolution of charge carrier lifetimes due to LeTID. The scheme is only approximative in time.

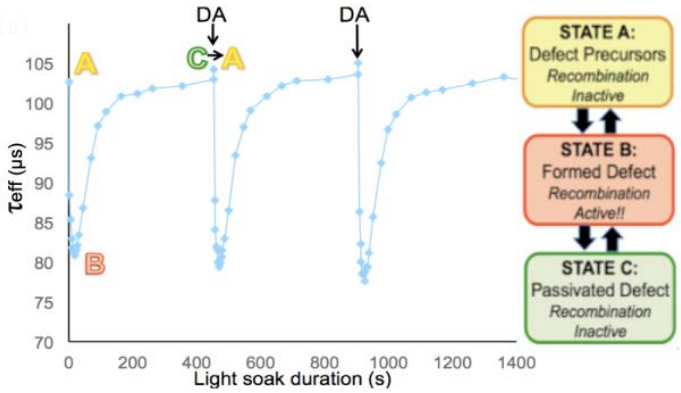

Figure 1.10: Cyclic evolution of degradation and regeneration processes in LID performing an accelerated test. Figure taken from [15].DA stands for dark annealing.

degradation have not been determined yet.
In the following sections we will discuss the main characteristics of LeTID, and the most popular theories that have been proposed to understand its mechanisms and the related mitigation processes suggested so far.

1.3.1 LeTID as a three state model

LeTID was first observed in 2012 in multicrystalline silicon passivated emitters and rear cells (PERC) operating under normal light and temperature conditions[17]. Since then, it has been reported to reduce the performance of devices up to 16% without any treatment [18]. Despite the joint effort of many research groups, the root cause of the degradation is still under discussion.
As a first attempt to understand LeTID, it was compared to the well understood light induced

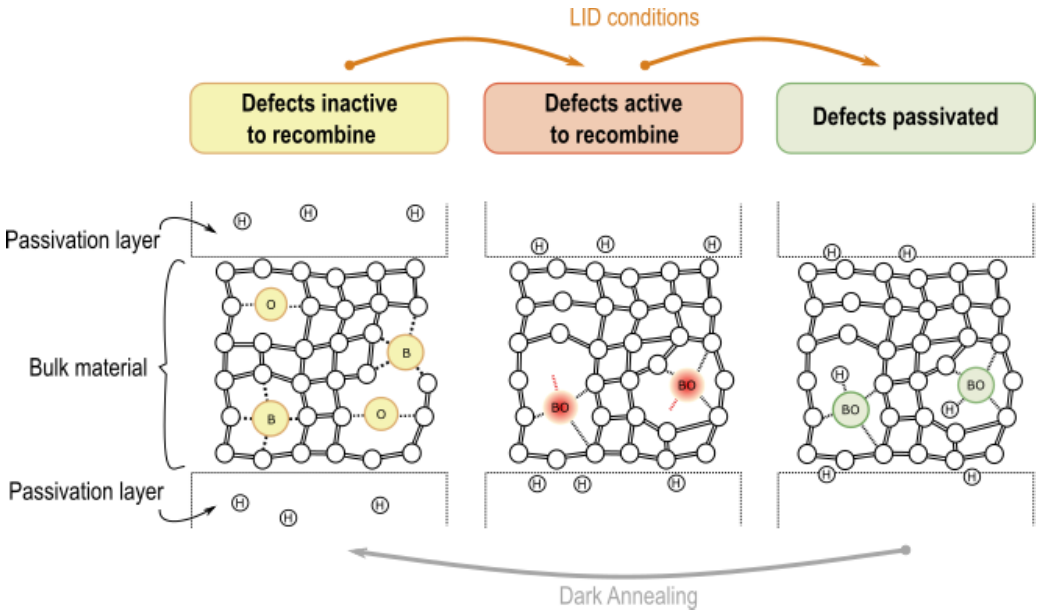

Figure 1.11: Example of a 3 step model to explain LID. The state of maximal degradation occurs when all the B and O defects form B-O complexes, which recombines with electrons and decreases the module efficiency. When all the B-O defects are passivated, they do not trap electrons anymore. Therefore, the recovered state is reached.

degradation (LID). First observed in 2002, LID causes significant performances losses in silicon modules within only some hours of sunlight exposure, . Nowadays, its mechanisms are well understood and it has been attributed to boron-oxide (BO) defects in the bulk material [19, 20]. From this comparison, the simple three step model used to explain the mechanisms behind LID was adopted for LeTID. LID is an aging process that, as LeTID, presents degradation and recovery phases when looking at the efficiency of the module. Figure 1.10 shows the evolution of the charge carrier lifetime for a silicon module exposed to LID conditions during accelerated test [15]. The charge carrier lifetime is obtained by the use of equation 1.3 where the term τ_{SHR} is related to the initial lifetime τ_0 and the lifetime at the state of maximal degradation τ_{deg} [21]:

$$\frac{1}{\tau_{SHR}} = \frac{1}{\tau_{deg}} - \frac{1}{\tau_0} \tag{1.5}$$

Such changes in the free charge lifetime are caused by the formation of the BO defects in the material. We observe in figures 1.10 and 1.11 that initially the bulk material is in state A, at which the BO defects have not yet been formed. The recombination process is not happening. As the bulk material is exposed to light, BO defects start to form (state B) and recombination occurs, lowering the charge carrier effective lifetime τ_{eff}. Hydrogen atoms migrate from other layers of the module and passivate the recently formed defects, preventing recombination from happening. The system recovers a high charge carrier lifetime and stability under illumination (state C).

Annealing is a high-temperature furnace operation that can relieve stress in silicon, activates or moves the dopants, densifies different types of films and repairs certain damages occurred during the wafer processing.

Accelerated test are employed to test LeTID in solar cells in minutes instead of hundreds of hours. To accelerate the duration of the degradation tests, increased temperature and illumination sources ten or hunderd tiemes brighter than the sun (usually lasers) are used[22]. This is the case of the tests presented in figures 1.10 and 1.9.
During this accelerated test, an anneal process in the absence of light (dark annealing) allows to return the system from state C to state A after the silicon modules have been degraded by light. After dark annealing, the degradation and regeneration stages of LID are observed, pointing to a periodic phenomenon. By carefully H-passivating the BO defects before exposing the modules to light, the LID was corrected [15].
Even though LeTID cannot be understood by the exact same mechanisms as LID, a similar three-stage model is used to explain the changes in the charge carrier lifetime [15, 23, 24, 25]. As observed in figure 1.12, LeTID shows no periodicity in the degradation-regeneration cycles after dark annealing treatment. To explain this behavior, let us consider some LeTID defects D in the silicon module. Such defects can be stored either like heavy doped regions, impurities in the material or in some structural defects, like grain boundaries or dislocations. When they are trapped, they are in a state at which they cannot recombine with charge carriers, allowing for higher carrier lifetimes (and good module performance). The conditions to trap and release D in each structure are different, so we consider that they could be in one of these states:

- **Reservoir**. LeTID defects in the reservoir D_R are bounded strongly to their traps. After ex-

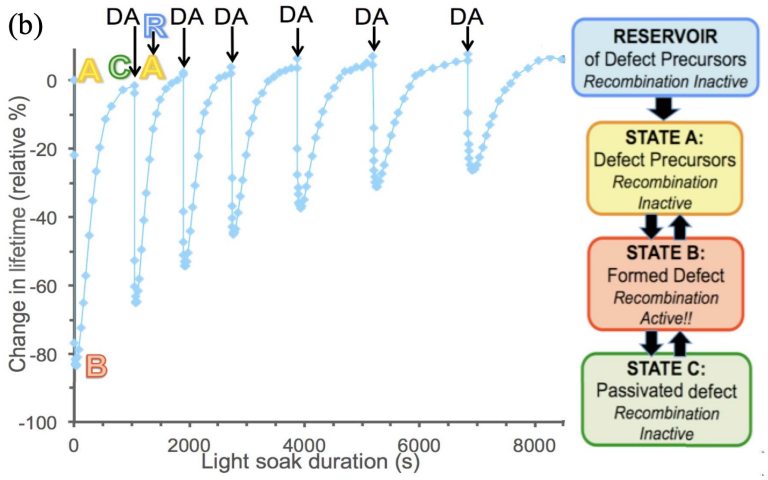

Figure 1.12: LeTID cycle measured experimentally performing an accelerated test. It is observed that it does not show repeatable degradation cycles as LID. (Figure taken from [15]).

posure to LeTID conditions, the reservoir feeds defects in state A (D_A), which are not able to recombine with charge carriers either.

- **State A**. LeTID defects D_A are weakly trapped into impurities or structural defects. When exposed to working conditions of the solar cell (carrier induction and temperatures above 50ºC - 60ºC) they will create LeTID defects that will activate the charge carrier recombination process (D_B).

- **State B**. When LeTID defects are in an unstable state where they can recombine with charge carriers (D_B), a decrease in the carrier lifetime will be observed. At the beginning, the amount of defects going from state A to B will be very high and degradation will take place rapidly. The degradation is reduced when the rate of D_R going from the reservoir to state A is the same as the one of atoms going from state A to B.

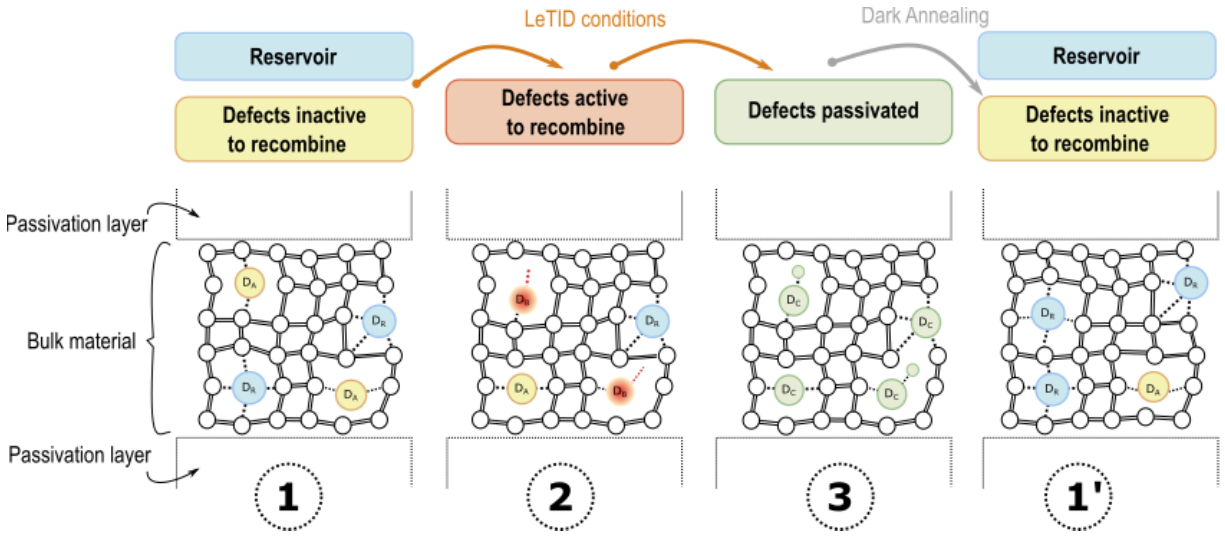

Figure 1.13: LeTID cycle measured experimentally performing an accelerated test. It is observed that it does not show repeatable degradation cycles as LID; see figure 1.10. (Figure taken from [15]).

- **State C**. The device is fully recovered when all defects D_B are passivated, i.e. their ability to recombine is disabled. Passivation is achieved by dispersion of D_B toward grain boundaries, the wafer surfaces or if they join to an atom with a bond strong enough to not be broken under LeTID conditions.

A dark annealing process allows us to move LeTID defects that have been passivated (D_C) to a stable state where they are unable to recombine with charge carriers, either D_R or D_A. As the bond between traps and defects D_R is stronger than D_A, D_R defects are more stable and therefore more likely to form. If in the next LeTID cycle the amount of D_R is higher than D_A, the maximal extent of degradation will be lower, which explains the aperiodicity of LeTID. The kinetics of LeTID depends on the thermal history of the sample. Thus, dark annealing does not restore the initial state of the wafer, it rather puts it into a new state, with different degradation and regeneration rates.
A clear example is the case of boron doped crystalline silicon; here, the most problematic ways to store hydrogen are by molecular hydrogen H_2 (reservoir) and hydrogen bounded to boron $H-B$ (state A) [26]. The LeTID conditions rapidly break the $H-B$ bounds, forming a source of interstitial hydrogen that provokes recombination. During dark annealing, interstitial hydrogen will be more likely to form H_2 molecules than $H-B$ complexes.

1.3.2 LeTID main characteristics.

The characteristics of LeTID are rather complex. Even though it normally occurs only under illumination and high temperatures (above 70ºC), it has been observed that LeTID can also be induced under carrier injection [27]. Then, the rate and extent of the degradation depends not only on temperature, but also on the carrier injection level, which is influenced by the operating conditions and the illumination intensity [27, 28]. For example, a linear dependence between the degradation rate constant and the injected carrier density Δn was found in the regime of $10^{13}-10^{15}$ carriers/cm^3[25]. Many more studies on the dependence of LeTID kinetics on illumination, dopant type and doping concentration, among others, have been published. What is important to note, however, is that all these reports converge at demonstrating that the key factor really impacting the LeTID kinetics is that of the amount of excess carrier, i.e. generated electron and holes. This is independent of their generation origin, that is, photogenerated or as the result of applied current.
LeTID has also been named carrier induced degradation (CID), nevertheless, CID describes a wider range of mechanisms including among others BO-LID and Cu-LID [16].
Unlike LID, LeTID has been observed in almost all types of silicon-based modules[12]. At first, it was believed to happen exclusively in p-type multi-crystalline silicon, but with the years it was observed in different types of pure silicon modules. Studies on FZ-silicon, a type of silicon with low metallic impurities and crystallographic defects, showed that LeTID behaves the same as in other types of silicon-based cells, different only in the extent of the degradation rate [30, 31].
More recent works have shown the existence of LeTID in n-type silicon wafers as well [16]. Although there remains a possibility that the degradation observed on different wafer types is caused by different defects, there is strong evidence and many behavioral similarities suggesting that the recombination active defect in each of these materials is the same.

In particular, LeTID in mc-Si presents a spatial dependence where degradation around $200\mu m$ – $400\mu m$ wide across grain boundaries is weaker than in the intra-grain regions, where it is observed to be homogeneous [30, 32]. Comparison between the degradation and regeneration rates in intra-grain and boundary regions is presented in figure 1.14(a) [29], along with photoluminescence and light beam induced current images of degraded p-type mc-Si PERC solar cell [16].
In order to explain the spatial distribution for LeTID, it has been hypothesized that structural defects, such as dislocations, vacancies and self insterstitial silicon, presented at the grain boundaries either inhibit LeTID defect formation or passivate it [29, 34]. Other possible explanations concern lower charge carrier concentrations or doping differences around the grain boundaries[29][35]. Even though some materials have shown a relation between doping concentration and LeTID extent, measurements on FZ-silicon have proven wrong the idea of grain boundaries having less degradation due to a difference in the dopant concentration[33]. FZ-silicon has doping variations lower than 5%. Measurements on photoluminescence in such FZ-silicon samples are depicted in figure 1.14 for the initial, maximal degraded, and recovered states.
Another property that differentiates LeTID from other CID processes is the dependence on the degradation extent on the peak temperature of the solar cell metallization. This metallization pro-

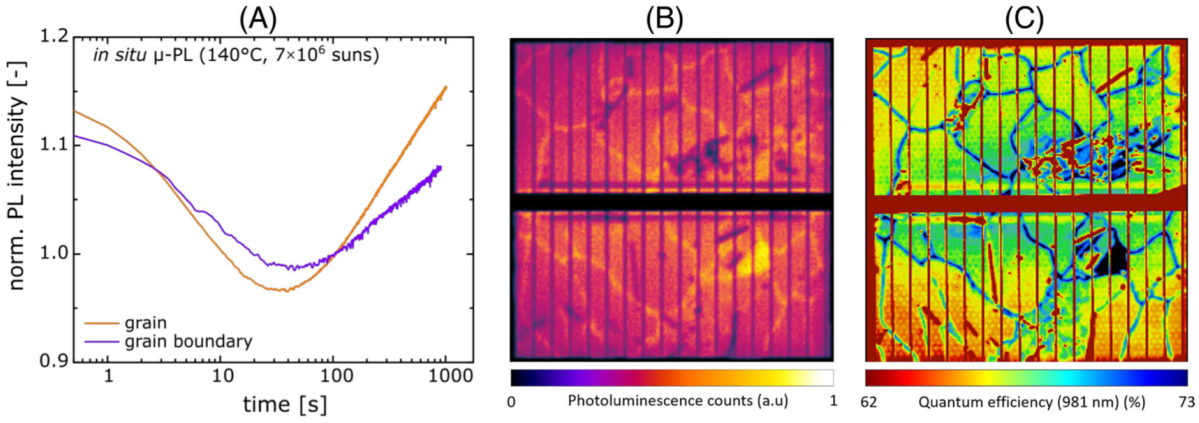

Figure 1.14: Photoluminiscence signal comparison in intra-grain and grain boundary of mc-Si. Figure (A) taken from [29]; figures (B),(C), taken from [16]).

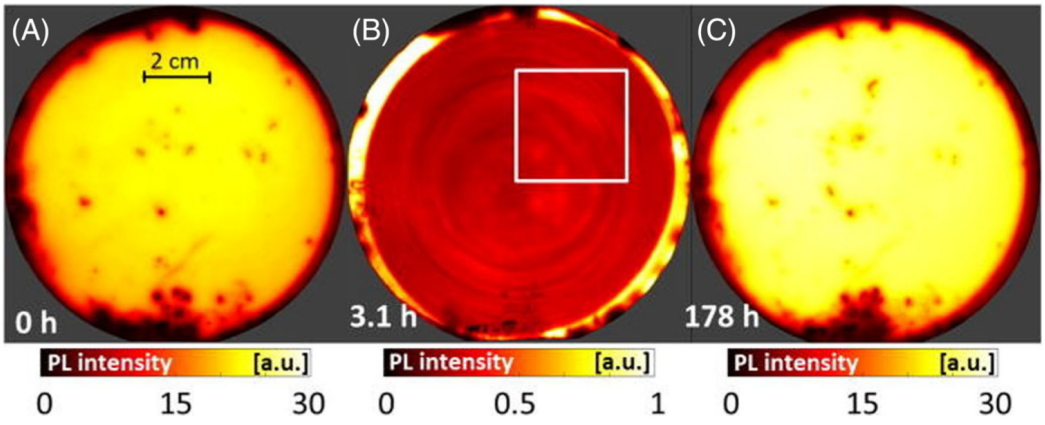

Figure 1.15: Photoluminiscence images of 1 $\Omega - cm$ p-type FZ sample passivated with 10nm $P - ALD Al_2O_3$, capped by 100nm PECVD $a - SiN_x$ and fired at 900ºC [33]. The images are taken at (A) inital state, (B) maximal degradation, state and (C) recovered state.

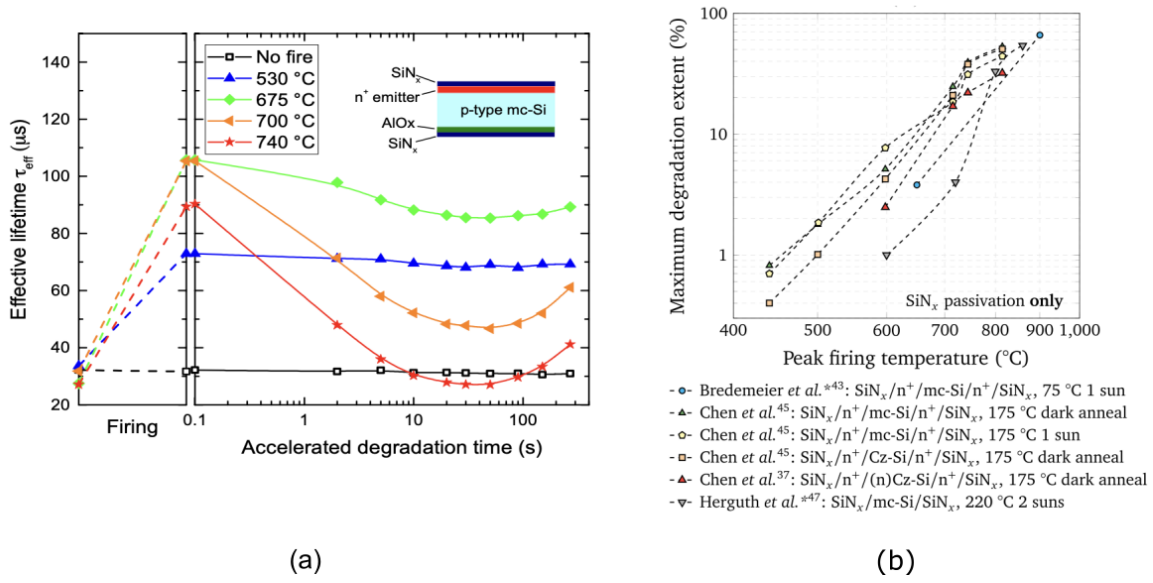

(a) (b)

Figure 1.16: LeTID extent dependence on the firing step. (a) Lifetime after increasing firing temperatures and subsequent LeTID testing. Figure taken from [15]. (b) Maximum degradation extent as a function of the peak firing temperature. Figure taken from [16].

cess is often referred to as contact firing process.

Figure 1.16 shows the maximal degradation extent of solar cells fired at temperatures between 400ºC and 920ºC [16]. In several studies, LeTID was not found to occur if solar cells were fired below approximately 650ºC or not fired at all [30, 36, 37]. For the case of cells with passivation layers, the relation between maximal degradation extent and peak firing temperature is almost exponential. Nevertheless, this relation seems to depend on the structure and passivation layer type of the cell. It has been observed that LeTID not only depends on the peak firing temperature, but also on the cooling rate of the solar cell. High peak temperatures and fast cooling rates enhance LeTID and vice versa, low peak temperatures and slow cooling rates can largely suppress it [38, 39]. It has been observed as well that LeTID was present only in samples with dielectric layers during the firing step[40].

From the experimental evidence presented so far, we observe a dependence of the LeTID extent on the cell structure and passivation layers. This made scientists think that degradation might not arise from a bulk defect. Nevertheless, several studies have demonstrated that it is, indeed, caused by a bulk defect [41].

1.3.3 The defect precursors behind LeTID

We have discussed that, even if the first discovery of the LeTID phenomenon was reported for p-type boron-doped mc-Si materials only, similar degradation has been observed for various other materials including float zone silicon, Cz-Si, high performance mc-Si, and mono crystallyne-like Si in both p- and n-type materials [16]. Keeping in mind that each type of silicon is grown under different conditions, different defect species and different concentrations are expected to be found among them.

Such materials present differences in the rate and extent of LeTID but the behavior of the degra-

dation remains the same, pointing to the existences of a universal LeTID defect mechanism.
After initial suggestions that the degradation might arise from LeTID degradation of dielectric surface passivation layers, many results indicate that the degradation arises from a recombination-active bulk defect [41]. Even more, measurements as electroluminescence, photoluminescence or light beam-induced current measurements have shown that the LeTID defect is distributed homogeneously across intra-grain regions in mc-Si.
Other important characteristics of LeTID include its dependence on the firing step and on carrier injection. All these properties observed about the degradation behavior lead to the assumption that LeTID is triggered by the concentration of a specific impurity (or a mix of impurities) that is more or less homogeneously distributed over the wafer area. The simple three-state model presented in section 1.3.1, explains the main behavior of LeTID such as its dependence on the peak firing temperature and the cooling rate [39] and the formation of a bulk defect in the wafer prior to degradation [42]. Nevertheless, it does not provide with a precise description of the role of silicon intrinsic and extrinsic defects on the LeTID precursor mechanisms. There is a general consensus concerning the role of hydrogen in LeTID [15, 30, 37, 43, 44, 45, 46]. Some other defects as metallic impurities and structural defects in silicon have also been proposed as precursors of LeTID. These cases will be discussed in the following sections.

1.3.4 Hydrogen as a LeTID cause

Nowadays, from an experimental point of view, there is a general consensus around the fundamental role of hydrogen as precursor for LeTID [15, 30, 37, 43, 44, 45, 46]. Among others, studies such as lifetime measurements for samples with different amounts of hydrogen concentration in the bulk material, followed by a LeTID test, have shown that modules with higher H concentrations present higher degradation [47].
In mono and multi-crystalline silicon, experiments show that the presence of hydrogen in the silicon bulk is related to the firing step applied during the solar cell fabrication. The amount of hydrogen remaining in the silicon bulk after the firing treatment depends on the properties of the dielectric films, the peak firing temperature and the cooling rate [37, 46]. The overall dependence on the firing conditions led to the first hypothesis: hydrogen diffusing from the surface dielectric films could either activate the LeTID defect or be part of the LeTID defect itself. Figure 1.17 shows that the concentration of defects associated to LeTID increases with the hydrogen content, introduced during the firing step.
One of the most important hypotheses of hydrogen as a LeTID cause considers that hydrogen might cause recombination on its own [15]. Known as hydrogen-induced degradation (HID), this theory relies on the electronic properties of hydrogen charge states and on its ability to act as a dopant. Dynamics, stability and dissociation of monoatomic hydrogen defects as H^+, H^0, H^- and of hydrogen dimers H_2 in crystalline silicon has already been studied by ab initio methods [48, 49]. It has been observed that hydrogen in various semiconductors, including silicon, can be present in both positive and negative states. In p- type materials, hydrogen donates its electron and is stable in the positive charge state (H^+). Due to coulombic attraction, H^+ tends to neutralize and bind with the dopants. The reverse happens in n-type materials with an abundance of electrons; the hydrogen atom takes an electron, acting as an acceptor, and sits stably as (H^-). In this way,

hydrogen tends to react against the prevailing conductivity of the material in which it resides, a process known as 'counter-doping'. If hydrogen exists in silicon at concentrations above the doping concentration, it will counter-dope the silicon until the Fermi level reaches an energy at which hydrogen exchanges electrons with the surroundings, making it a recombination center.

Along with the HID theory, there is the hypothesis that hydrogen might be part of the LeTID defect and that the degradation requires two reactants. In [44] it was reported that the firing process itself does not cause LeTID and hydrogen is required for LeTID to occur. The finding that samples fired without hydrogen containing films did not degrade, led to the conclusion that two reactants are required hydrogen and one or more defects that can be modified separately by firing.

One example of a two reactant LeTID defect has been proposed to explain degradation in multi-

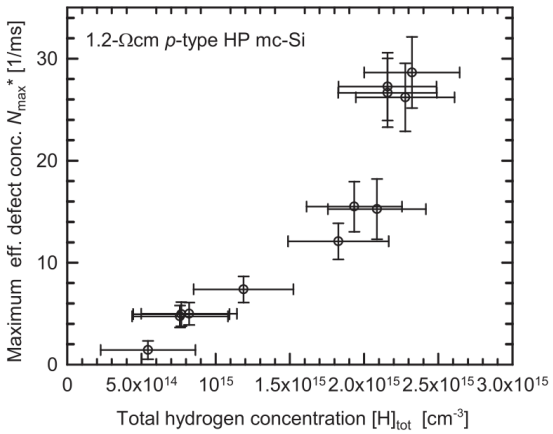

Figure 1.17: Maximum effective defect concentrations measured on neighboring mc-Si sister wafers, which were coated on both surfaces with $SiN_x : H$ films of different $Si : N$ ratios, and fired at 900°C Figure taken from [46].

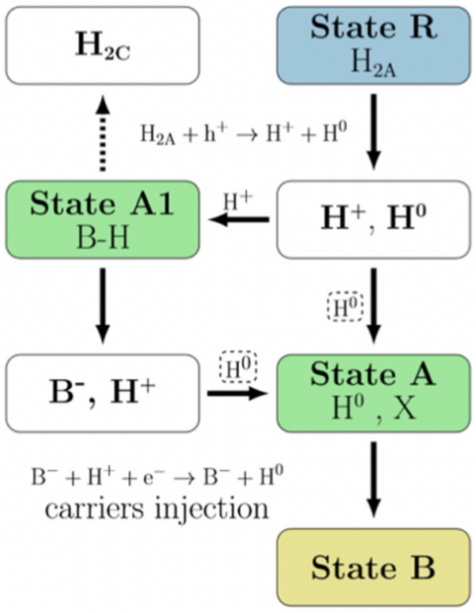

Figure 1.18: Diagram of hydrogen dynamics as part of LeTID mechanisms proposed in [45]. Here H_{2A} refers to the hydrogen molecule formed after firing and H_{2C} to the one formed after dark annealing.

crystalline boron doped silicon [45]. After finding experimental evidence that shows that B-doped samples degrade faster with respect to Ga-doped samples [50], a defect model involving atomic hydrogen, B-H and hydrogen dimer was proposed [45]. This model is based on the interaction between H_2, B-H and atomic H. In this work, it is suggested that H_2 serves as a reservoir of H, B-H acts as light-sensitive storage of H^+, and H^0 is the immediate defect precursor, as presented in figure 1.18. Information about the formation of hydrogen complexes with other dopants has not been found in the literature yet.

The low extent of LeTID in gallium doped silicon based solar cells have been experimentally studied [50, 51]. In general, the existing results show that, compared with boron doped silicon, gallium-doped silicon has a different dependence on carrier injection and dynamics. But in the case of high-temperature lighting, the same defects are activated in both gallium-doped and boron-doped silicon. However, research on LeTID in gallium-doped silicon is quite limited and more research is needed on its degradation characteristics [51].

While there are many reports of LeTID in p-type Si materials, LeTID studies in n-type Si materials are rather limited [37], but it has been found that n-type mc-Si material can also exhibit degradation behavior under illumination, although the rate and magnitude of the degradation are considerably reduced.

Interestingly, the opposite trend is observed in mc-Si materials under dark annealing conditions, where n-type mc-Si shows a faster degradation and regeneration rate than p-type mc-Si [37]. There, this behavior is explained by the different diffusivity of hydrogen in p- and n-type Si materials. Under dark annealing conditions, the higher diffusivity of hydrogen in n-type materials , out-diffuses a larger amount of hydrogen. This leads to a lower amount of hydrogen in n-type mc-Si, explaining the lower extent of LeTID [37].

In [46] a model that attributes LeTID to dissociation of metal-hydrogen pairs and regeneration due to out-diffusion of metal to surfaces and crystallographic defects is proposed. This particular model will be detailed explained in the next section.

1.3.5 The role of metal impurities in LeTID

The presence of metal impurities in silicon coming from the firing step is known. The synthesis of mc-Si induces the presence of metal impurities, but also mono-crystalline Si contains similar amounts of metal impurities compared to mc-Si [37]. Because of this reason, experimental studies such as [30, 46] point out that a metal could also play a role in LeTID.

There are several methods to isolate metal atoms in silicon known, as *gettering*. One strategy to corroborate if the presence of metal defects plays a role in LeTID is to compare a gettered and an ungettered wafers exposed to LeTID conditions. In particular, this is done for mc-Si samples in [46]. Experimentally, the number of LeTID defects in a silicon-based cell at maximal degradation extent N_{max} can be related to the initial lifetime and the minimum lifetime after completing a LeTID cycle according to equation

$$N_{max} = \frac{1}{\tau_{min}} - \frac{1}{\tau_0} \tag{1.6}$$

In [46] a higher reduction of the effective defect concentration is observed for the gettered sample, showing (not in a conclusive way though) that metals might be involved. From this observation,

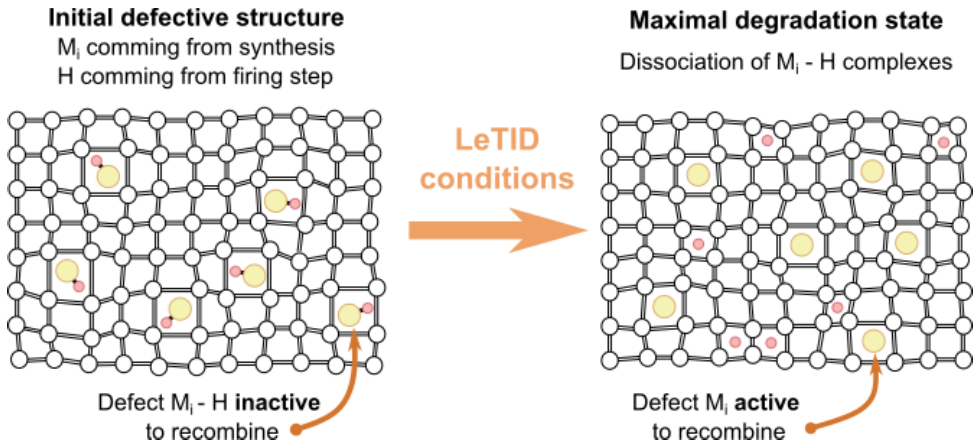

Figure 1.19: Suggested LeTID model where degradation is caused by dissociation of a metal-hydrogen ($M_i - H$) complex. The hydrogen is introduced during firing and initially passivates the metalM_i. During excess carrier injection and increased temperature, the $M_i - H$ complex dissociates and recombination-active M_i centers limit the lifetime [46].

two models are proposed in table 1.3. Their dynamics are shown in figures 4.1 and 4.2.
It was also observed that the LeTID extent decreases strongly and regeneration speeds up when decreasing the wafer's thickness of mc-Si (see figure 1.21), which might be explained by a model of diffusion of the recombination-active defects to the wafer surfaces[46], as the one shown in figure 4.2.
The lifetime regeneration is attributed to the diffusion of the recombination-active impurity to the wafer surface, where it is permanently trapped. Modeling lifetime dependence on the wafer's thickness, measured experimentally, it is possible to determine the diffusion coefficient of the impurity, which is found to be in a range of $(5 \pm 2) \times 10^{-11} cm^2 s^{-1}$ at a temperature of 75ºC [52].
Therefore, in order to spot the possible metals that are part of LeTID, a relation between diffusion coefficients (at 75ºC) of mobile impurities and the thickness of the wafer is established [46]. Cobalt and nickel diffusion coefficients where found to fit the model and, interestingly, there are recombination centers for these metals in multi-crystalline silicon.

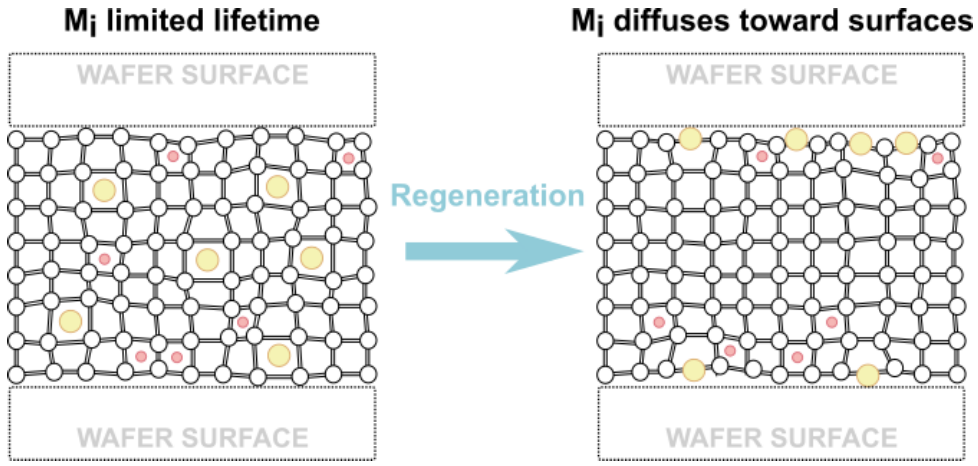

Figure 1.20: Graphic representation of sinking of the interstitial metal impurity M_i and hydrogen defects to the wafer surfaces during the lifetime regeneration state. This explains the pronounced dependence of the degradation rate on the wafer thickness [46].

Defect model 1	**Defect model 2**
Fast firing: H released from $SiN_x : H$ layer and it passivates metal impurities M_i(likely interstitially). M_i might stem from metal precipitates dissolved during the fast firing step	
$M_i - H$ complexes are no strong recombination centers or might even be completely recombination-inactive.	The metal is initially passivated with several hydrogen atoms.
During injection of minority carriers via illumination at enhanced temperature, the $M_i - H$ complex dissociates.	By carrier injection at increased temperature, some of the hydrogen atoms detach
Isolated M_i, which is assumed to be highly recombination active, reduces the bulk lifetime (the H either attaches to B, forms H_2 molecules, or attaches to other defects abondant in mc-Si).	The remaining recombination-active center is not an isolated M_i, but is in fact a metal-hydrogen complex possessing an energy level within the silicon band gap.

Table 1.3: Two different models explaining metal-hydrogen complexes dynamics regarding LeTID.

Similar thickness-dependence of mono-Si wafers is observed, but such a behavior is explained by the out-diffusion of hydrogen during contact firing, leading to a different amount of hydrogen remaining in the bulk in samples of different thicknesses after firing, and thereby affecting the LeTID kinetics [37]. Agreement of diffusion coefficient values at this temperature is only found with nickel, cobalt, and hydrogen.

Considering also diffusion of the LeTID defect in order to create the spatial distribution of degradation observed in mc-Si, the diffusion coefficient ranges of the LeTID defects can be used to spot the impurity involved in the degradation process.

According to[30], the denuded zones must form during the cooling of the firing step. Under this assumption, among the common impurities in mc-Si, the ones that have high diffusion coeffi-

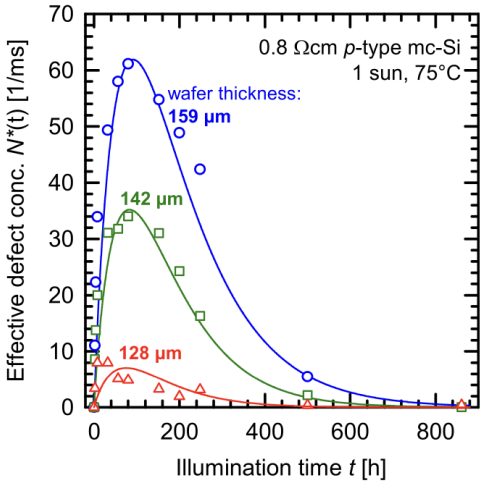

Figure 1.21: Evolution of the effective defect concentration $N(t)$ in sister mc-Si wafers of three different thickness at 1 sun illumination and 75°C. Figure taken from [46].

cients and would be able to form denuded zones are Cu, Co and Ni. Nevertheless, the solubility being quite high of Ni, similar to Cu, and all Cu complexes, would dissolve these impurities at temperatures lower than the firing temperature. Considering this criterium, Co is the only interesting candidate to cause LeTID. More information about Co defects can be found in [53, 54]. It has also been proposed that LeTID may be related to the presence of other metallic impurities such as tungsten [55], titanium and molybdenum that have been found at the maximal degradation point [56].

1.3.6 Silicon defects and vacancies

One specific type of mono crystalline silicon is float-zone (FZ) silicon, a very pure silicon. By comparing LID in FZ silicon (FZ-LID) and LeTID in multicrystalline silicon in [30] it was observed that both phenomena present the same transitions, however the processes occur in different time scales. Therefore, this study suggests that LeTID and FZ-LID have similar precursors. Such a comparison points out to interstitial silicon atoms Si_i or lattice vacancies V_{Si} as the potential LeTID defect precursors.

1.3.7 Mitigation processes

Finding mitigation processes of different degradation mechanisms has been of critical importance in the silicon-based photovoltaic industry. Both, changes in the solar cell fabrication and post-processing methods have been proposed as solutions for LeTID defect suppression.

- **The use of thin enough modules**. It has been proposed considering that the LeTID extent reduces with wafer thickness [46, 52]. Nevertheless, the proper thickness should be chosen taking into account the photon absorption properties of the material.

- **Modulation of hydrogen diffusion into the silicon bulk associated with the changes in the dielectric layers and modification of the metallization firing profile**. It has been proposed as well that hydrogen and metallic impurities are plausible causes of LeTID. The amount of hydrogen in the bulk material has proven to affect the LeTID extent and kinetics. The proper firing step and a sufficient slow cooling rate have proven to partially reduces LeTID.

- **Adapt the passivation layer** SiN_x. Studies have suggested to reduce the thickness of the SiN_x film [57] and to tune the refractive index of the SiN_x film to high (close to 3) or low (close to 1.9) values [58].

- **Phosphorus gettering of the silicon modules**. Taken into account the hypothesis of the possible role of metal impurities in LeTID, it has been shown that such a process can reduce the rate of LeTID in the silicon modules[43, 59].

- **A proper annealing treatment.** A low temperature annealing (650ºC)should be performed before metallization firing [60]; as well as dark annealing treatment after firing at a temperature between 300 and 550ºC [61]. It has also been proposed to perform annealing of the finished solar cell either under illumination, with current injection or in darkness [62]. Such

processes have shown to suppress LeTID efficiently, although they can damage the device if they are not properly optimized.

Several solar cell fabrication post-processing methods have been introduced to suppress LeTID. Nowadays, it may seem that LeTID mitigation tends to opt for the reduction in total hydrogen concentrations within the bulk of the solar cells. However, it is important to highlight that hydrogen is essential for the passivation of bulk defects, in particular of mc-Si modules for grain boundaries or Cz-Si modules to passivate BO-LID defects. It is therefore crucial to find a balance between LeTID mitigation processes and maintaining sufficient hydrogen for the passivation of other defects.

Summary of LeTID characteristics

LeTID is a type of degradation that has been observed so far in all types of silicon-based solar panels. The similarities of the LeTID cycle in different types of silicon-based modules suggest that the defects precursors along these materials are the same and that LeTID mechanisms occur in the bulk material of the module. It is believed that metal impurities and hydrogen are the main defects that affect LeTID as it has been observed that the amount of hydrogen and metal impurities changes the degradation degree of LeTID. By changing the thickness of the substrate, the thickness of the film or the firing process, the content of hydrogen in the solar cell can be altered to change the degradation degree of LeTID. Gettering metallic impurities has also proven to change the degree of LeTID degradation. Several metallic defects have been proposed as LeTID precursors, but according to measured diffusion coefficients of mobile impurities in degraded modules, cobalt and nickel are the most likely to take part in LeTID. On the other hand, a lower extent of LeTID in gallium doped silicon based solar cells have been experimentally observed. The precise role that such impurities play in causing or preventing LeTID have not been determined, neither if other non-metals impurities could be involved.

1.4 A theoretical atomic approach to understand LeTID

LeTID is one of the most common degradation mechanisms occurring in silicon-based photovoltaic technologies and, even if it was observed for the first time ten years ago, it is not yet well understood. Experimental studies have succeeded in characterizing it and identifying hydrogen and metallic impurities as possible defect precursors for LeTID. Even though hydrogen defects, some metallic impurities, and self-defects in silicon have been studied before using a first-principles approach [49, 63], a first-principles analysis to understand the complete LeTID mechanisms has not yet been presented. Therefore, theoretical atomic approaches, such as density functional theory (DFT), can provide a deeper understanding of LeTID degradation mechanisms.
In this work, we propose a LeTID study based on a DFT approach. This study aims to identify the defects that cause LeTID. Based on previous experimental observations, the most likely candidates for LeTID are hydrogen, nickel, and cobalt. We will also be interested in self-silicon defects (such as single vacancies and self-interstitials), which usually act as impurity traps. Therefore, we propose

to analyze the properties and behavior of such defects in bulk Si.
The main LeTID characteristic that we seek to retrieve and in which we base our study is the existence of degradation and recovery phases of solar cell performance. These properties are generally explained by simple models that consider three main states of the defects causing this degradation:

A. **Initial defect:** There are impurities in the bulk material in different stable states which are unable to recombine with charge carriers. Once they are exposed to LeTID conditions, they will cause degradation.

B. **Degradation:** The initial stable impurities evolve towards defects that recombine with the charge carriers. This induces a decrease in the charge-carrier lifetime. These defects are said to be in a metastable state as they evolve toward a recovered phase.

C. **Recovery:** Recombination defects are passivated until they reach final stable states.

Considering these LeTID features, along with the main characteristics of LeTID behavior, the methodology followed to propose a model for the dynamics of LeTID is based on the following hypothesis:

1. **First principles simulations in crystalline silicon will be representative to understand LeTID.** The choice of crystalline silicon as a bulk material is based on various assumptions of a common defect causing LeTID in different silicon-based wafers [12, 16]. The same characteristics of LeTID were observed for all types of silicon-based wafers, differing only in the extent of degradation.

2. **Defects taking part of LeTID are in a weak concentration along the bulk material so they are considered to be isolated from each other.** The silicon materials used for photovoltaic modules have impurity concentrations in the range of 10^{-12}–$10^{-15} cm^{-3}$ [7].

3. **Defects involved in LeTID mechanisms switch from a stable state to a metastable state and back.** Defects in the initial state A and recovery phase C are in different stable configurations and are unable to recombine with charge carriers, whereas defects in degradation phase B are in a metastable state and can recombine with charge carriers.

4. **The probability to go from state A to state B is higher than the probability to go from state B to state C.** The time to which the degradation phase occurs is considerably shorter than the time at which the recovery phase occurs [15].

The stability and electronic properties of the defects in bulk crystalline silicon were studied using DFT. The stability was analyzed by computing the defect formation energy. The electronic properties of the defective structures were analyzed by studying their band diagrams of the defective structures. It is required that defects in states **A** and **C** are unable to recombine; therefore, they might not induce an energy level in the Si band gap. Assuming that defects in state **B** might act as

traps for photogenerated carriers, they might give rise to additional electronic levels within the silicon bandgap. Therefore, the DFT results allow the categorization of defects to take part in phases **A, B** or **C**.

CHAPTER 2

Computational details for LeTID analysis

There is a current need to understand the role played by hydrogen, self-silicon defects and metallic impurities in silicon as a cause of LeTID. Such an understanding demands to predict the interaction of these defects with charge carriers in complex large-scale silicon systems. Experimentally, it is extremely complicated to measure the structural and electronic properties of these defects when they are isolated, leading to an important lack of information about their characterization properties and the exact influence they have in charge carrier recombination within different silicon materials. Atomistic modelling presents an interesting tool to study this issue because *ab initio* models such as Hartree Fock (HF) and density functional theory (DFT) can retrieve the quantum electronic interactions of these defects.

This work suggests to analyze the electronic interactions and stability of point defects in crystalline silicon within a DFT approach and, from the results obtained, to deepen our understanding of dynamic evolution over temperature changes of these defective structures with respect to experimental information available. Although there are several *ab initio* studies that have addressed the problem of hydrogen, elf-silicon defects and metallic impurities, they present important inconsistencies among each others in the description of the thermodynamic and electronic properties of such defects. We attribute these inconsistencies to the choice of Hamiltonian and the correction scheme adopted to compensate for the drawbacks of DFT methodology. Such corrections are often not clearly described and include fitting the simulated results to experimental values in an inconsistent and unjustified manner.

In this chapter, we present a brief mathematical background to understand the basics of DFT simulations, followed by the methodological aspects of our simulations. The correction scheme considered in our calculations is presented in details in order to properly evaluate the uncertainty of our approach.

2.1 Solving the problem of a system with n particles

The study of atomic systems requires the capacity to describe the properties of a well-defined collection of electrons. One of the fundamental quantities to describe it, along with the system

wavefunction, is the total energy and, more importantly, how their energy changes for different configurations. The time independent, non relativistic Schrodinger equation allows one to retrieve the energy of the system :

$$\hat{H}\Psi = E\Psi \tag{2.1}$$

In this equation, $\hat{H}$ is the Hamiltonian operator and $\Psi = \{\Psi_n\}$ is a set of solutions of the Hamiltonian. Each of these solutions Ψ_n has an associated energy eigenvalue,E_n, that satisfies the equation. The detailed definition of the Hamiltonian depends on the physical system.

Considering that an atom position is defined by the position of the nucleus **R** as well as the positions of its electrons **r**, we can define a general Hamiltonian in terms of the kinetic energy of electrons $\hat{T}_e$ and nuclei $\hat{T}_N$, as well as their potential interactions $\hat{V}$ as :

$$\hat{H} = \hat{T}_e + \hat{T}_N + \hat{V}_{eN} + \hat{V}_{NN} + \hat{V}_{ee} \tag{2.2}$$

Taking into account the mass difference between electrons and nuclei, it is possible to assume that nuclei's positions are fixed while electrons move. Therefore, to compute the ground state energy of the system, the equations that describe the electron motion and atomic nuclei are separated. This fundamental approximation is the Born – Oppenheimer approximation [64], in which :

$$\Psi(\mathbf{r},\mathbf{R}) = \Psi_{nuclei}(\mathbf{R})\Psi_{electrons}(\mathbf{r},\mathbf{R}) \tag{2.3}$$

Therefore, the Scrhodinger equation reads

$$[\hat{T}_e + \hat{T}_N + \hat{V}_{eN} + \hat{V}_{NN} + \hat{V}_{ee}]\Psi(\mathbf{r},\mathbf{R}) = E_{el}\Psi(\mathbf{r},\mathbf{R}) \tag{2.4}$$

E_{el} represents the potential energy experienced by the nuclei and, in particular, $E_{el}(\mathbf{R})$ gives the potential energy surface from which equilibrium geometry and vibrational frequencies are obtained. On the other hand, the electronic wavefunction $\Psi(\mathbf{r},\mathbf{R})$ contains the information about molecular properties such as dipole moments, polarizability, etc.

Systems with more than two electrons do not posses analytic solutions for the Schrodinger equation. In order to propose an analytic solution to equation 2.4, it would be convenient to express the electronic wavefunction in the general form:

$$\Psi(\mathbf{r}) = \phi_1(\mathbf{r}_1)\phi_2(\mathbf{r}_2)\cdots\phi_N(\mathbf{r}_N) \tag{2.5}$$

While this wavefunction form is convenient, it fails to satisfy the *antisymmetry principle*, in which a wavefunction describing fermions should be antisymmetric with respect to the interchange of any set of space-spin coordinates [65]. To propose a form of the wavefunction in which the antisymmetry principle is fullfilled, we propose to change our notation from spatial orbitals $\psi(\mathbf{r})$ to spin orbitals $\chi(\mathbf{x})$ in which **r** are the spatial coordinates of the electron while $\mathbf{x} = (\mathbf{r}, s)$ are the spatial-spin coordinates.

To satisfy the *antisymmetry principle*, the many-electron wave function takes the form of a Slater determinant of single electron spin orbitals [66]

$$\Psi = \frac{1}{\sqrt{N!}} \begin{vmatrix} \chi_1(\mathbf{r}_1) & \cdots & \chi_N(\mathbf{r}_1) \\ \vdots & & \vdots \\ \chi_1(\mathbf{r}_N) & \cdots & \chi_N(\mathbf{r}_N) \end{vmatrix} \tag{2.6}$$

As a consequence of expressing the wavefunction in this form, the electrons are all indistinguishable and each electron is no longer associated to a specific orbital, but rather to a set of orbitals.

2.1.1 The Hartree Fock approximation

Seeking to write the Hamiltonian of the system in a simpler way, it can be expressed as the sum of monoelectronic Hamiltonian $\hat{H} = \sum_i \hat{h}_i$. We define the one electron operator as can be written in terms of the Hamiltonian associated to each electron $\hat{h}_i = \hat{T}_i + \hat{V}_i^{eN}$ and the two-electron operator $\hat{v}_i^{ee} = \hat{V}_{ee}$. The kinetic and potential energy terms in atomic units satisfy $\hat{T} = -\frac{1}{2}\nabla^2$, $\hat{V}_{eN} = \sum_A \frac{Z_A}{\mathbf{r}_{iA}}$ and $\hat{V}_{ee} = \sum_{i>j} \frac{1}{\mathbf{r}_{ij}}$.
The electronic Hamiltonian is then written as

$$\hat{H}_{el} = \sum_i \hat{h}_i + \sum_{i<j} \hat{v}_{ij} + \hat{V}_{NN} \tag{2.7}$$

We can take out the term $\hat{V}_{NN}$ since it is just a constant for the fixed set of nuclear coordinates **R** and it only shifts the eigenvalues. Nevertheless, the problem persists as the two-electron operator is not divisible into single electron terms.

Hartree proposed to replace all interactions experienced by an electron with an average or effective interaction, called a **mean field** [67]. By doing so, the second term can be separated into a set of one-electron terms:

$$\hat{H}_{el} = \sum_i \hat{f}_i, \qquad \hat{f}_i = \hat{h}_i + \hat{v}_i^{HF} \tag{2.8}$$

$\hat{v}_i^{HF}$ is the average potential that the ith electron experiences because of the other electrons, and $\hat{f}$ is a one-electron operator called the **Fock operator**.

Using the Fock operator, it is possible to rewrite the electronic Shrodinger equation as a set of one-electron equations. The mean field operator $\hat{v}_i^{HF}$ can be split into two components

$$\begin{aligned} \hat{v}_i^{HF}(\mathbf{x}) &= \hat{v}_i^{Coul}(\mathbf{x}) + \hat{v}_i^{XC}(\mathbf{x}) \\ \hat{v}_i^{Coul}(\mathbf{x}_1) &= \sum_{i \neq j} \hat{J}_j(\mathbf{x}_1) \\ \hat{v}_i^{XC}(\mathbf{x}_1) &= \sum_{i \neq j} \hat{K}_j(\mathbf{x}_1) \end{aligned} \tag{2.9}$$

The operators $\hat{J}$ and $\hat{K}$ are know respectively as the Coulomb and exchange operators, they are defined as:

$$\hat{J}_j(\mathbf{x}_1) = \int d\mathbf{x}_2 |\chi_j(\mathbf{x}_2)|^2 r_{12}^{-1} \tag{2.10}$$
$$\hat{K}_j(\mathbf{x}_1)\chi_i(\mathbf{x}_1) = \left[\int d\mathbf{x}_2 \chi_j^*(\mathbf{x}_2) r_{12}^{-1} \chi_i(\mathbf{x}_2)\right] \chi_j(\mathbf{x}_1)$$

The Coulomb operator represents the exact Coulomb interaction between two electrons. In the Hartree-Fock approximation, the ith electron in orbital χ_i experiences a one-electron potential coming from the orbital χ_j. The summation is over all spin-orbitals. On the other hand, the exchange operator results from the exchange-correlation between electrons with parallel spins. Because the only interaction between electrons is coulombic, HF overestimates the ionic character of the system, leading to the overestimation of semiconductor and insulator band gaps. The lack of information regarding the electronic interaction for the HF approach leads to the definition of the electronic correletaion as

$$E_{corr} = E_{real} - E_{HF} \tag{2.11}$$

By use of the variational method, the Hartree-Fock approximation determines the set of spin orbitals which minimize the energy and are closest to the true wavefunction. The molecular orbitals can be obtained numerically as a linear combination of a set of given basis functions, usually atom-centered Gaussian type functions. The initial orbitals guess is refined iteratively. This methodology to solve the equations in the Hartree-Fock approach is called a self-consistent-field (SCF) approach.
To express the energy of the system within the Hartree fock approximation we simplify the notation of the many electron wavefunction considering that the construction of a Slater determinant requires only the list of occupied spin orbitals. Therefore, we can write it in a short hand using a ket notation $|\chi_i\chi_j\cdots\chi_k\rangle$ or even more simply as $|ij\cdots k\rangle$.

Finally, the energy of the electronic system is given by $E_{el} = \langle\Psi|\hat{H}_{el}|\Psi\rangle$, and therefore the **Hartree Fock energy** is given by

$$\begin{aligned} E_{HF} =& \sum_i \left(\langle i|\hat{h}|i\rangle + \langle i|\hat{v}^{Coul}|i\rangle + \sum_{j>i} \langle i|\hat{v}^X|i\rangle \right) \\ =& E_{core} + E_{Coul} + E_X \end{aligned} \tag{2.12}$$

2.1.2 Density Functional Theory

Even though the solution of the Schrodinger equation leads to the understanding of the electronic distribution and the energy of the system, the quantity of physical interest is really the probability that a set of N electrons in any order have coordinates $\mathbf{r}_1,...,\mathbf{r}_N$. This probability is equal to $\Psi^*(\mathbf{r}_1,...,\mathbf{r}_N)\Psi(\mathbf{r}_1,...,\mathbf{r}_N)$.

The **density of electrons** at a particular position in space $n(\mathbf{r})$, is a closely related quantity to the probability $\Psi^*(\mathbf{r}_1,...,\mathbf{r}_N)\Psi(\mathbf{r}_1,...,\mathbf{r}_N)$. This can be written in terms of the individual electron wave functions as

$$n(\mathbf{r}) = 2\sum_{i=1}^{N} \Psi*(\mathbf{r}_1,...,\mathbf{r}_N)\Psi(\mathbf{r}_1,...,\mathbf{r}_N) \tag{2.13}$$

The factor of 2 comes from the Pauli exclusion principle for electrons. The electron density $n(\mathbf{r})$, which is a function of only three coordinates, contains a great amount of information that is actually physically observable from the full wave function solution to the Schrodinger equation, which is a function of $3N$ coordinates.
The entire field of density functional theory rests on two fundamental mathematical theorems proved by Kohn and Hohenberg in the mid-1960s [68].

First Hohenberg-Kohn theorem: The ground-state energy from Schrödinger's equation is a unique functional of the electron density. for non-degenerate states. Therefore, there exists a one-to-one mapping between the ground-state wave function and the ground-state electron density.

Second Hohenberg–Kohn theorem: The electron density that minimizes the energy of the overall functional is the true electron density corresponding to the full solution of the Schrödinger equation.

Then, it is possible to solve the Schrödinger equation by finding a function of three spatial variables, the electron density, rather than a function of 3N variables, the wave function. Thus, all properties of the electronic system and in particular any expectation value of an observable $\hat{O} = \langle\Psi_0|\hat{O}|\Psi_0\rangle$ are functionals of $\rho(\vec{r})$, $O[\rho]$ for the observable $\hat{O}$.
If we take the Kohn and Hohenberg theorem, the ground-state energy E can be expressed as the functional $E[n(r)]$, where $n(r)$ is the electron density. From equation 2.13, and cosidering that the enrgy is the expectation value of the DFT Hamiltonian, we have that

$$E[n(r)] = E_{known}[n(r)] + E_{XC}[n(r)] \tag{2.14}$$

where $E_{known}[n(r)]$ is given by

$$E_{known}[n(r)] = \underbrace{-\frac{1}{2}\sum_i \int \Psi_i^* \nabla^2 \Psi_i d^3r}_{\text{electron kinetics energies}} + \underbrace{\underbrace{\int V(\mathbf{r})n(\mathbf{r})d^3r}_{\text{electron - nuclei}} + \underbrace{\frac{1}{2}\int\int \frac{n(\mathbf{r})n(\mathbf{r'})}{|\mathbf{rr'}|}d^3r d^3r'}_{\text{electrons}} + \underbrace{E_{ion}}_{\text{nuclei}}}_{\text{Coulomb interactions}} \tag{2.15}$$

The other term in the complete energy functional, $E_{XC}[\{\Psi_i\}]$, is the exchange–correlation functional, and it is defined to include all the quantum mechanical effects that are not included in the "*known*" terms. The main problem is to get some good approximation of the exchange and correlation description.

Several approximations can be used to define the exchange-correlation functional. The simplest is where this functional is derived exactly from the uniform electron gas. In this situation, the electron density is constant at all points in space. This approximation uses only the local density to define the approximate exchange–correlation functional, so it is called the *local density approximation* (LDA) [69].
The best known class of functionals after the LDA uses information about the local electron density and the local gradient in the electron density; this approach defines a *generalized gradient approximation* (GGA). The GGA approximation takes some combination of $n(\mathbf{r}), \nabla n(\mathbf{r}) \nabla^2 n(\mathbf{r})$ so in general, it thus reads [70] :

$$E_{XC}^{GGA}[n(\mathbf{r})] = \int d\vec{r} \mathscr{F}(n(\mathbf{r}), \nabla n(\mathbf{r}), \nabla^2 n(\mathbf{r}), ...) \tag{2.16}$$

where $\mathscr{F}(n(\vec{r}), \nabla n(\vec{r}), \nabla^2 n(\vec{r}))$ is a an effective one electron exchange-correlation energy.
Because there are many ways in which information from the gradient of the electron density can be included in a GGA functional, there is a large number of distinct GGA functionals. One of the most widely used functionals in calculations involving solids is the Perdew–Burke–Ernzerhof functional (PBE) [71] and it will be used for the calculations along this work. As the basic DFT approximations are based on the assumption that the electron distribution is more delocalized and homogeneous like in metals, it thus underestimates the band gap for the case of semiconductors.

2.1.3 Hybrid functionals

Both HF and DFT methods are approximated solutions to the energy or electron distribution of an atomic system. Hybridization of DFT with Hartree–Fock (HF) exchange was introduced by Axel Becke in 1993 [72] to improve the calculation of molecular properties, such as atomization energies, bond lengths, and vibration frequencies, which tend to be poorly described with the two previous methods. Both HF and DFT present an important error when describing the band gap of semiconductors. While HF over estimates the band gap, DFT under estimates it. Therefore, hybrid functionals are adequate to correct this issue.
The simplest form of the hybrid approach proposes a linear combination of the exact exchange of HF with DFT exchange-correlation terms [73]. The percentage of HF mixed with the DFT functionals is giving by the mixing parameter α :

$$E_{XC} = (1-\alpha)E_{XC_{DFT}} + \alpha E_{XC_{HF}} \tag{2.17}$$

A pragmatic approach is to fit the mixing parameter to adjust a specific parameters of the system, for example band gap values, vibration energies or dielectric constants, allows one to reproduce the desired properties for a given material.

2.2 Methodological aspects

In the following section we will address the computational details used to simulate the defects in crystalline silicon that we consider to be related to LeTID. Experimental studies have proven two

important LeTID features: first, LeTID is caused by defects in the bulk material of solar modules, i.e. the silicon material; and second, there exists a common LeTID defect in all the varieties of silicon wafers [12, 16].

In order to go through the computational details of the simulations performed along this work, we first present the most relevant characteristics of crystalline silicon in this context. The multiscale approach that we propose to reproduce the behavior of the possible LeTID precursors requires, in the first instance, density functional theory (DFT) computations. Such results seek to understand the electronic properties of defective structures taking into account the quantum interactions of atoms. For this aim, the commercial code `CRYSTAL17` [74] was used. The considerations within the DFT methodology are discussed as a second subject in this chapter.

2.2.1 Crystalline silicon

Monocrystalline silicon is a form with the diamond crystal structure, the space group of crystalline silicone is Fd3m. The disposition of the silicon atoms in the crystalline structure is shown in figure 2.1. The primitive cell contains two silicon atoms (figure 2.1c) which corresponds to a unit or conventional cell (figure 2.1a)containing 8 atoms at corners, 6 atoms in faces at a hight of $\frac{1}{2}L$ and 4 atoms within cell. The experimental value of the lattice parameter L is 5.431Å [75].

Crystalline silicon is an indirect semiconductor with an indirect band gap of 1.11 eV at 300 K, or 1.17 eV at 0 K [76]. As typical for semiconductors, its resistivity drops as temperature rises. The dielectric constant (ϵ) is an essential piece of information for semiconductors, defined as the ratio of the permittivity of a substance to the permittivity of free space. It is an expression of the extent to which a material concentrates electric flux. In the case of silicon, the total dielectric constant has a value of $\epsilon = 11.7$ at 300 K, or 11.4 at 0 K[76].

This work aims to study understand the role played by impurities in cristalline silicon in charge recombination processes. A catalog of the defects that will be treated in this work is presented in figure 2.3.

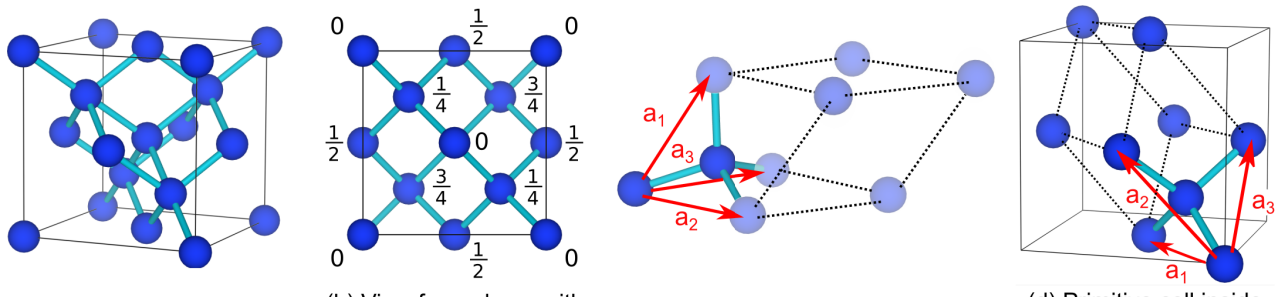

(a) Conventional cell (b) View from above with coordinate z of each atom (c) Primitive cell with two atoms (d) Primitive cell inside the conventional cell

Figure 2.1: Crystalline structure of Silicon. We can observe the primitive and conventional cells.

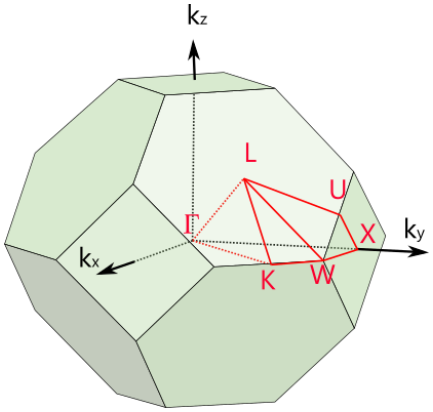

Figure 2.2: First Brillouin zone and main points for FCC geometry.

Points	(u,v,w)	$[k_x,k_y,k_z]$	Remarks
Γ	$(0,0,0)$	$[0,0,0]$	Origin of k space
X	$(0,\frac{1}{2},\frac{1}{2})$	$[0,\frac{2\pi}{a},0]$	Middle of square faces
L	$(\frac{1}{2},\frac{1}{2},\frac{1}{2})$	$[\frac{\pi}{a},\frac{\pi}{a},\frac{\pi}{a}]$	Middle of hexagonal faces
W	$(\frac{1}{4},\frac{3}{4},\frac{1}{2})$	$[\frac{\pi}{a},\frac{2\pi}{a},0]$	Middle of edge shared by two hexagons and a square
U	$(\frac{1}{4},\frac{5}{8},\frac{5}{8})$	$[\frac{\pi}{2a},\frac{2\pi}{a},\frac{\pi}{2a}]$	Middle of edge shared by a hexagons and a square
K	$(\frac{3}{8},\frac{3}{4},\frac{3}{8})$	$[\frac{3\pi}{2a},\frac{3\pi}{2a},0]$	Middle of edge shared by two hexagons

Table 2.1: Symmetry points in k-space

The electronic properties of the structures containing the potential LeTID defects help to determine the possible interactions of such defects with charge carriers. Therefore, their band structures are analyzed in this study. In order to help the interpretation of these diagrams, figure 2.2 represents the Brillouin zone for silicon, which corresponds to the Brillouin zone for a FCC geometry. The band indexes specified in the band structures of this work refer to the symmetry points described in table 2.1.

2.3 Retrieving silicon properties with DFT

When performing DFT simulations, the choice of Hamiltonians is crucial to properly reproduce the structural and electronic properties of crystalline silicon. Along this work, the DFT calculations were conducted using the Hamiltonian described by a hybrid functional based on PBEsol [71]. The choice of this hybrid potential was based on the accuracy to reproduce crystalline silicon, observed in previous studies[77].

DFT calculations are computationally demanding, so it is necessary to guarantee the correct numerical convergence of the results while optimizing their computational time. In order to do this optimization, we focused on the following aspects: the precision in the total energy, the sampling of k points in reciprocal space, and the tolerance parameter used in our computations.

Figure 2.3: Catalog of defects that are simulated within the DFT framework along this work. Complexes might refer to molecules or different atoms complexes.

The number of iterations performed is controlled by the **precision in the total energy**, which estimates how close the current solution is to the exact solution.

The proper **sampling of k points** ensures the convergence of the part of the calculations that are defined in reciprocal space. Here, integrals are evaluated only over the possible values of **k** in the Brillouin zone, so choosing the right number of k points to represent it is crucial.

The **tolerance parameter** $ITOL$ controls the accuracy of the calculation of the two electrons coulombic interaction term. When the overlap between two atomic orbitals is smaller than 10^{-ITOL}, the corresponding integral is either neglected or evaluated in a less precise way.

2.3.1 The choice of Hamiltonian

Results in DFT calculations depend on the choice of exchange correlation functionals, which will describe the physical behavior of the system. Here, we have chosen the hybrid functional PBEsol to describe crystalline silicon as well as structures containing point defects such as hydrogen, self silicon defects, and metallic impurities. In order to understand the consequences of using a hybrid functional, we first analyze the performance of a HF and DFT Hamiltonian. Regarding DFT, we consider the functionals PBEsol (purely DFT) and PBEsol0, a hybrid functional of PBEsol with 25% of HF contribution by default.

Figure 2.4 presents numerical evidence of the convergence of results in terms of the sampling of the reciprocal space and the tolerance parameter. The energy cutoff value used in all DFT calculations along this work is 10^{-6} a.u., which is set to by default in the `CRYSTAL17` code. A geometry optimization was performed systematically during all simulations. This process minimizes the

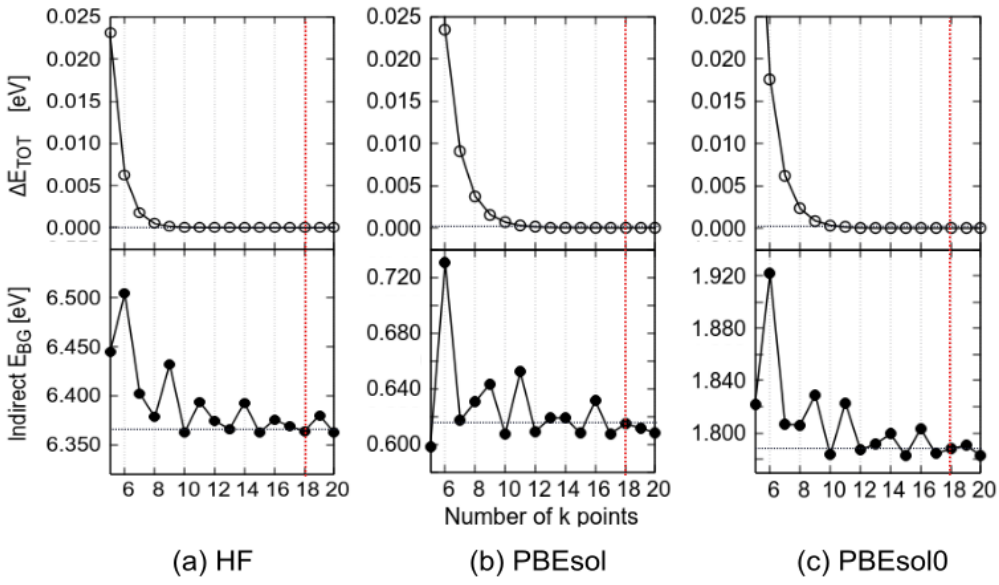

Figure 2.4: Energy and indirect gap convergence as a function of the number of k points for sampling the reciprocal space.

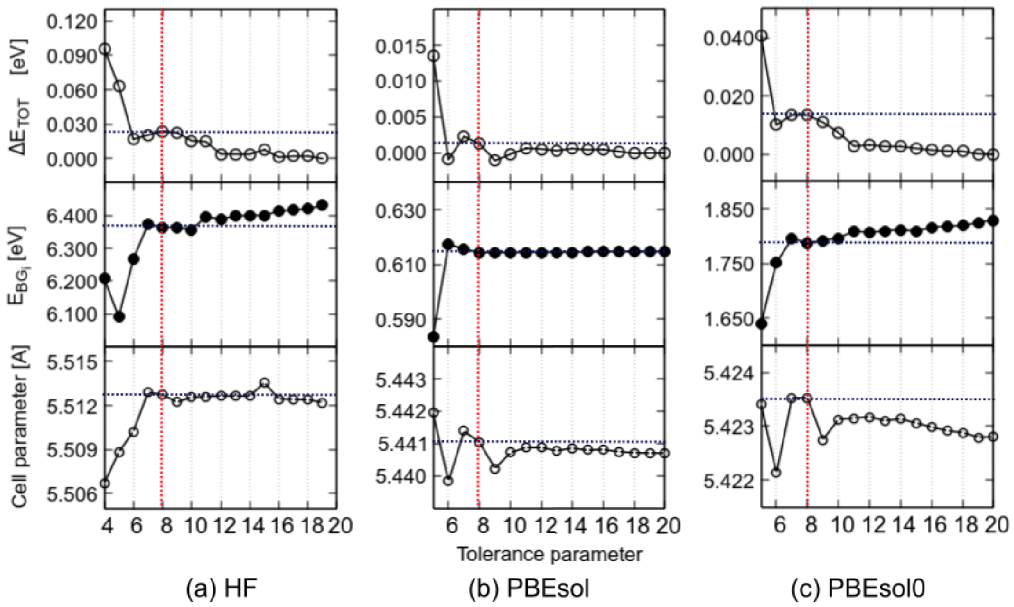

Figure 2.5: Convergence of total energy difference, indirect band gap energy, and cell parameter as a function of the tolerance parameter factor.

energy of the system by changing the system's geometry (the nuclear coordinates and the lattice vectors). Figure 2.4 shows the convergence of the total energy of the system and the energy band gap value with respect to the number of k-points. We define ΔE_{TOT} as difference between the computed value of the total energy of the system and the converged value, taking as converged value $E_{TOT_{k=20}}$. Considering as the energy convergence criteria the cutoff energy ($10^{-6} a.u.$), the optimized number of k points is chosen to be 18 for the three cases.

A particular feature of these results is the irregularity of the variation of the band gap energy as a function of the number of k points. It is originated from the sampling of the $k-$points along with the indirect nature of the Si bandgap. This irregular variance in the value of the energy band gap with respect of the number of k points results in a numerical error in the band gap of $E_{BG_{error}} = 0.01 eV$. When we only consider the changes in total energy of the system and indirect band gap energy with respect to the tolerance parameter (figure 2.5), the energy convergence criteria with respect to the cutoff energy is no longer good enough for the optimization. Therefore we took

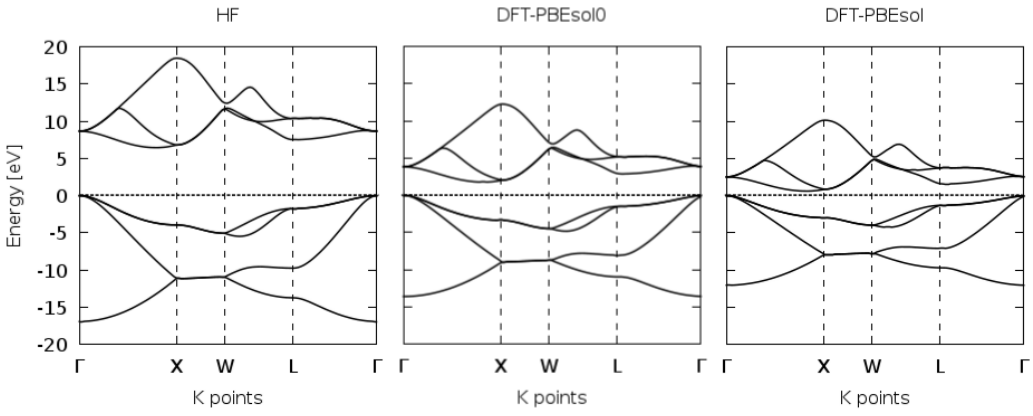

Figure 2.6: Si-crystalline band structure for HF and DFT hamiltonians.

into account the convergence of the cell parameter while performing a geometric optimization for each calculation. We considered as a criterion a difference of less than 0.001 Å with respect to the converged cell parameter value. As observed in figure 2.5, the tolerance parameter chosen to be the optimum is 8, for which the numerical errors are $E_{BG_{error}} = 0.01eV$, $E_{lattice_{error}} = 0.001$Å, and $E_{Total_{error}} = 0.005eV$.

The converged values of the crystalline silicon properties obtained by each Hamiltonian are presented in table 2.2, with a the cell parameter, ω the phonon frequency at the gamma point, and ϵ the dielectric constant. There is an important difference between the computed indirect band gap values, also observed in the electronic band structure computed for each Hamiltonian (figure 2.6).

From table 2.2 and figure 2.6 we observe a clear over estimation of the band gap for the HF Hamiltonian. This is because HF does not consider any correlation between electrons beyond the Pauli's exclusion principle. On the other hand, the purely DFT-PBEsol functional assumes that electron distribution is more delocalized and homogeneous, resulting in an under estimation of the band gap. Finally, we have found that the DFT-PBEsol0 hybrid functional, with a 25% of HF contribution, is in the middle of both. Therefore an optimization of the mixing parameter is needed in order to properly reproduce the band gap energy value.

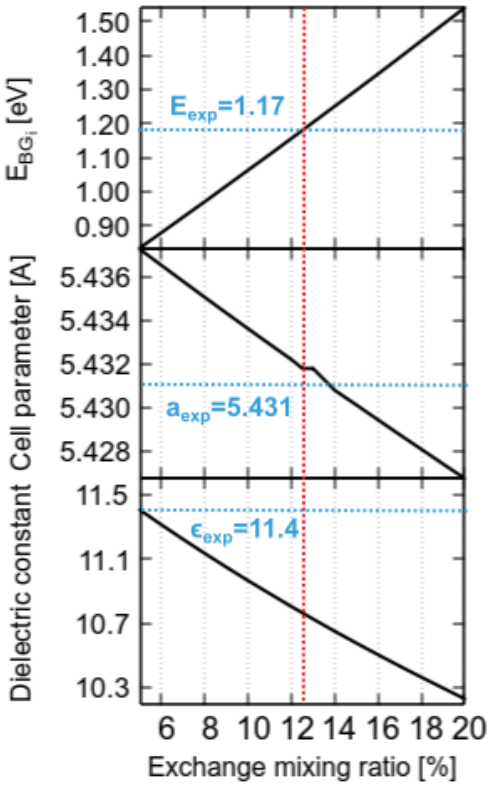

Figure 2.7: Crystalline Si properties (indirect band gap value, cell parameter and dielectric constant) dependence on functional mixing parameter.

	a [Å]	ω $[cm^{-1}]$	ϵ	E_{BG_i} **[eV]**
HF	5.512	583	7.3	6.44
PBEsol	5.423	522	9.9	0.62
PBEsol0	5.440	548	11.9	1.78
PBEsol$_{12.5}$	5.4317	535	10.7	1.17
Experimental	5.431	520	11.4	1.17

Table 2.2: Electronic properties calculated with different hamiltonians compared to experimental data [78].

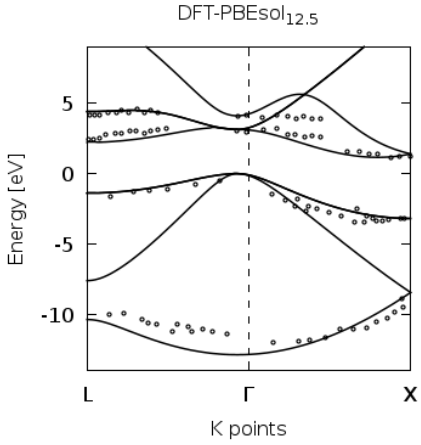

Figure 2.8: Electronic band structure (PBEsol$_{12.5}$) compared with experimental data [79].

2.3.2 Hybrid functional performance

In order to optimize the hybrid mixing parameter, and according to the results of numerical convergence observed in section 2.3.1, we used an energy cutoff of $10^{-6} a.u.$, 18 k points to sample the reciprocal space and a tolerance parameter of 8. Figure 2.7 presents the crystalline silicon properties dependence on the PBEsol hybrid exchange-correlation mixing parameter, where the percentage refers to the contribution of the HF Hamiltonian. According to these results, the DFT-PBEsol0 hybrid functional was optimized to reproduce the experimental value of crystalline silicon's band gap, so the extent of Hartree-Fock is $HF_{\%} = 12.5$.
The band structure of crystalline silicon obtained with $\text{PBEsol}_{12.5}$ is presented inf figure 2.8 along with experimental values (dots) [79]. We observe that the electronic structure is in good agreement with experiments, therefore $\text{PBEsol}_{12.5}$ will be used in the following.

2.4 Simulation of defective structures

The following discussion about our methodology for modeling LeTID defects by the use of DFT focuses on the modeling of point defects in a perfect silicon crystal. As we consider that the defect perturbation in the crystal is small due to its local nature, their structural and electronic impact is confined in the finite region close to the defect, called the *defect zone*. The rest of the system was treated as a perfect crystal (with a perfect periodic structure). To study the LeTID defect, we chose a supercell approach, which is discussed at the beginning of this section, along with its main disadvantages. An analysis of the computation of the formation energy of the defects is presented. This is an important quantity for two main reasons: first, it allows the determination of the stability of the defects studied, and second, it is used as a criterion to confirm that the defect zone is contained within the used supercells. Here, we choose a supercell size for which the formation energy and bandgap values converge. The main corrections concerning the supercell drawbacks are discussed next and are included in the formation energy computation.
Finally, to ensure the stability of the defective structures studied, additionally to a geometry optimization, the phonon-frequencies are analyzed for each structure. Such an analysis is described in details at the end of the section.

2.4.1 Supercell approach

A **supercell** is a large unit cell defined as a linear combination of the primitive unit cell vectors. The new translation vectors $\mathbf{a}'_1, \mathbf{a}'_2, \mathbf{a}'_3$ are defined in terms of the primitive cell vectors $\mathbf{a}_1, \mathbf{a}_2, \mathbf{a}_3$:

$$\begin{aligned} \mathbf{a}'_1 &= \epsilon_{11}\mathbf{a}_1 + \epsilon_{12}\mathbf{a}_2 + \epsilon_{13}\mathbf{a}_3 \\ \mathbf{a}'_2 &= \epsilon_{21}\mathbf{a}_1 + \epsilon_{22}\mathbf{a}_2 + \epsilon_{23}\mathbf{a}_3 \\ \mathbf{a}'_3 &= \epsilon_{31}\mathbf{a}_1 + \epsilon_{32}\mathbf{a}_2 + \epsilon_{33}\mathbf{a}_3 \end{aligned} \tag{2.18}$$

with ϵ_{ij} integer numbers.

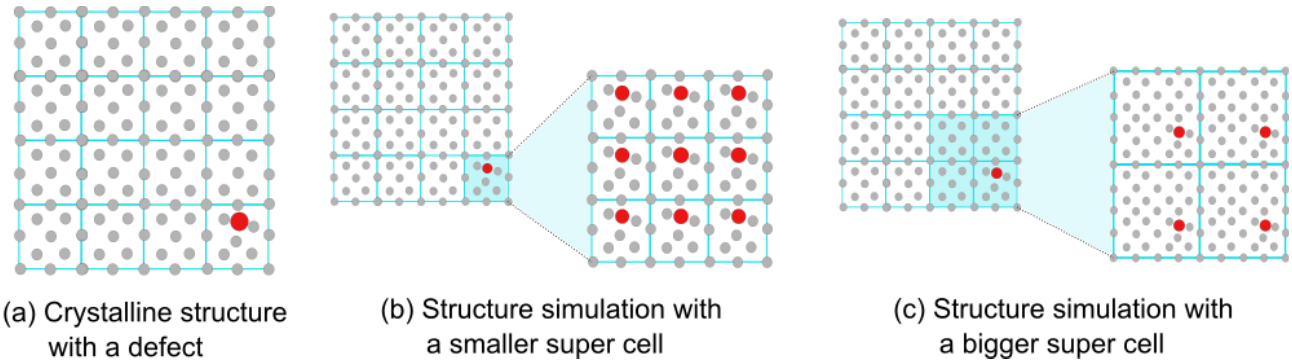

Figure 2.9: Schematic example of a local defect in a two-dimensional lattice as modeled by the supercell approach.

Number of Si atoms	32	64	128	216	432
k points	10	8	5	4	3

Table 2.3: Number of k points for converged results with respect to the number of atoms in the supercell.

The supercell approach simulates a periodic arrangement of the defect zone, represented by a defect within a supercell. Figure 2.9 represents the supercell approach : by starting from the perfect crystal, a defect is inserted in one of the unit cells (figure 2.9a); we could therefore determine a supercell as a defect zone and use it as a *building block* for the periodic structure. In figure 2.9b and 2.9c, two different sizes of supercells are represented. We consider a weak impurity concentration in the bulk material, which implies that impurities are isolated one from another. Therefore, to reproduce the characteristics of a defect, we look for a specific size of supercell for which defects from adjacent supercells do not interact mechanically or electronically, with the one within the neighbor supercell. In such a way, defects can be considered isolated. This requires a distance among defects large enough to reduce their electrostatic interaction to negligible values. Therefore, computed properties are required to converge with the supercell size, which ensures that the interaction between defects in neighboring cells can be neglected. As mentioned before, we choose the formation energy and band gap values as criteria for the supercell size.

Taking into account that an increase in the volume in real space corresponds to a decrease in volume in reciprocal space, it is necessary to optimize the number of k points used in calculations involving supercells. For the systems that are used in the present work (from 8 to 512 atoms), the number of k points was optimized according to table 2.3.

DFT computations involving supercells are computationally demanding. For this reason, the code `CRYSTAL17` has two paralellized versions: `Pcrystal` is the basic parallel version developed to be used on clusters, it is optimal for computations involving less that 100 atoms. On the other hand, `MPP Crystal` (massively parallel crystal) distributes data and tasks to cores more efficiently than `Pcrystal` and is particularly suitable for large unit cell cases (more than 100 atoms) with large memory requirements. All simulations of defective structures require the optimization of the number of nodes with respect to the computational time. They were performed by using the EDF High Performance Computing Capabilities.

2.4.2 Drawbacks of the supercell approach and how to face them

The main drawbacks of the supercell approach come from the artificial periodicity of the defects in the crystalline structure. The first feature is the difference between the defect concentrations in the simulated and real materials. As mentioned in Section 2.4.1, to reproduce the properties of a material with a weak concentration of impurities, defects must be considered to be isolated from one another. This requires the use of large supercells; however, the computational cost increases rapidly with the system size. In practice, the supercell size is chosen according to the convergence of the formation energy and bandgap values. Nowadays, in most calculations for different systems, supercells fulfilling this criterion contain up to a few hundred atoms for different systems[80], which implies that for each few hundreds of atoms there is one impurity. The defect density in real crystals is, of course, much lower than that reproduced using the supercell approach. This unrealistically high defect density prevents us from extracting any reliable information related to the extrinsic properties of the material on a large scale (larger than the defect zone), but it allows us to see the dynamics and local structure around the defects, and we achieve a converged value of the bandgap and formation energy with respect to a certain size of the supercell.

The convergence of the formation energy and band gap values diminishes, to a certain extent, the interaction of a defect with its periodic images, but does not ensure that it vanishes completely. Defect interactions with their periodic images can be mechanical or electrostatic. Mechanical interactions are usually complicated to account for and negligible for supercells with a size of ≈ 15Å [80] therefore, they will not be treated in this work. We will only consider the electrostatic interactions and their respective corrections.

One sign of electronic interactions between defects within neighboring supercells is *dispersion* in defect-induced electronic levels in the defect bands [80]. In the computations presented in this work, supercells containing 216 silicon atoms were observed to be around 0.1 eV.

In a defect-containing supercell, the states of the band gap edge are affected by the defect, which reduces the accuracy of the placement of the top of the valence band (TVB) and the bottom of the conduction band (BCB) values. Furthermore, the location of the energy level ϵ_{TVB} depends on the type and charge state of the defect due to finite size effects and differs from that of the crystalline supercell. To avoid this problem, the band edge positions can be determined by aligning a reference level between the defective structure and perfect crystal, which is discussed in Section 2.4.4.

In addition, complications arise when treating charged defects. To avoid divergences in the electrostatic energies when simulating a charged defect in a supercell, `CRYSTAL17` calculations introduce a homogeneous neutralizing background charge to the supercell, which enables the evaluation of electrostatic energies [81]. However, this introduces an electrostatic interaction between the periodic charge distribution in the supercells and the background, which vanishes only for *infinitely* large supercells. Such an electrostatic correction ΔE_{elect} corresponds to the Coulomb interaction between two localized charged densities separated by a distance L, which is the lattice parameter of the defective cell. Because such charge distributions are not isolated systems, their Coulomb interaction is written in terms of the Madelung constant, α_m [76],

$$\Delta E_{elect} = -\frac{\alpha_m q^2}{2\epsilon L} \tag{2.19}$$

where ϵ denotes the dielectric constant of the host material. The correction ΔE_{elect} is called the Markov-Payne correction scheme [82]. In the case of crystalline silicon, the Madelung constant value is $\alpha_m = 2.885$ [80] and the computed dielectric constant for $PBEsol_{12.5}$ is 10.762. With these values, the correction was determined to be $\Delta E_{elect} = -q^2 \times 0.118eV$ for $3 \times 3 \times 3$ supercells ($L =$ 16.295Å).

2.4.3 Formation energy

The formation energy E_f of a defect D is defined as the energy difference between the investigated system and the components in their reference states. It is a quantity that allows to study the stability of the defective structure and its convergence is used as criterion to choose the size of supercells in our DFT calculations. Evidence of such convergence will be presented in the following chapters, when the properties of such structures will be discussed.

The formation process of a point defect can be described by the reaction:

$$Crystal + React_A \rightarrow Defective + React_B \tag{2.20}$$

where $Crystal$ is the perfect crystal and $Defective$ is the defective system. $React_A$ and $React_B$ are the reactants and the products, respectively, and are typically atomic or molecular species. The reaction requires a certain amount of energy to occur, which is called **formation energy.**

$$\Delta E_{form} = E_{Def} + E[R_B] - E[Cryst] - E[R_A] \tag{2.21}$$

In general, the formation energy equations for the defects treated in this work will be presented along with the defect description. As mentioned before, the defects treated here are point defects that can be in an interstitial or substitutional position in the crystalline silicon structure. In the case of the formation of a substitutional defect, for example, in equation 2.20 $React_A$ represents the substituting atom and $React_B$ would be the silicon atom that is substituted. As well, the case of a neutral interstitial atom A ($React_A$) does not have a reactant term $React_B$. In the process of creating a vacancy, the term containing A is absent and B is the leaving atom.
The treatment of defects in different charge states complicates the choice of the right reference states for electrons. In order to address this problematic we consider the case of an interstitial point charged defect D; the reaction that corresponds to their formation process is given by

$$Crystal + D^0 \rightarrow Defective[D^q] \pm ne^- \tag{2.22}$$

with D^0 the defect in the neutral charge state and D^q the charged defects after losing or gaining n electrons. The formation energy of such a defect can be computed from the total energy of the bulk and defective structures obtained from DFT calculations by

$$\Delta E_{form}[D^q] = E_{TOT}[Si, D^q] - E_{TOT}[Crystal] - E[D^0] \pm E[ne^-] \tag{2.23}$$

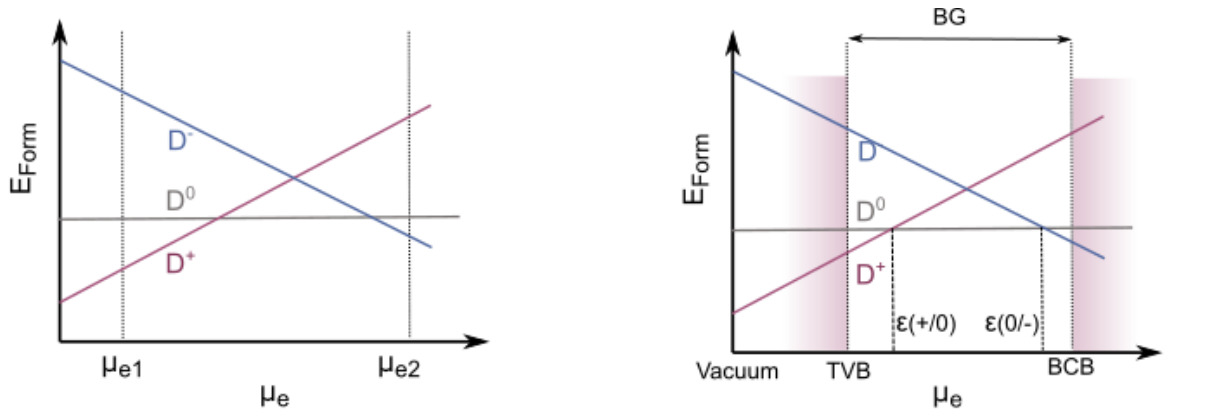

(a) The choice of μ_e defines the stability of different charged states of defect *D*

(b) Formation energy for different charge states of defect *D* considering the band gap edges

Figure 2.10: Formation energy ΔE_{form} as a function of the electron chemical potential μ_e. (a) The stability of different charged defects D^q depends on the electron chemical potential considered. For μ_{e1}, $\Delta E_{form}[D^+] < \Delta E_{form}[D^0] < \Delta E_{form}[D^-]$, whereas μ_{e2} satisfies $\Delta E_{form}[D^+] > \Delta E_{form}[D^0] > \Delta E_{form}[D^-]$.(b) Formation energies with respect to the band gap edges. The ionization levels $\epsilon(+/0)$ and $\epsilon(0/-)$ lie inside of the bandgap (BG).

The energy of the reactant $E[D^0] = \sum_i n_i \mu_i$ where n_i is the number of impurity atoms and μ_i the chemical potential of the the ionic reservoir. Complications in the formation energy computation arise from the reference chosen to define the electron energy $E[ne^-]$. A natural choice is to assume that the defect can exchange electrons stored in a reservoir with energy $\mu_e = \epsilon_{TVB} + \epsilon_F$ where ϵ_{TVB} is the top of valence band and ϵ_F the Fermi level of the material [8]. For this reason, it can be computed as $E[ne^-] = -q(\epsilon^q_{TVB} - \epsilon_F)$ with q the defect charge. Nevertheless, equation 2.24 must be read with caution as it has to consider the corrections required for a supercell approach:

1. The value of the top of valence band for each charged state (ϵ^q_{TVB}) must be in the same reference as the one of the perfect crystalline structure. One solution is to compute both values of the charged state and for the crystalline silicon with respect to the vacuum. If only ϵ_{TVB} for the perfect crystal is computed with respect to the vacuum, it is necessary to add the term $\Delta\epsilon_{TVB}$ to equation 2.24, corresponding to a band edge alignment between the band gap edges of the defective and crystalline systems.

2. An electrostatic correction ΔE_{elec} given by equation 2.19, that accounts the undesired image-charge interactions that arise from using periodic boundary conditions.

Therefore, the formation energy is given by

$$\Delta E_{form}[D^q] = E_{TOT}[D^q] - E_{TOT}[Crystal] - \sum_i n_i \mu_i - q(\epsilon_{TVB} - \epsilon_F) + \Delta E_{elec} \tag{2.24}$$

Figure 2.10 shows the dependency of the formation energy E_{form} on the electronic chemical potential μ_e given by equation2.24. We observe in figure 2.10(a) that for μ_{e1}, $\Delta E_{form}[D^+] < \Delta E_{form}[D^0] < \Delta E_{form}[D^-]$, whereas μ_{e2} satisfies $\Delta E_{form}[D^+] > \Delta E_{form}[D^0] > \Delta E_{form}[D^-]$. Therefore, for a given chemical potential μ_{e_i}, a different charge state of the defect will be the most stable one.

This dependency of the formation energy on μ_e demands the proper choice of a reference value for μ_{e_i} to analyze the stability of defects. Figure 2.10(b) shows the formation energy evolution of three different charge states considering the bandgap edges. Here, the ionization levels $\epsilon(+/0)$ and $\epsilon(0/-)$ lie inside the bandgap. Generally, for the computation of the formation energy, the electron energy is referenced to the position of the bandgap edges. The choice of such a reference frame might seem arbitrary, but it is related to the definitions of electron affinity or work function in a semiconductor, defined with respect to the energies to extract or put an electron into a semiconductor in contact with the vacuum.

The **electron affinity** χ is the energy obtained by moving an electron from the vacuum to the bottom of the conduction band (BCB) inside the semiconductor [83]. In an pure semiconductor at absolute zero temperature, an added electron will spontaneously go to the bottom of the conduction band.

$$\chi = E_{vac} - E_{BCB} \tag{2.25}$$

The electron affinity of a surface is closely related to, but distinct from, its work function.

The **work function** is the thermodynamic work that can be obtained by moving an electron from the vacuum to the material. This electron is considered to go to the Fermi level on average, not to the conduction band edge:

$$W = E_{vac} - \epsilon_F \tag{2.26}$$

While the work function of a semiconductor can be changed by doping, the electron affinity ideally does not change with doping and so it is closer to being a material constant. Both properties are shown in figure 2.11.

2.4.4 Band edge positions

In DFT calculations, the top of valence band (TVB) is computed with respect to a mean potential characteristic of the simulated structure [84]. If we consider a structure with a defect, it will have a different reference potential with respect to the perfect crystalline structure, which will cause a shift in the values of the TVB. Consequently, the energy of the TVB (ϵ_{TVB}) must be determined independently of any energy reference. This is possible by the use of the Janak theorem, which allows a calculation of charge transition levels by analyzing the Kohn-Sham eigenvalues of the density-functional theory without the need of explicitly comparing differently charged systems [85, 86]. According to the Janak theorem, the Kohn-Sham eigenvalues of the DFT can be calculated as the derivative of the total energy with respect to the occupation number of the related Kohn-Sham orbital[87] :

$$\epsilon_i = \frac{dE(N)}{dn_i} \tag{2.27}$$

where E is the total energy, ϵ_i is the Kohn-Sham eigenvalue of the ith orbital and n_i its occupation number ($0 < n_i < 1$) so that the total number of electrons becomes $N = \sum_i n_i$. Applying this theorem to the TVB eigenvalue we obtain

$$\epsilon_{TVB} = \frac{dE(N)}{dn_{TVB}} \tag{2.28}$$

where n_{TVB} is the occupation factor of the last occupied band and ϵ_{TVB} is its eigenvalue. By using the derivative definition and considering that with $N-1$ electrons, n_{VBM} goes from 1 to 0, we get:

$$\epsilon_{TVB} = \lim_{N\to\infty} [E_{TOT}(N) - E_{TOT}(N-1)] \tag{2.29}$$

Then according to equation 2.29, the supercell size must be increased until the convergence of ϵ_{TVB}. In our calculations using CRYSTAL17, the ϵ_{TVB} referenced to the vacuum (ionization energy) for a perfect crystalline silicon structure is estimated to be $7.215eV$ with $PBEsol_{12.5}$. The TVB for the same system referenced to the effective potential of the system is reported to be $4.650eV$. Along this work we will not compute the ionization energy for each defective structure, therefore an alignment of the band edges between the perfect crystalline and the defective structures is required.

To estimate the shift of the band structure between the defective supercell and the perfect crystal, the difference between the average electrostatic potentials of the defective supercell $\langle U_D^{eff} \rangle$ and in the crystalline supercell $\langle U_{Cryst}^{eff} \rangle$ must be calculated [88]:

$$\epsilon_{TVB}^{q} = \epsilon_{TVB}^{cryst} + \langle U_D^{eff} \rangle - \langle U_{Cryst}^{eff} \rangle \tag{2.30}$$

where U^{eff} is the effective Kohn–Sham potential and the brackets denote averaging over the bulk and defect supercells, respectively. Then, the magnitude of this correction is $\Delta\epsilon_{TVB} = \langle U_{Cryst}^{eff} \rangle - \langle U_D^{eff} \rangle$. Nevertheless, other potential-energy references are possible. One possibility is to choose

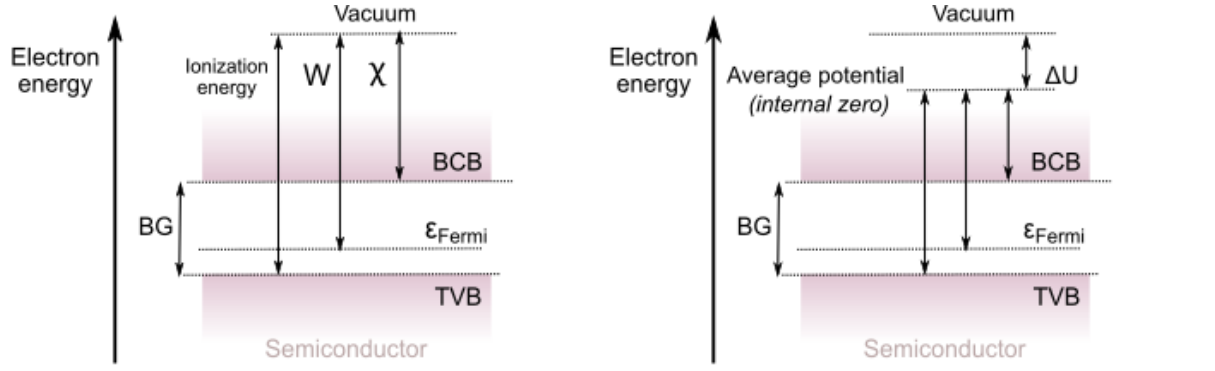

(a) Electron afinity χ, work function W and ionization energy in a semiconductor in contact with vacuum

(b) Top of valance bands (TVB), botom of conduction bands (BCB) and fermi level (ε_{Fermi}) in CRYSTAL17

Figure 2.11: (a) Band diagram of semiconductor-vacuum interface showing electron affinity χ, defined as the difference between near-surface vacuum energy E_{vac}, and near-surface conduction band edge E_C. Also shown: Fermi level E_{Fermi}, top of valence band TVB, work function W. (b)Same band diagram shown the definiton of band gap edges and Fermi level in CRYSTAL17 with respect to an average potential of the crystalline structure.

a deeper core-level energy of the perfect and defective structures. In the case of this work we have chosen to align the values of the gamma point of the last core energy level of both structures

$$\Delta\epsilon_{TVB} = \epsilon^{\Gamma}_{core,Cryst} - \epsilon^{\Gamma}_{core,D^q} \tag{2.31}$$

2.4.5 The marker method

An alternative method to calculate electrical levels of defects is the marker method [80], where one references the system of interest to one that is well understood. If we simplify equation 2.24 we could write

$$\Delta E_{form}[D^q] = E_{TOT}[D^q] - E_{TOT}[Crystal] - \sum_i n_i\mu_i - q(\epsilon^q_{TVB} - \epsilon_F) + \xi[D^q] \tag{2.32}$$

With ϵ^q_{TVB} the valence band maximum with reference to the vacuum of the defective structure and $\xi[D^q]$ the rest of the corrections, that in this case correspond to the electrostatic shift. The ionization level of a defect to go from q to q' is defined as the chemical potential that satisfies $\Delta E_{form}[D^q] = \Delta E_{form}[D^{q'}]$. Using equation 2.32 we find that the acceptor level satisfies

$$\mu_D(-1/0) = E_{TOT}[D^{-1}] - E_{TOT}[D^0] - \epsilon^{-1}_{TVB} + \xi[D^{-1}] - \xi[D^0] \tag{2.33}$$

If we want to reference the acceptor level $\epsilon_D(-/0)$ to a known acceptor level of a *marker* (known) system $\epsilon_M(-/0)$, we would get that

$$\begin{aligned}\epsilon_D(-/0) =& \epsilon_M(-/0) + \left(E_{TOT}[D^{-1}] - E_{TOT}[M^{-1}]\right) - \left(E_{TOT}[D^0] - E_{TOT}[M^0]\right) \\ &- \left(\epsilon_{TVB}[D^{-1}] - \epsilon_{TVB}[M^{-1}]\right) + \left(\left(\xi[D^{-1}] - \xi[M^{-1}]\right) - \left(\xi[D^0] - \xi[M^0]\right)\right)\end{aligned} \tag{2.34}$$

Now, we consider that $E_v(X,q) = E_v(Y,q)$ since we have the calculated formation energy of both systems in the same reference as the crystalline structure, by adding the proper shift $\Delta\epsilon_{TVB}$. Additionally, the correction terms ξ must cancel as they are estimated to fulfill equation 2.19. Then, the unknown acceptor level, $\mu_D(-1/0)$ can be defined with respect to the known marker acceptor level $\mu_M(-1/0)$ and with reference only to total energies that are known:

$$\epsilon_D(-/0) = \epsilon_M(-/0) + \left(E_{TOT}[D^{-1}] - E_{TOT}[M^{-1}]\right) - \left(E_{TOT}[D^0] - E_{TOT}[M^0]\right) \tag{2.35}$$

However, there are two important areas where the marker method may be difficult to apply. The first is where the available markers are far in energy and chemical nature from that of the system of interest, such as using a shallow donor as a reference for a very deep donor. Under these circumstances, it is unlikely to have complete cancellation in the ξ, and hence the error bars in the calculation become more significant. The second is that in some materials there may be no experimental data. In this case, one might use a bulk system as the reference, M , in equations 2.36 and 2.35. Here, the first donor and acceptor levels of a bulk system are ϵ_{TVB} and ϵ_{BCB} (referenced to the vacuum) respectively.

$$\begin{aligned}\epsilon_D(-/0) &= \left(E_{TOT}[D^{-1}] - E_{TOT}[Cryst^{-1}]\right) - \left(E_{TOT}[D^0] - E_{TOT}[Cryst^0]\right) + \epsilon_{BCB}[Cryst] \\ \epsilon_D(0/+) &= \left(E_{TOT}[D^{+1}] - E_{TOT}[Cryst^{+1}]\right) - \left(E_{TOT}[D^0] - E_{TOT}[Cryst^0]\right) + \epsilon_{TVB}[Cryst]\end{aligned} \tag{2.36}$$

Nevertheless, the use of the bulk system as a *marker* translates to ensuring a band alignment in the system and to use the same reference for all the studied systems, which in this work has been chosen to be the vacuum. Therefore, the marker method is already "included" in our correction scheme of formation energies.

2.4.6 Phonon frequency analysis

We have mentioned along this chapter that a numerical optimization of the number of k points and the tolerance parameter is needed for the proper convergence of our DFT results. Then, a geometric optimization with respect to the total energy of the system was performed for each defective structure. Nevertheless, even if the total energy of a structure is minimized, its stability cannot be assured as long as the dynamical stability is not confirmed.

The lattice vibrations of a crystal, also known as **phonon modes**, describe a large number of material properties. In particular, the harmonic phonon spectrum of a solid is the simplest description of its structural dynamics.

To understand the analysis of the phonon frequencies by the harmonic approximation we recall the Born-Oppenheimer approximation, with which the potential energy of the ionic motion $U(\{\mathbf{R}_n\})$ can be written as the sum of the ground state electronic energy ϵ_0 and the ionic interaction V_{NN}:

$$U(\{\mathbf{R}_n\}) = \epsilon_0 + V_{NN} \tag{2.37}$$

We define the position of the n-th atom as $\mathbf{R}_n = \mathbf{R}_0 + u_n$ where u_n is a little displacement with respect to the equilibrium position $\mathbf{R}_0$. In the harmonic approximation the potential energy of the lattice is expanded up to the second order around the minimum energy value. To express such an expansion, we label two different ions n, m and we define vectors $\alpha = (x, y, z), \beta = (x, y, z)$:

$$U = U_0 + \sum_{n,\alpha} \frac{\partial U}{\partial u_{n,\alpha}}\Big|_0 + \frac{1}{2} \sum_{n,m,\alpha,\beta} \frac{\partial^2 U}{\partial u_{n,\alpha} u_{m,\beta}}\Big|_0 u_{n,\alpha} u_{m,\beta} \tag{2.38}$$

As the ions are in equilibrium at a minimum of the total potential U, the first order derivative is equal to zero, while the second-order derivatives correspond to a *Hessian matrix*.

A **Hessian matrix** is a square matrix of second-order partial derivatives of a scalar function. One of the main characteristics of the Hessian is that when all its eigenvalues are positive, then the scalar function is at a stable minimum at point x. If the Hessian has both positive and negative eigenvalues, then x is a saddle point.

In this case, the Hessian matrix $\frac{\partial^2 U}{\partial u_{n,\alpha} u_{m,\beta}}\Big|_0$ is defined as the force-constant matrix and its eigenvalues correspond to the frequencies of the normal modes of vibration for the considered system, i.e. the phonon frequencies.
In this work, we have analyzed the phonon frequencies at the $\Gamma-$ point by computing the vibration of harmonic frequencies. If a value of one of the frequencies turned to be negative, we explored

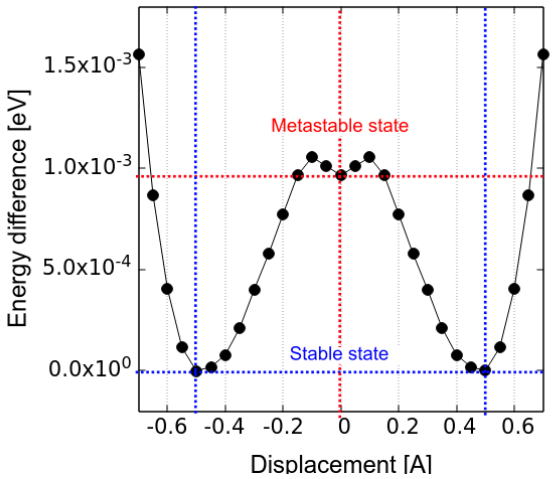

Figure 2.12: Analysis of the normal mode for the case of a supercell with 64 silicon atoms and a H^+ impurity.

the normal mode of the negative frequency in order to find a total energy minimum. If we call $|r_0\rangle$ the *metastable* configuration; then the set of configurations explored is $|r_i\rangle = |r_0\rangle + \delta_i|u\rangle$; $|u\rangle$ is the eigenvector of the negative frequency mode, i an integer and δ a small displacement. The total energy of the system is computed for each configuration. An example of such an analysis is shown in figure 2.12, for the case of a supercell of 64 silicon atoms and an interstitial H^+ defect. A first geometry optimization led to a transition state with an energy that is, indeed, in a local minimum but that does not correspond to the configuration with minimal energy. In figure 2.12 the term *Energy difference* refers to the energy difference of the different configurations along the eigenvector of the negative frequency mode with respect to the minimal energy. We observe that the error in the total energy of the system in the metastable state is around $10^{-3}eV$. This value will vary from one system to another according to the number of atoms and type of defect of the simulated structure.

CHAPTER 3

Hydrogen and self silicon defects induced degradation

There is a global consensus around the fact that hydrogen is the main cause of LeTID [15, 30, 37, 43, 44, 45, 46] along with metallic impurities [30, 37, 46]. The hypothesis of the presence of hydrogen in LeTID is reinforced by the fact that hydrogen, as well as LeTID, have been observed in all silicon materials, from multicrystalline silicon, mono-like crystalline silicon, p- and n-type silicon, Czochralski-grown silicon, to FZ silicon [15], which is not surprising because many growth techniques use hydrogen. Intrinsic defects are also involved in LeTID degradation since silicon materials with very low impurity concentrations also exhibits LeTID [31]. The single vacancy V and self-interstitial Si_i are the two fundamental point defects in bulk silicon, and they are present in any type of silicon material. At present, the role of these nonmetallic impurities in LeTID dynamics has not been clearly elucidated, one of the main reasons being that these isolated impurities are extremely difficult to observe experimentally.
Interstitial hydrogen is a mobile defect in silicon that can easily bind to native defects or other impurities; therefore, it is widely used for passivation purposes. In silicon modules, hydrogen is required to passivate SiN_x dielectric layers and certain bulk defects. During the firing step in module processing, hydrogen disperses across the bulk silicon and it can be stored in many places, including grain boundaries, dislocations, heavily doped regions, or bound to other impurities. At each of these locations, hydrogen is trapped and released under different conditions. Hydrogen can degrade solar cell performance in several ways, either by forming bulk defects that recombine with charge carriers[89], by passivating dopants [90, 91, 92], by increasing the charge carrier recombination on surfaces, or by causing the formation of structural defects by large congregates [15]. Hydrogen (and other impurities) can recombine with charge carriers during different processes. In the framework of LeTID, we analyze the structural and recombination properties of an active bulk defect in three ways:

- Hydrogen-induced recombination (HIR) in which no other elements or species are involved. Here, the interstitial atomic hydrogen acts as a defect and causes recombination.
- Complex formation caused by an interaction of hydrogen with existing silicon or impu-

rity atoms, which forms recombination active defects such as the vacancy-hydrogen [93] or hydrogen-cobalt complexes observed in p-type silicon [94].

- Crystallographic deformations occur when hydrogen atoms become trapped in the crystal lattice. Platelets are formed when hydrogen stacks in several crystallographic parallel planes, which can induce localized charge recombination [95].

In this chapter, we focus on the possibility that hydrogen, silicon vacancies, and self-silicon interstitial atoms cause LeTID. The case of hydrogen-induced recombination is described in Section 3.1. It requires the study of hydrogen as a monoatomic impurity in its three different charge states: H^+, H^0, and H^-, along with the case of hydrogen as a diatomic molecule, which can be found in two forms, as H_2 or as a dissociated molecule H_2^*. The case of hydrogen forming complexes with other impurities is discussed in detail in Chapter 4, where the hypothesis that metal - hydrogen complexes are the cause of LeTID is studied.
Sections 3.4 and 3.5 analyze the single silicon vacancies and interstitial silicon defects. In the same way, to understand the role of the single vacancy V and self-interstitial Si_i in LeTID degradation, their different charge states are considered. Depending on the charge, they can modify the mechanical and electrical properties of the silicon material differently, in addition to favoring charge carrier recombination [96, 97, 98]. Therefore, to develop physical models that can confirm the involvement of V and Si_i in LeTID degradation, it is necessary to determine the physical properties of neutral and charged defects of this type, such as the formation energies, charge transition levels, and band structures.

3.1 Interstitial monoatomic H impurities

Understanding isolated hydrogen in silicon and its reactions with other impurities requires the study of the stability of the different charge states of the defect. It is well known that hydrogen is present in silicon in three states: H^+, H^0, and H^- [49, 63, 99, 100]. The problem of monoatomic hydrogen inside silicon has been studied both experimentally and theoretically. In particular, *ab initio* theoretical studies at the DFT level approach use either the local density approximation or generalized gradient approximation [48, 100]. In this work, we re-examined the properties of monoatomic hydrogen defects using the $PBEsol_{12.5}$ hybrid functional.
According to the literature, the charge states H^+ and H^0 are located at the bond center (BC) position while H^- occupies the tetrahedral position [48, 49, 100, 101]. These were chosen as the initial positions of each charge state prior to relaxation of the lattice and atomic positions. To determine the stability of the interstitial H defects, we analyzed the formation energy of the defects, which, according to equation 2.24, is given by

$$\Delta E_{form}[H^q] = E_{TOT}[Si + H^q] - E_{TOT}[c:Si] - \frac{1}{2}E[H_2] - q(\epsilon^q_{TVB} + \Delta\epsilon^q_{TVB} - \epsilon_F) + \Delta E_{elec} \qquad (3.1)$$

In equation 3.1 the term $E_{TOT}[Si + H^q]$ refers to the total energy of the defective system, $E_{TOT}[c:Si]$ is the total energy of the crystal, ϵ^q_{TVB} is the value of the top of the valence band, $\Delta\epsilon^q_{TVB}$ is the

	H^+		H^0		H^-	
Atoms	ΔE_{TOT} **[eV]**	E_{BG}**[eV]**	ΔE_{TOT} **[eV]**	E_{BG}**[eV]**	ΔE_{TOT} **[eV]**	E_{BG}**[eV]**
8	0.585	0.906	13,72	0.939	6,87	0,8798
32	0.692	0.918	13,83	1.129	6,45	1,1093
64	0.792	0.927	13,80	1.154	6,34	1,0835
128	0,812	0,987	13,80	1,164	6,28	1,0649
216	0,811	0,957	13,83	1,170	6,27	1,1166
512	0.811	0.967	13,83	1,168	6,22	1,0839

Table 3.1: Relative formation energies and band gap values for supercells of different sizes containing interstitial monoatomic hydrogen in three charge states.

correction for the band alignment, and ΔE_{elec} is the electric correction owing to the interaction of charge images. We chose the reference energy for hydrogen as the isolated H_2 molecule and its chemical potential is computed using the functional $PBEsol_{12.5}$. Spin polarized calculations have been performed in the case of H^0.

To reproduce the properties of isolated defects, the convergence of the formation energy and band gap values with respect to the number of atoms in the supercell was analyzed. Table 3.1 lists the formation energy and band gap values obtained for supercells of different sizes. We observe that the formation energies for the three charge states of interstitial hydrogen converges for supercells with 128 atoms, whereas the band gap value only does it for larger cells containing 216 Si atoms. Therefore, the structural and electronic properties of hydrogen impurities were studied using supercells with 216 Si atoms. For supercells of this size, the electrostatic correction is computed as $\Delta E_{elect} = -q^2 \times 0.118eV$, whereas the band alignment is $\Delta\epsilon^-_{TVB} = -0.189$ eV for H^- and $\Delta\epsilon^+_{TVB} = -0.087$ eV for H^+.

Figure 3.1 presents the stable positions of the three interstitial monoatomic defects with respect to their neighboring atoms. H^+ is located at a position that deviates slightly from the bond center (BC), as shown in Fig. 3.1a. The $Si-H$ distance is approximately 1.59Å consequently, the neighboring Si atoms move out over 0.41Å each. In a silicon crystal, the maximum charge occurs at the bond center. Because H^+ seeks regions with the highest electron charge density, it lies at or near the bond center, where the maximum charges occur in silicon. The position of H^+ agrees with the results of [48].

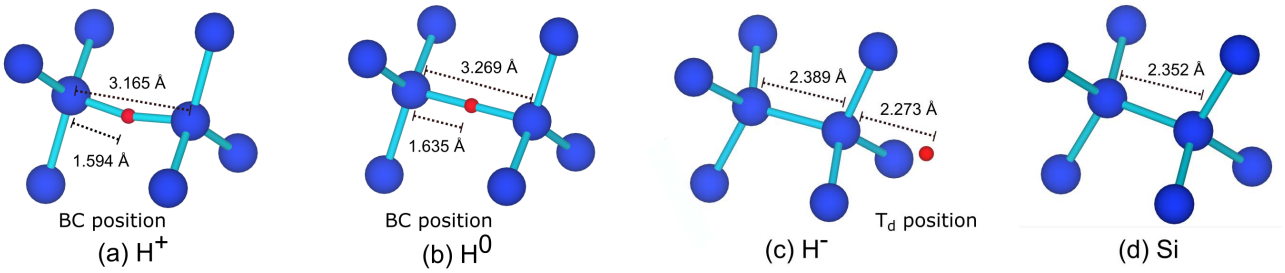

Figure 3.1: Minimum energy atomic configurations of charge states of interstitial hydrogen in bulk Si. Positions obtained from supercells containing 216 Si atoms. Only neighboring hydrogen atoms are shown.

The neutral interstitial hydrogen H^0 is obtained to be at the midway of two silicon atoms (Fig. 3.1b). The Si-H distance is found to be slightly longer than that in the positive charge state, and it is equal to 1.63Å. In this case, the neighboring Si atoms move out over 0.45Å.
In contrast, the negative charge state H^- resides in the vicinity of the lower electron density at the tetrahedral interstitial site (T_d) (Fig. 3.1c). The relaxations of the neighboring silicon atoms are of the order of 0.05Å, which is negligible for this configuration.
In Figure 3.2 we present the evolution of the formation energy as a function of the chemical potential for the three charge states of hydrogen. The chemical potential is referenced to the top of the valence band. We define the thermodynamic transition level $\epsilon(q_1/q_2)$ as the chemical potential, for which the formation energies of the charge states q_1 and q_2 are equal:

$$\epsilon(q_1/q_2) = \frac{E_{form}[D^{q_1};\epsilon_F = 0] - E_{form}[D^{q_2};\mu_e = 0]}{q_2 - q_1} \tag{3.2}$$

The transition levels will determine the stability of the defects with respect to the chemical potential. As shown in Figure 3.2, the donor level $\epsilon(0/+)$ is defined as the chemical potential position at which H^+ and H^0 have equal formation energies and implies that, when the chemical potential is below $\epsilon(0/+)$, H^+ is stable. Likewise, the acceptor level $\epsilon(-/0)$ is defined as the chemical potential position at which H^0 and H^- formation energies agree. This means that when the chemical potential is above $\epsilon(-/0)$, H^- is stable. The donor and acceptor levels are located at 0.28 and 0.83 eV, respectively. The fact that $\epsilon(0/+) > \epsilon(-/0)$ indicates that the neutral charge state H^0 is never thermodynamically stable. The chemical potential range in which the H^+ is the most stable charge state is below $\epsilon(-/+)$, located at 0.55 eV. If the chemical potential is above 0.55 eV, the negative charge state will be the most stable one. Therefore, the transition level between $\epsilon(-/+)$ describes the electronic behavior of the impurity. Our results are in good agreement with experimental results [102] that have established that the donor level is positioned above $\epsilon_m + 0.3$ eV and that the acceptor level is below $\epsilon_m - 0.25$ eV, where ϵ_m is defined as the middle of the bandgap.

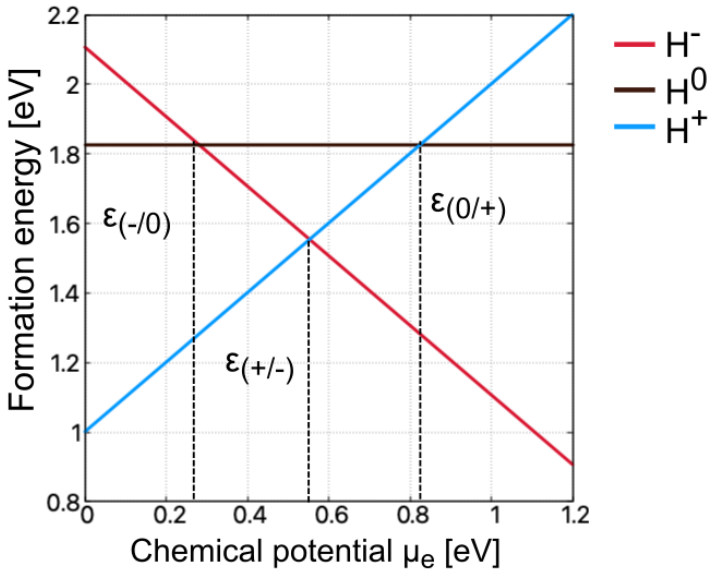

Figure 3.2: Relative formation energies for H charge states as a function of the chemical potential μ.The acceptor and donor levels are indicated as E_A and E_D, respectively for a converged supercell with 216 atoms.

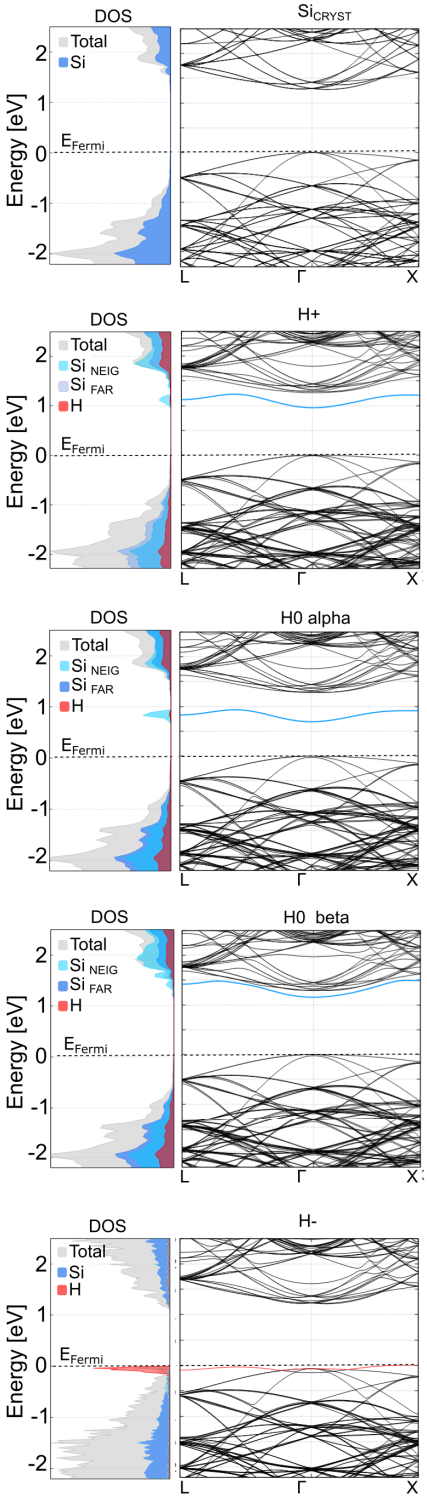

Figure 3.3: Band structure of crystalline silicon and defective structures containing H^-, H^0 and H_+.

From this behavior we see that p-doped (Fermi level at the top of the valence band) and n-doped materials (Fermi level at the bottom of the conduction band) will favor the presence of H^- and H^+ defects, respectively.

3.1.1 Electronic properties

Figure 3.3 presents a comparison of the band structures of crystalline silicon and defective structures containing three charge states of interstitial monoatomic hydrogen. These structures were obtained for supercells with 216 silicon atoms.

The positive charge state H^+ introduces a level at the top of the bandgap, which is induced by the antibonding combination of the Si hybrid orbitals derived from the displacement of the neighboring silicon atoms. This is highlighted in the band diagram, with the blue line representing the induced energy level. Considering the density of states (DOS), this state belongs to the neighboring silicon atom. This implies that H^+ forms a complex with the neighboring silicon, where an electron is removed from the combination of Si orbitals. From the position of the Fermi energy that defines the last occupied energy state, we observe that the level introduced by H^+ is empty.

For the neutral charge state, we considered a total spin of $S = 1$ in our calculations, which is attributed to the unpaired electron of the hydrogen impurity. In figure 3.3, we present two band diagrams of the H^0 defect for the alpha and beta electrons, respectively. The $H^0[\alpha]$ diagram shows an energy level in the middle of the bandgap. As in the case of H^+, the induced energy level in the band gap is empty and belongs to a neighboring silicon atom. This energy level is also induced by the anti-bonding of the Si hybrid orbitals produced by the movement of the neighboring silicon atoms, as highlighted in blue.

We observe as well that the presence of H^- introduces a deep level in the bandgap near the top of the valence band. This defect is unlikely to induce carrier recombination on its own because the energy level that it induces is at the top of the valence band.

3.1.2 Influence of the correction scheme and Hamiltonian on defect stability

The results of our calculations regarding the formation energy and ionization level values can be affected by two main factors: the choice of Hamiltonian and the correction scheme considered in this work (which is explained in details in sections 2.4.2, 2.4.4). To estimate the error caused by

the choice of the Hamiltonian, we compared the formation energies obtained for the three charge states of hydrogen using the $PBEsol$ functional (no HF percentage) with respect to the results obtained using a hybrid functional. A comparison is shown in Figure 3.4.
The curve of the formation energy as a function of the Fermi level for each Hamiltonian reported in this study is represented by a straight line for each defect. The dotted lines correspond to three different scenarios of the correction scheme considered in this study:

- The valence band alignment $\Delta\epsilon_{TVB}$ is not considered
- The electrostatic correction E_{elec} is not considered
- Neither of the two precedent corrections is considered

In the case of $PBEsol$, the band alignment is $\Delta\epsilon^{-}_{TVB} = -0.171$ eV for H^{-} and $\Delta\epsilon^{+}_{TVB} = -0.083$ eV for H^{+}, values that are similar to those of $PBEsol_{12.5}$. On the other hand, E_{elec} is computed according to equation 2.19, and depends on the lattice parameter. The electrostatic correction has a value of $\Delta E_{elect} = -q^2 \times 0.118eV$ the same that is computed for $PBEsol_{12.5}$ because the lattice parameter of a supercell with 216 Si atoms is the same in both cases ($L \sim 16.3$Å). The effect of considering our correction scheme can lead to a shift in the transition levels up to $0.22eV$ in the case of $PBEsol$. The $PBEsol_{12.5}$ calculations present a shift of the order of $0.15eV$ for $\Delta\epsilon_{TVB}$, similar to that of the electrostatic correction. The correction required for the band alignment depends on the sign of the defect charge; in the case of H^{-}, both corrections have the same sign and they add, leading to a dispersion of the donor level of $\approx 0.25eV$. In the case of the positive charge state, the shift in the formation energy coming form the electrostatic correction is similar to that coming from the band alignment. When all corrections are taken into account, there is an energy difference of $0.3eV$ in the donor level compared to the case when no corrections are considered.
In the case of $PBEsol_{12.5}$, the impact of the corrections scheme is similar. The position of donnor and acceptor levels can vary within a range of $0.2eV$ for $\epsilon(-/0)$ and up to $0.25eV$ for $\epsilon(0/+)$. The

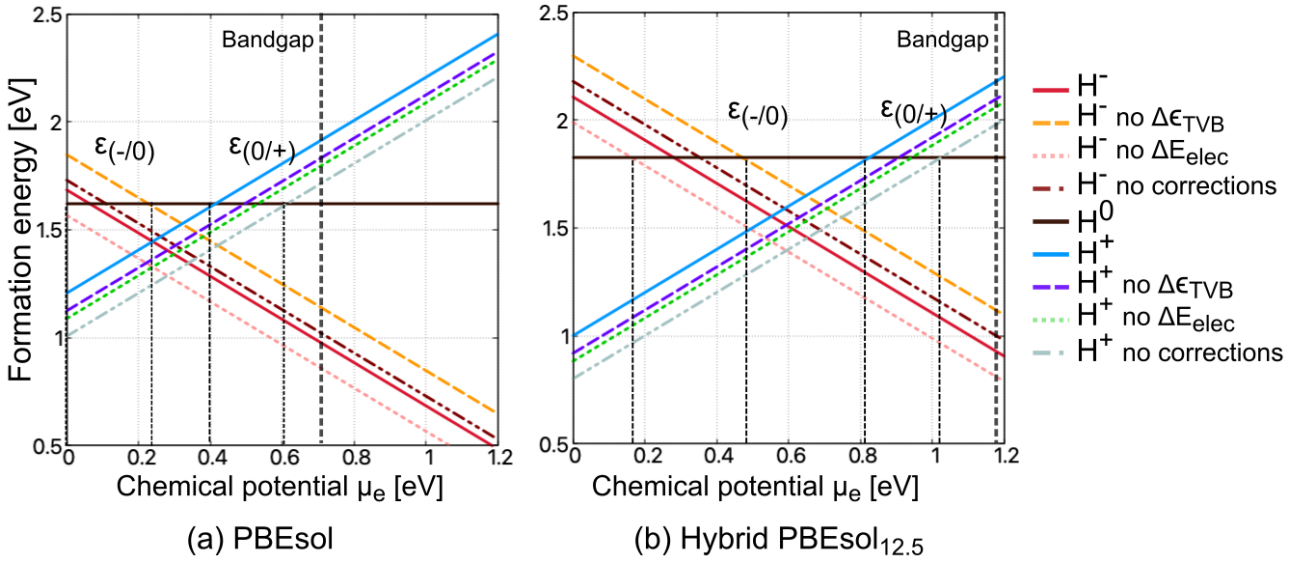

Figure 3.4: Relative formation energies for H charge states as a function of the chemical potential μ. (a) Comparison between the formation energy values obtained considering the corrections $\Delta\epsilon_{TVB}$ and ΔE_{elect} and without taking them into account for $PBEsol$.(b) Idem for $PBEsol_{12.5}$

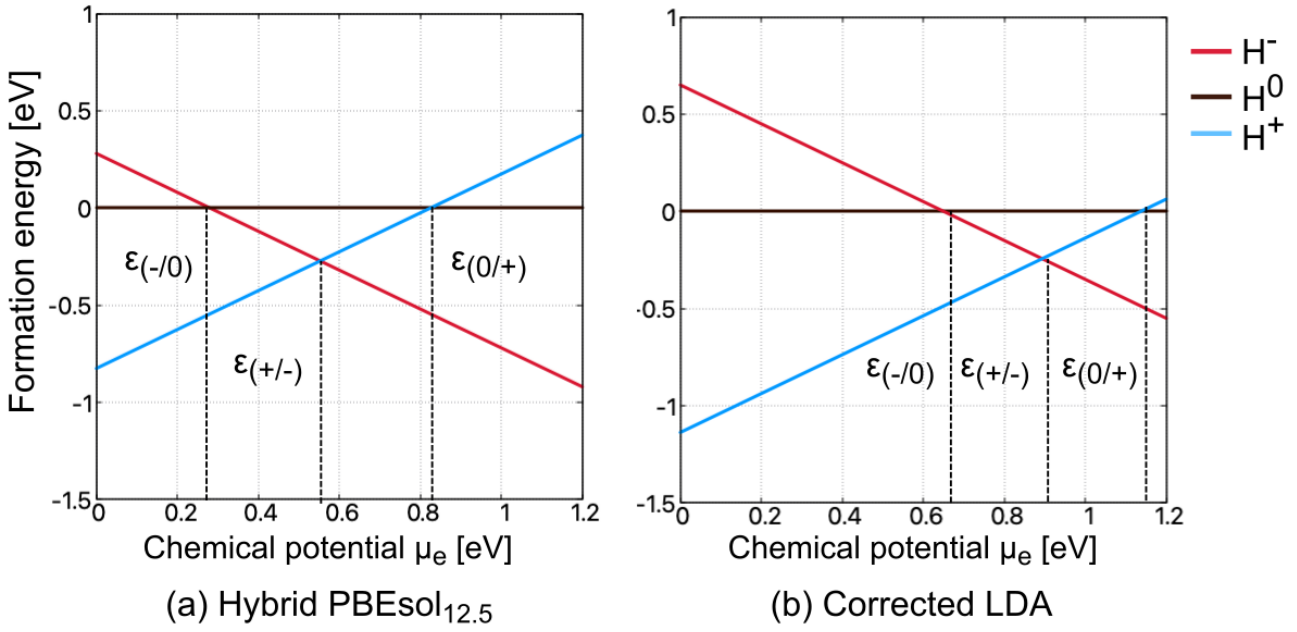

Figure 3.5: Comparison between our results and previous first principles studies [48, 49] for relative formation energies for H charge states as a function of the chemical potential μ.

precision of the transition energy level position is important for relating the stable charge state of hydrogen with a specific electronic density (or doping concentration) in silicon materials. Regardless the differences in the influence of our corrections scheme all simulations considering $PBEsol$ or $PBEsol_{12.5}$ Hamiltonians, with or without our correction scheme, describe the same general behavior of hydrogen-charged defects, where the neutral hydrogen H^0 is never the most stable charge state.

Previous first-principles studies have investigated interstitial hydrogen defects. One of the most cited articles is Ref. [49] whose results are in perfect agreement with those of [48], in which an LDA Hamiltonian was used to obtain the relative formation energies for different hydrogen-charge states as a function of the Fermi-level position. An *a posteriori correction* was applied to the LDA results to bring the band gap to agreement with the experimental value. Such a correction consists of a rigid shift in the defect level together with the conduction bands. The same methodology is used in [49]. Figure 3.5 presents a comparison between our results and those presented in these studies [48, 49]. The relative formation energies were referenced to the formation energy of H^0 for a better comparison. We observe that the relative positions of the transition levels are shifted to higher Fermi levels in the corrected LDA results compared to ours. The energy difference between $\epsilon(-/0)$ and $\epsilon(0/+)$ is 0.4 eV for the corrected LDA scheme, while we obtain $0.6eV$. These differences are explained by the dicrepancies in the corrections used in [48, 49] and in our work.

Even though Ref. [48] claims that this correction procedure is practical in avoiding computationally intensive approaches and overcoming the LDA bandgap problem, it results in a correction scheme that requires knowledge of an experimental value (i.e., the bandgap) and shifts almost arbitrarily the formation energy values, making it unreliable. On the other hand, our correction methodology is entirely self-reliable as it does not rely on any experimental value and pragmatically avoids the bandgap error that arises from using a DFT approach, by utilizing a hybrid Hamiltonian.

3.2 Interstitial H_2 in silicon

Theory and experiment have confirmed the presence of two stable forms of diatomic hydrogen in crystalline silicon [49, 101]: H_2 as a bounded pair molecule in the tetrahedral interstitial site (T_d), presented in Fig. 3.6(a), and, H_2^* complex consisting in one hydrogen atom in a bond-center-like position and the other in an antibonding-type position (see Fig.3.6(b)). To simulate the diatomic impurities, the H_2 molecule was initially located at a tetrahedral interstitial site oriented along the [100] direction. For the simulation of H_2^*, in the initial structure, one hydrogen atom was located in a BC position and the other in a T_d position around the same Si atom. In both cases, the positions of the host atoms were relaxed until the energy of the system was minimized. No spin was considered for any of configuration.
The formation energy for these interstitial molecules is computed as

$$\Delta E_{form}[H_2] = E_{TOT}[Si + H_2] - E_{TOT}[Si] - E_{H_2} \tag{3.3}$$

where $E_{TOT}[Si + H_2]$ refers to the total energy of the defective system and $E_{TOT}Si$ is the energy of the crystalline bulk silicon. As in Section 3.1, the reference energy for the hydrogen molecule was chosen to be the energy of the isolated H_2. The convergences of the formation energy and bandgap values of the defective structures containing H_2 and H_2^* are presented in Table 3.2. The formation energies and band gap values converged for supercells containing 216 Si atoms, for which the structural and electronic properties were computed.
We found that the H_2 molecule is most stable at a tetrahedral interstitial site and respects the orientation along the [100] axis (see Figure 3.6(b)). Our calculations produce a bond length of 0.784Å, which is slightly longer than the experimental bond length in free space reported to be 0.74Å [100]. The change in the positions of the nearest Si neighbors is negligible. The formation energy of this configuration is $1.08eV$.
Regarding H_2^*, it has been previously proposed that relaxation of the Si atom between the two H from its equilibrium site breaks the original Si-Si bond. The hydrogen in the BC position then binds to this dangling bond. [100]. According to our calculations, this configuration has a formation energy of $1.394eV$. We observe that the position of the hydrogen in the BC is not symmetrical, as it is closer to one of the two nearest silicon atoms. Nevertheless, the distance between each

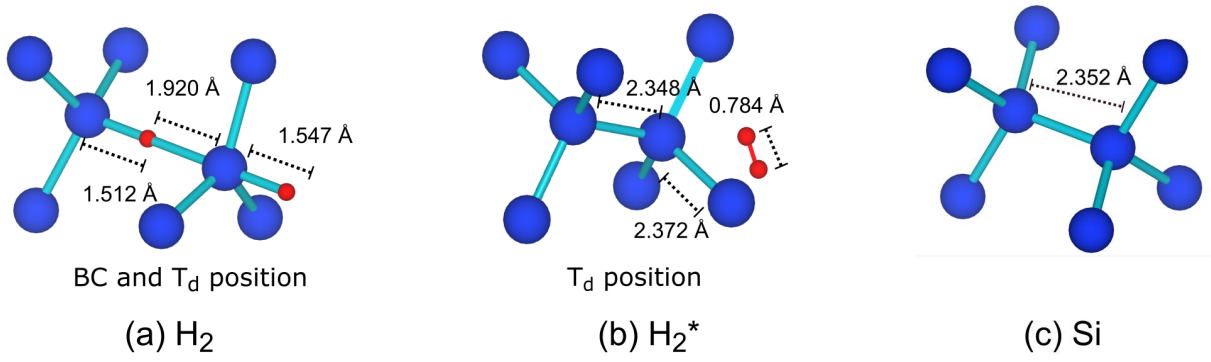

Figure 3.6: Generated position of interstitial H_2 and H_2^*.

Atoms	H_2		H_2^*	
Atoms	E_{form} **[eV]**	E_{BG}**[eV]**	E_{form} **[eV]**	E_{BG}**[eV]**
8	1.1046	1.209	1.404	1.218
32	1.0796	1.269	1.363	1.285
64	1.0850	1.194	1.405	1.200
128	1.0867	1.193	1.421	1.200
216	1.081	1.180	1.394	1,182
532	1.082	1.186	1.400	1,193

Table 3.2: Relative formation energies and bandgaps for interstitial H_2 and H_2^*.

hydrogen atom and its nearest silicon neighbor was found to be roughly the same(Fig. 3.6(a)).

The H_2^* complex has a slightly higher energy than H_2 and it has been observed that its activation barrier for migration is lower than that of molecular hydrogen [101]. This suggests that H_2^* has an important role in diffusion. If this is the case, this type of hydrogen defect might have a greater impact in LeTID than H_2.

3.2.1 Electronic properties of hydrogen molecules

We observe from figure 3.7 that both H_2^* and H_2 defects barely affect the silicon band structure. The band gap values obtained for H_2^* and H_2 are respetively 1.182 and $1.180eV$. The difference between the bandgap values of both defective structures with respect to crystalline silicon ($1.17eV$)is within the numerical error and they do not induce any energy level in the band gap. Therefore, they do not have any charge recombination behavior.

For H_2^*, the density of states of silicon between the two hydrogen atoms remains the same as any other silicon atom in the crystal. This suggests that even if the movement of this silicon atom to its relaxed position is important, it does not induce an antibonding combination of the Si hybrid orbitals. This is because it has two hydrogen atoms as nearest neighbors. Also, no difference is observed between H_{BC} (BC position) and H_{T_d} (T_d position)regarding their electronic properties.

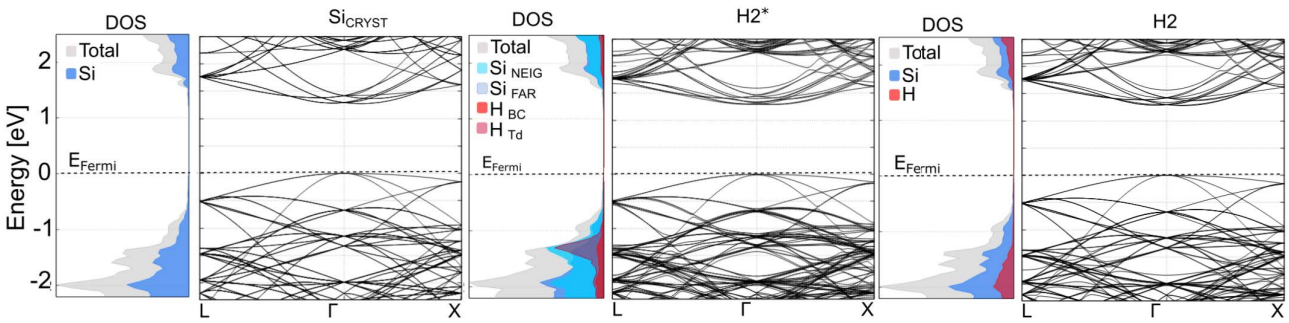

Figure 3.7: Band structure of crystalline silicon and defective structures containing H_2 and H_2^* interstitial molecules.

3.3 Hydrogen induced recombination

The possibility that hydrogen might cause recombination on its own was analyzed by considering the formation energies of the different charge states, transition levels, and band diagrams obtained from our calculations. These results indicate that only H^+ and H^0 will be recombination-active defects, whereas H^-, H_2 and H_2^* will not trap any charge carriers in any significant manner.

An additional analysis of the optoelectronic properties of the defective structures was performed to corroborate the meta-stability of the impurities. It has been observed that hydrogenated amorphous silicon undergoes light-induced degradation, and that this process is reversible upon annealing [103], as it occurs for LeTID. This degradation is explained by the Staebler-Woronski effect, where the metastability of hydrogen with dangling bonds causes a 0.3% increase in the refractive index of the structure measured experimentally [103]. Taking this into account and that for isotropic materials the dielectric constant ϵ and the refractive index n of a crystalline material are related by $n = \sqrt{\epsilon}$, we computed the dielectric constant of the defective structures. The dielectric constant measures the ability of a material to store electric charge. In a semiconductor, the dielectric constant influences the strength of the Coulomb interaction between electrons and holes, which can modify the effective mass of these particles and influence the bandgap energy. We define ΔE_Γ defined as energy difference at the Γ-point between the Fermi level and the first unoccupied energy level. This variable results convenient to analyze the change of the dielectric constant of each structure. Indeed, an increase in the dielectric constant can be related to the existence of energy levels in the band gap. The lower the value of ΔE_Γ, the higher the probability of recombination, resulting in an increase in the dielectric constant.

The changes in the dielectric constant and ΔE_Γ of structures containing hydrogen impurities, in comparison to the values calculated with $PBEsol_{12.5}$ for a perfect crystalline structure, are presented in Table 3.3. We observe that only the cases of H^+ and H^0 present an important change in the dielectric constant. Structures with direct band gaps facilitate charge recombination more than structures with indirect band gaps. This result, along with the decrease in the ΔE_Γ value for H^0 and H^+, reinforces the hypothesis that these two defects behave as charge recombination centers.

On the other side, the relative stability analysis showed that the donor energy level $\epsilon(-/0)$ of hydrogen is higher than the acceptor energy level $\epsilon(0/+)$ (Fig. 3.2), which implies that the neutral

Defect	**Dielectric constant ϵ**	$\Delta_{\epsilon\%}$	ΔE_Γ **[eV]**	**Band gap**
H^+	10,986	2,077	0.957	Direct
H^0	10,986	2,077	1.154	Direct
H^-	10,788	0,237	1.117	Indirect
H_2	10,794	0,301	1.180	Indirect
H_2^*	10,777	0,136	1.182	Indirect
Crystal	10,762	0	1.17	Indirect

Table 3.3: Dielectric constant, percentage difference with respect to crystalline silicon and band gap values for different hydrogen defects as we calculated with $PBEsol_{12.5}$.

state H^0 is never the most stable on for hydrogen. As a result, a neutrally charged hydrogen atom will seek to reduce its energy by giving or accepting electrons; it will form $H-$ or $H+$ according to the position of the chemical potential.
The position of the chemical potential can be modified by doping the silicon material; therefore, the presence of one of the charge states is favored: H^+ for p-type materials and H^- for n-type Si. When E_{Fermi} is exactly at $\epsilon(+/-)$, the probability of forming H^+ or H^- is the same.
Nevertheless, in both intrinsic and doped silicon, H^0 exists at very low concentrations, and the equilibrium condition of bulk materials (where the total amount of hydrogen and electrons is conserved) requires that the fractional concentration of hydrogen be maintained [49]. Therefore, after a neutral hydrogen defect has given or accepted an electron to form the appropriate charge state, $H-$ or $H+$ must form another H^0, and so on.This dynamic can be written as

$$\begin{aligned} H^- + hole &\rightarrow H^0 \\ H^0 + e^- &\rightarrow H^- \end{aligned} \tag{3.4}$$

To maintain fractional hydrogen concentrations, according to equation 3.4, H^0 and H^- are formed by capturing an electron or a hole, respectively. The loss of holes and electron causing recombination leads to hydrogen-induced recombination (HIR), as proposed in [15].
In addition to HIR, hydrogen can passivate doping defects in silicon[100]. For example, in the case of p-type silicon, the most stable charge state of hydrogen is H^+, which exhibits donor-like behavior. Here, electrons from neutral hydrogen annihilate free holes in the valence band, leading to passivation of the p-type material [48, 101]. To illustrate this case, we consider boron-doped silicon: the high mobility of H^+ and the Coulombic attraction to negatively charged B atoms lead to the formation of HB pairs: $H^+ + B^- \rightarrow (HB)$. Pair formation occurs because of passivation of the doped material [48].
Considering that hydrogen can modify the doping properties of silicon materials [101], at high H concentrations, it modifies the chemical potential such that it reaches the transition $\epsilon(-/+)$. Here, any additional H^0 would have an equal probability of forming H^+ or H^-, leaving the Fermi level unchanged. This behavior has been experimentally observed [101] and enhances the HIR.
The fact that both H_2 and H_2^* molecules have lower formation energies within the Si crystal than H^0 means that they are more stable than the monoatomic defects. The energy difference between the neutral charge state H^0 and H_2 and H_2^* found in our results is in agreement with the energy differences obtained by Ref. [100]. The ability of H_2 and H_2^* to dissociate remains to be studied by determining the bounding energy of these molecules. Their dissociation would increase the amount of monatomic hydrogen and contribute to the hydrogen-induced recombination dynamics.

3.4 The single vacancy

Single vacancies are one of the most common self-silicon defects. It has been observed experimentally and, along with ab initio calculations, it has been proven to exist as a stable defect in

crystalline silicon in different charge states: V^{++}, V^{+}, V^{0} and V^{-} [104]. The most stable geometries of the neutral and charge states of the silicon vacancy are $V^0 \rightarrow D_{2d}$, $V^{++} \rightarrow T_d$, $V^{+} \rightarrow D_{2d}$, and $V^{-} \rightarrow D_{3d}$ [105, 106], they are schematized in Figure 3.10. To study these configurations, one silicon atom was removed from the perfect crystalline structure to set the initial structures. The removal of a Si atom leaves four unpaired electrons. The charge states of the mono-vacancy are formed by the addition or removal of one or more electrons. Relaxation of the host atoms around the impurity was performed.

The formation energy for the simple silicon vacancy is computed following the equation

$$E_{form}[V^q] = E_{TOT}[Si, V^q] - \frac{N-1}{N} E_{TOT}[Crystal] - q(\epsilon_{TVB} - \epsilon_F) + \Delta E_{elec} \tag{3.5}$$

where $E_{form}[V^q]$ is the formation energy of the vacancy, $E_{TOT}[Si, V^q]$ is the total energy of the system with a vacancy, and $E_{TOT}[Crystal]$ is the energy of the perfect crystalline structure. The factor $\frac{N-1}{N}$ originates from the removal of one Si atom from the crystal. The convergence of the formation energy with respect to the supercell size was checked in the same manner as for hydrogen. Convergence of the formation energy and bandgap values is presented in figure 3.4, it was obtained for supercells containing 215 Si atoms.

For all defective structures, computations were performed with and without considering spin. The imposition of a spin is of great importance because it induces a symmetry break in the system. With CRYSTAL, the spin of the system is determined by stating the difference between the alpha and beta electrons ($S = n_\alpha - n_\beta$). The total energies were compared to determine the most stable spin configuration for each charge state. The most stable configurations for the structures V^{++} and V^0 were obtained with closed shell calculations, which indicates the recombination of the electrons within the crystal. In the cases of V^+ and V^- the most stable charge state is found to have a spin of $S = 1$.

Atoms	7	31	63	127	217	531
E_{form} **[eV]**	3.805	3.912	3.947	3.895	3.947	3.939
E_{BG} **[eV]**	0.7062	0.7149	0.7203	0.7383	0.7573	0.7568

Table 3.4: Relative formation energies and band gap values for supercells of different sizes containing a neutral single Si-vacancy.

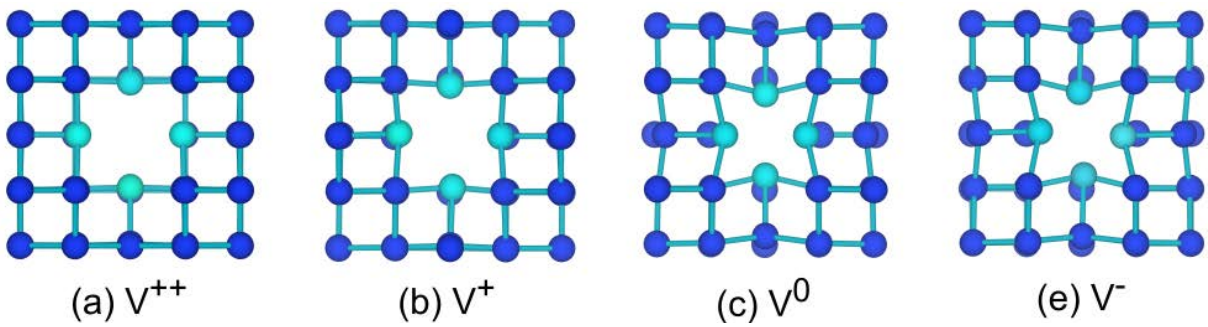

Figure 3.8: Position of silicon atoms for different charge states of the single vacancy. View from plane [110].

Charge state	Point group	Distance [Å]	Multiplicity
V^{++}	T_d	3.616	6
V^{+}	D_{2d}	3.488	4
		3.310	2
V^{0}	D_{2d}	3.461	4
		2.858	2
V^{-}	C_{2v}	3.273	4
		2.925	1
		2.631	1

Table 3.5: Distances between the four atoms surrounding the vacancy for supercells of 215 Si atoms.

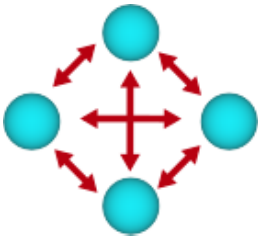

Figure 3.9: The multiplicity refers to the 6 different distances that can be traced among the 4 neighboring Si atoms.

Figure 3.8 shows the position of the Si atoms nearest to the vacancy from the viewpoint of the plane [110]. For the positively charged states of the vacancy, the positions of the host atoms did not vary significantly. Nevertheless, for the cases of V^0 and V^-, relaxation of the host atoms is important. The distances between the four atoms surrounding the vacancy are listed in table 3.5. From these results, we can conclude that the point groups of the relaxed structures are T_d for V^{++}, D_{2d} for V^+ and V^0, and C_{2v} for V^-. In the T_d, C_{2v}, and D_{2d} structures, the four atoms surrounding the vacancy remained relatively near their bulk sites. Experimental information regarding the V^+ and V^- structures was obtained from electron paramagnetic resonance (EPR) data obtained under illumination [107]. These studies found D_{2d} symmetry for V^+ and C_{2v} symmetry for V^-. No experimental information is available regarding the geometry of other charge states [106].

3.4.1 The Jahn-Teller model for the silicon vacancy

The relaxed positions of the atoms surrounding the vacancy site are explained by the Jahn–Teller effect. This effect allows an energy minimization of the system by removing the degeneracy of the electronic levels of the unpaired electrons [108]. In the linear combination of atomic orbitals

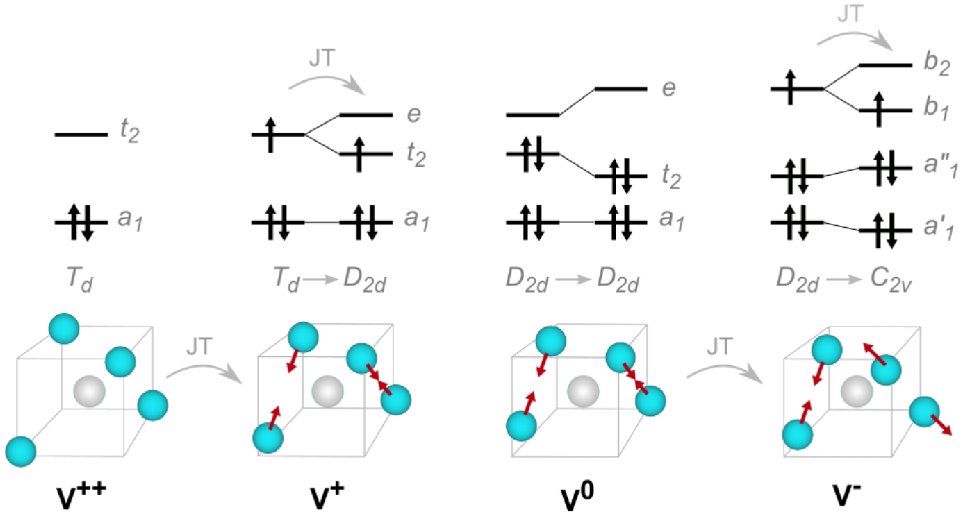

Figure 3.10: Splitting states for a vacancy in Si, the electronic population is denoted with arrows (alpha and beta/ spin up and down). The point symmetry group is specified.

(LCAO) model, each unpaired electron occupies an orbital in the atoms surrounding the vacancy, which induces electronic states in the gap [109].

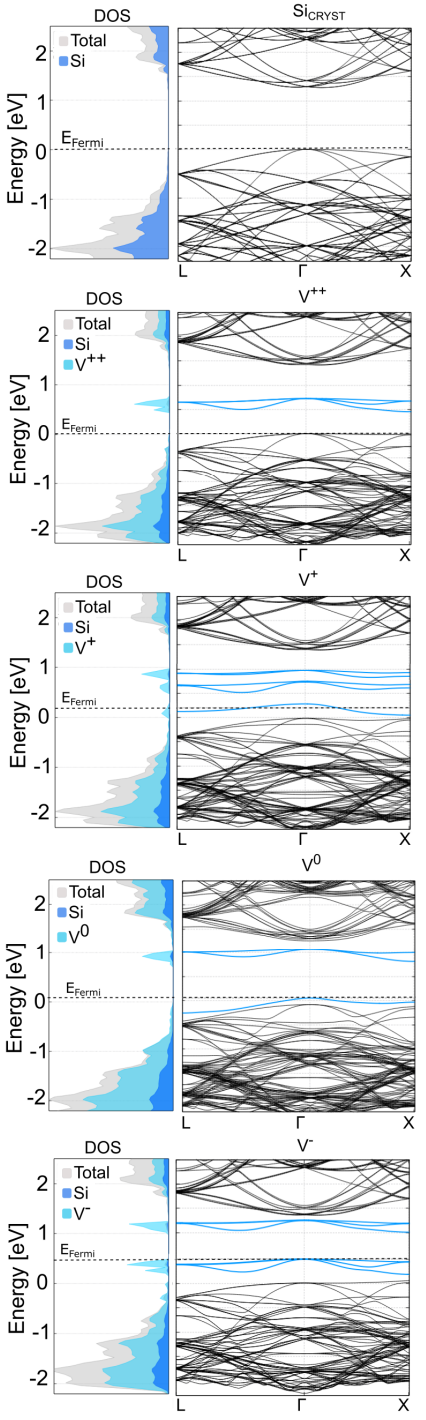

Figure 3.11: Band structure of crystalline silicon and defective structures containing different charge states of the single vacancy.

According to the model proposed by Watkins [110], the electronic configuration of a neutral vacancy in Si with an initial T_d symmetry consists of two electrons at the level a_1^2 and two others in t_1^2, analogous to the electronic configuration of the silicon atom ($[Ne]3s^2 2p^2$). Level a_1 lies in the valence band and is full, as it can contain up to two electrons. The energy level t_1, originally in the valence band, moves into the gap after the removal of the silicon atom from the lattice. This level contains up to six electrons [109]. The relaxation of the atoms surrounding the vacancy is associated with the filling of the gap states, which increases the Fermi level of the structure. When an additional electron in the system populates an empty level, it splits, leading to a symmetry change in the structure.

The Jahn-Teller effect, including the energy-level splitting and distortions of the charge states of the vacancy, is schematically presented in Figure 3.10. To explain how this works, we start with a structure in which the T_d symmetry of the ideal vacancy is maintained. This is the case when no electrons are present at levels a_1 and t_1. If we consider the charge state V^{++}, a_1 is occupied by two electrons and lies below the bandgap. Figure 3.11 shows that the Fermi energy (last occupied state) was zero. The relaxed positions of the host atoms respect a T_d geometry. When one electron is added, we obtain a V^+ structure. As shown in Figure 3.10, the degeneracy of level t_2 splits and symmetry breaks after atomic relaxation, both of which are induced by the Jahn-Teller effect. This atomic relaxation is in the form of tetragonal distortions, giving rise to a D_{2d} symmetry. The t_2 state is populated and increases the Fermi energy to $E_F = 0.19$ eV. In order to obtain a neutral vacancy, another electron must be added to the structure. The t_2 and e levels move further aside, lowering the Fermi energy of V^0 to 0.05 eV. The atoms surrounding the vacancy move closer, respecting the D_{2d} geometry of the system. In order for the symmetry to change again, another electron must be added to the system. The geometry of V^- changes from D_{2d} to C_{2v} and the population of state b_1 increases the Fermi energy to 0.45 eV, as shown in Figure 3.11.

3.4.2 Formation energy and transition level analysis

The relative stability of the different charge states of the vacancy was evaluated by analyzing their formation energies as a function of the chemical potential, which is defined as the energy at which

defects exchange electrons with such reservoirs. The formation energies were computed according to equation 3.5, for which the band alignment was $\Delta\epsilon^{-}_{TVB} = -0.218$ eV for V^{-}, $\Delta\epsilon^{+}_{TVB} = 0.136$ eV for V^{+} and $\Delta\epsilon^{++}_{TVB} = 0.193$ eV for V^{++}. The electrostatic correction, which depends on the size of the supercells considered, has the same value as that considered for charge hydrogen defects ($\Delta E_{elect} = -q^2 \times 0.118eV$). Therefore, the formation energies in electron volts (eV) for a chemical potential equal to zero obtained for the different charge states were: $E_{form}[V^{-}] = 4.438$ eV, $E_{form}[V^{0}] = 3.947$ eV, $E_{form}[V^{+}] = 4.003$ eV, and $E_{form}[V^{++}] = 3.795$ eV.

In Figure 3.12, the relative formation energies for the different charge states of the vacancy are presented; the chemical potential is referenced to the top of the valence band. The transition levels that better describe the electronic behavior of the impurity and define the chemical potential range in which each charge state is stable are $\epsilon(2+/0) = 0.08$ and $\epsilon(0/-) = 0.59$ eV. For materials with a Fermi level below $\epsilon(2+/0)$, the most stable charge state will be V^{++}; V^{-} will be the most likely charge vacancy when the chemical potential is higher than $\epsilon(0/-)$, and between these two values, the stability of the neutral charge state will be predominant. The transition level $\epsilon(+/0)$ is found to be positioned 0.05 eV below the top of the valence band, while $\epsilon(2+/+)$ is 0.21 eV above the TVB.

A comparison of the experimental values of the transition levels with our results is presented in table 3.6. We can see that the transition levels are approximately ±0.1 eV away from the experimental values. Even if we find an acceptable agreement with the experimental results, we consider that it

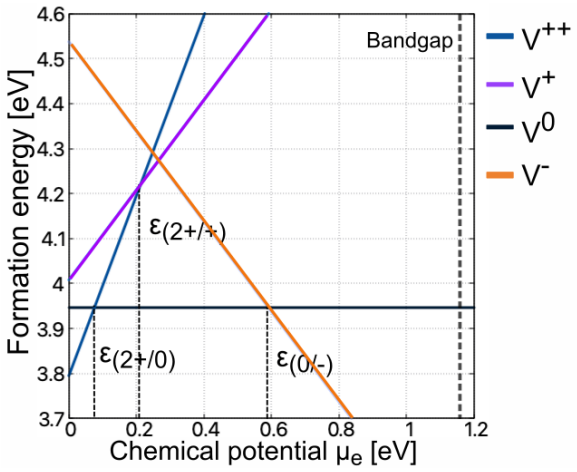

Figure 3.12: Relative formation energies for the single-vacancy charge states as function of the chemical potential.The transition levels are indicated.

Transition level	Exp. [110]	$PBEsol_{12.5}$ [eV]	**LDA** [eV] [106]	**GGA** [eV] [106]	**AMIRO** [eV] [111]	**VASP-VUS** [eV] [111]
$\epsilon(2+/0)$	0.09	0.08	0.192	0.093	0.0	0.06
$\epsilon(2+/+)$	0.13	0.21	0.130	0.130	0.05	0.11
$\epsilon(+/0)$	0.05	-0.050	0.237	0.060	-0.04	0.02
$\epsilon(0/-)$	——	0.59	0.845	0.714	ϵ_{BCB} - 0.31	ϵ_{BCB} - 0.34

Table 3.6: Transition levels obtained in our calculations ($PBEsol_{12.5}$) compared with experimental results and different *ab initio* studies. In all the cases, ϵ_{TVB} was referenced to 0.

is still necessary to study the impact of our correction scheme in the calculated formation energies and transition levels.

Figure 3.13 shows the influence of our correction scheme in the stability behavior of the charge defects. We indicate only the ionization levels that are going to determine the transitions between the most stable states. Only in the case where the band alignment is not considered, there is one transition likely to happen from $V^0 \rightarrow V^-$. In the rest of the cases, the states V^{++}, V^0 and V^- are the most stable configurations. The double donor V^{++} transition to V^0 appears to happen in a range between 0.08 eV and 0.3 eV, while the transition level $\epsilon(0/-)$ varies in a range of 0.18 eV. The ranges in which these transition levels vary are similar to those obtained for the H defect.

Our results are compared to those obtained in Ref. [106] for LDA and GGA studies on the single silicon vacancy (Figure 3.14). This comparison do not allow us to determine the influence of the Hamiltonian on the stability of the defects, because the correction scheme used in [106] differs from ours. In Ref. [106], the marker method was used to obtain the band alignment correction; in particular, $\Delta\epsilon_{TVB}$ was estimated with respect to the transition level $\epsilon(++/0)$. Therefore, a constant shift for the relative formation energies of all charge defects is found: $\epsilon_{TVB} = 0.328$ for LDA calculations and $\epsilon_{TVB} = 0.159$ eV for GGA calculations.

The bandgap values computed with the LDA and GGA Hamiltonians are not reported in [106]; but they report to obtain the same convergence values as in [105] for the LDA Hamiltonian, where the bandgap value is obtained to be 0.47 eV. Since both LDA and GGA Hamiltonians underestimate the bandgap, a major inconsisntency in the methodology in [106] is that the transition levels are com-

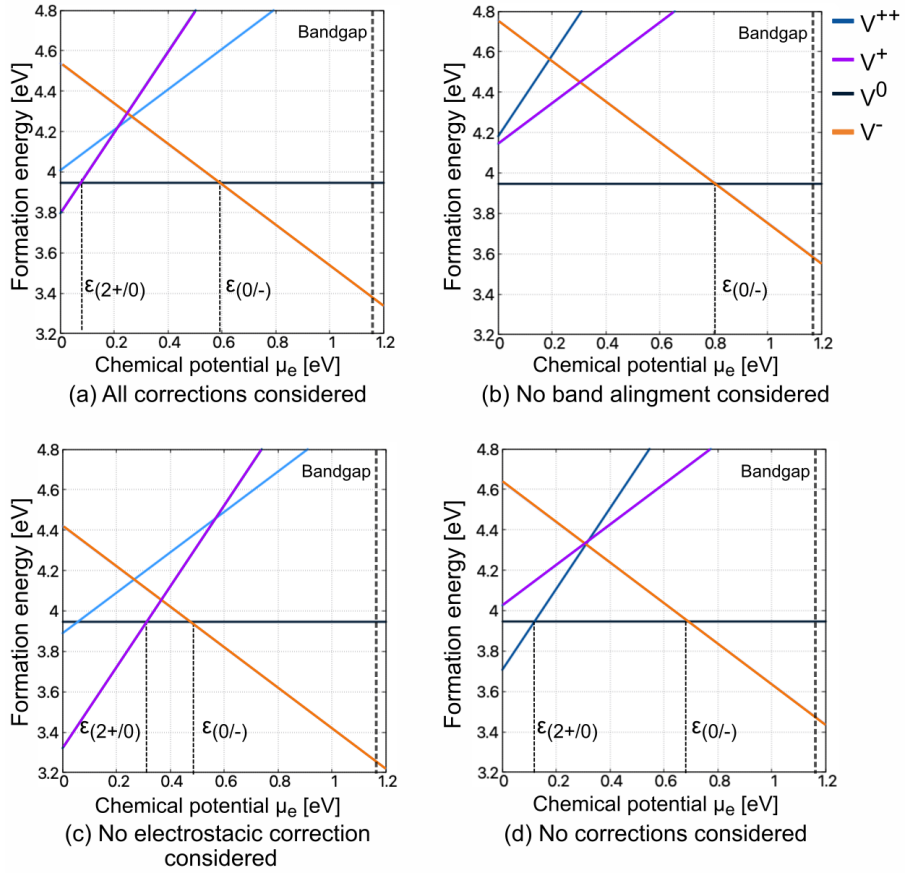

Figure 3.13: Formation energy dependency on the chemical potential. Comparison between different corrections schemes.

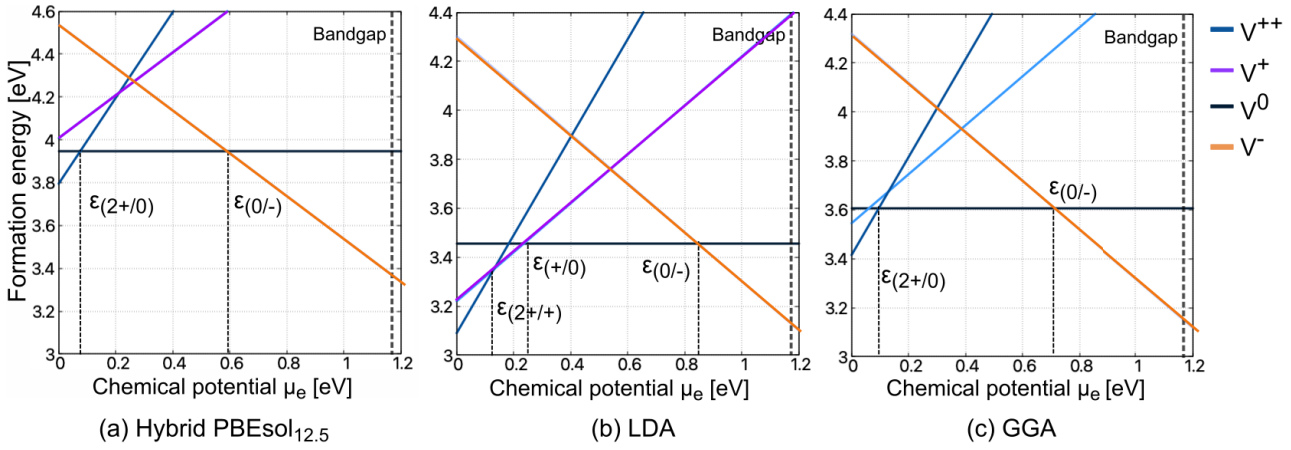

Figure 3.14: Formation energy dependency on the chemical potential. Comparison between results obtained in this work and the LDA and GGA results presented in [106]. The bandgap value presented in the figure for (b) and (c) is the measured bandgap of silicon, as the results in [106] were fitted to experimental results.

pared with the experimental bandgap value of silicon, which is indicated in figures 3.14 (b) and (c). According to [106], "*an optimal procedure for determining* ϵ_{TVB} *has not yet been determined and, as such, the present approach should be viewed as provisional.* "
The behavior of the transitions between the most stable states of the single vacancy obtained within our correction scheme shows a marked resemblance to do the results obtained in [106], considering that they were obtained with a questionable methodology. This comparison emphasizes the importance of a consistent correction scheme preferably independent from experimental values and it underlines the validity of our corrections scheme.

3.4.3 Charge recombination properties of the vacancy

An analysis of the optoelectronic properties of the defective structures was also performed for the different charge states of the silicon vacancy. Table 3.7 shows the changes in the dielectric constant and ΔE_Γ of the structures containing hydrogen impurities with respect to the values computed with $PBEsol_{12.5}$ for a perfect crystalline structure. We observed that the presence of all charge states in the crystalline structure has an influence on the dielectric constant: the more electrons are present in the vacancy, the smaller the effect on ϵ. Because the Γ-point is not the minimum for the energy difference between the Fermi level and the first unoccuppied state, we do not observe a relation between ΔE_Γ and ϵ. However, from Figure 3.11 we observe that the lower this energy difference, considering the minimum of the first unoccupied state, the higher the dielectric constant. Therefore, an increase in the dielectric constant implies a higher recombination probability for each charge state of the vacancy.
In order to propose the evolution of a single vacancy when electrons are added or removed, we first consider that the second donor level $\epsilon(+/++)$ lies in the bandgap, but, due to the Jahn Teller effect, the transition level $\epsilon(0/+)$ is located below it. We recall from figure 3.12 that V^+ is a metastable state. To lower the energy of the system, it will evolve to the stable states V^0 and V^{++} according to

$$2V^+ \rightarrow V^0 + V^{++} \tag{3.6}$$

Defects	**Dielectric constant** ϵ	$\Delta_{\epsilon\%}$	ΔE_Γ **[eV]**	**Bandgap**
V^{++}	13.090	21.632	0.712	Indirect
V^{+}	12.791	18.871	0.498	Indirect
V^{0}	11.396	5.888	1.001	Indirect
V^{-}	11.272	4.720	0.723	Indirect
Crystal	10.762	0	1.171	Indirect

Table 3.7: Comparison of dielectric constant and bandgap values of structures containing a single vacancy in different charge states.

In agreement with EPR measurements, the charge state V^+ has only been observed by photoexcitation at cryogenic temperatures [112]. Additionally, the activation energy determined by these experimental observations is 0.057 eV, which indicates the release of a hole due to thermal fluctuations. The kinetics of V^+ are given by

$$V^+ \rightarrow V^0 + h^+ \tag{3.7}$$

According to our calculations, the donor level $\epsilon(0/+)$ that determines this reaction is located at $\epsilon_{TVB} - 0.05$, whereas experimental measurements locate the donor state at $\epsilon_{TVB} + 0.05$ eV. This inconsistency of 0.1 eV might come from numerical errors and the used correction scheme. The fact that this transition level lies that close to the TVB, along with the stability of the V^{++} defect, suggests that the initial transition comes from V^{++}

$$V^{++} \rightarrow V^+ + h^+ \rightarrow V^0 + 2h^+ \tag{3.8}$$

We find the transition level $\epsilon(+/++)$ at 0.21 eV while it has been observed experimentally at $\epsilon_{TVB} + 0.13eV$ using deep-level capacitance transient spectroscopy (DLTS) [112]. The fact that $\epsilon(+/++) > \epsilon(0/+)$ indicates that the hole involved in the first ionization is bound more strongly than that in the second one. Therefore, once the first hole is emitted, the second hole follows immediately. This result emphasizes the instability of V^+.
Finally, the neutral vacancy V^0 is stable up to the transition level $\epsilon(0/-)$ where it recombines with an electron to form V^-

$$V^0 + e^- \rightarrow V^- \tag{3.9}$$

These reactions are likely to occur in the absence of impurities. Several impurities tend to diffuse in the Si material toward vacancies, where they act as substitutional defects.

3.5 Interstitial silicon

Although the existence of interstitial silicon Si_i is well known, its study is difficult because of the lack of direct experimental observations of its existence, structure, or characteristics. Furthermore, there is little agreement in the literature regarding the structural and electronic properties of the various charge states of interstitial Si. Previous ab initio studies of Si_i indicate that the interstitial

may exist in five charge states, specifically $Si_i^{--}, Si_i^{-}, Si_i^{0}, Si_i^{+}$ and Si_i^{++} [113, 114, 115, 116]. Figure 3.15 shows the possible locations of interstitial silicon. The position of each charge state depends on the charge of the defect. While the interstitial Si_i^{+} and Si_i^{++} charge states are typically positioned in a tetrahedral (or near-tetrahedral) configuration, the Si_i^{--}, Si_i^{-} and Si_i^{0} charge states are usually located in split-[110] positions [117]. Nevertheless, other studies propose that the charge states Si_i^{+} are located in a BC position [118].

To retrieve the most stable configuration of each charge state, relaxation of the host atoms around the impurity was included in our calculations. The initial position of the five charge states was considered to be the tetrahedral position because in this position the defect is less likely to disturb the position of the host atoms. Nevertheless, the initial configuration of the charge states Si_i^{--}, Si_i^{-} and Si_i^{0} was also tested as a split-[100] defect structure. All possible spin configurations for each charge defect were computed to ensure the stability of the defect with respect to the spin. The tested spin configurations depend on the parity of the number of electrons in the system, according to the defect considered and its charge. The most stable configuration corresponded to the lowest total energy.

The formation energy of the interstitial silicon was computed according to

$$E_{form}[Si_i^q] = E_{TOT}[Si, Si_i^q] - \frac{N+1}{N} E_{TOT}[Crystal] - q(\epsilon_{TVB} - \epsilon_F) + \Delta E_{elec} \tag{3.10}$$

where $E_{form}[Si_i^q]$ is the formation energy of interstitial silicon, $E_{TOT}[Si, Si_i^q]$ is the total energy of the system with Si_i^q, and $E_{TOT}[Crystal]$ is the energy of the perfect crystalline structure. The factor $\frac{N+1}{N}$ comes from the addition of an extra Si atom originating from the crystalline silicon. Convergence with respect to the supercell size was checked, like for the previous structures in this work, and it was obtained for supercells containing 216 atoms.

The relaxed positions of the charge defects were found to be in the split-[110] structure for the Si_i^{--}, Si_i^{-} and Si_i^{0} charge states. Interstitial Si_i^{+} along with the double ionized charge state Si_i^{++}

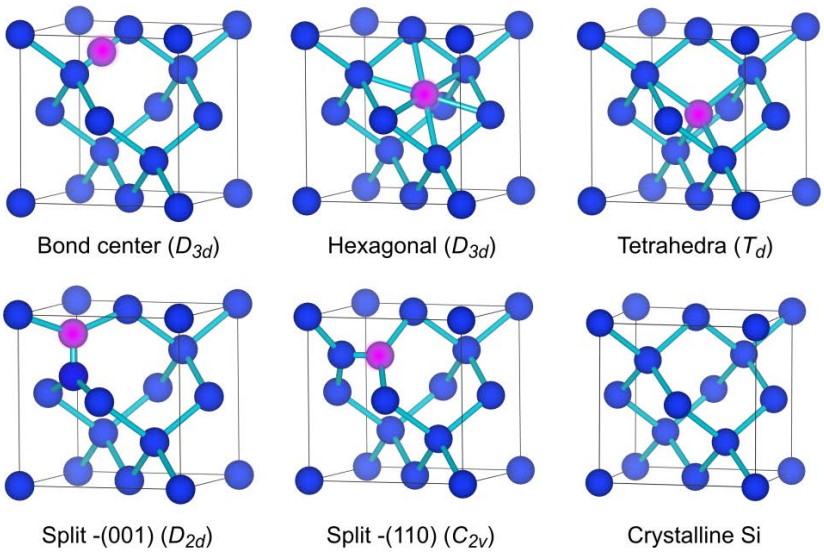

Figure 3.15: Structures of silicon self-interstitials, Si_i atoms are indicated in pink color. For the split-[001] and split-[110] structures, the interstitial atom cannot be distinguished from one of the host atoms. The point symmetry of each structure is indicated in parentheses.

Defect	$\Delta\epsilon_{TVB}$ **[eV]**	$E_{form}[Si_i^q]$ **[eV]**	**Band gap [eV]**
Si_i^{--}	-0.595	5.682	1.243
Si_i^{-}	-0.320	5.059	1.221
Si_i^{0}	-0.147	4.214	1.221
Si_i^{+}	-0.112	3.725	1.211
Si_i^{++}	-0.180	3.167	1.209

Table 3.8: Bands alignment, formation energy and band gap values for different charge states of interstitial silicon defects.

were found to be at T_d position. The structures Si_i^{--}, Si_i^0 and Si_i^{++} were found to be more stable in a configuration obtained with closed shell calculations. In the cases of Si_i^- and Si_i^+ a total spin of 1 was found in the most stable structures. We took into account an electrostatic correction of $\Delta E_{elect} = -q^2 \times 0.118eV$ in our correction scheme, while the values of the band alignment varied for each structure. This value, along with the formation energy and band gap value are presented in Table 3.8.

By analyzing the formation energies of the various charge states of Si_i as a function of the chemical potential, the relative stability of each state was determined. The dependence of $E_{form}[Si_i^q]$ on ϵ_f is presented in Figure 3.16, where the Fermi level is referenced to the top of the valence band.

The transition levels that determine the chemical potential range in which each charge state is stable are $\epsilon(2+/0) = 0.516$ and $\epsilon(0/2-) = 0.731$ eV. They describe the evolution of Si_i when adding or removing electrons. Si_i^{++} will be the most stable charge state for regions with a chemical potential below $\epsilon(2+/0)$. Regions with a chemical potential between 0.561 and 0.731 are more likely to present Si_i^0 and for energies above the 0.731 eV, the most stable state will be Si_i^{--}.

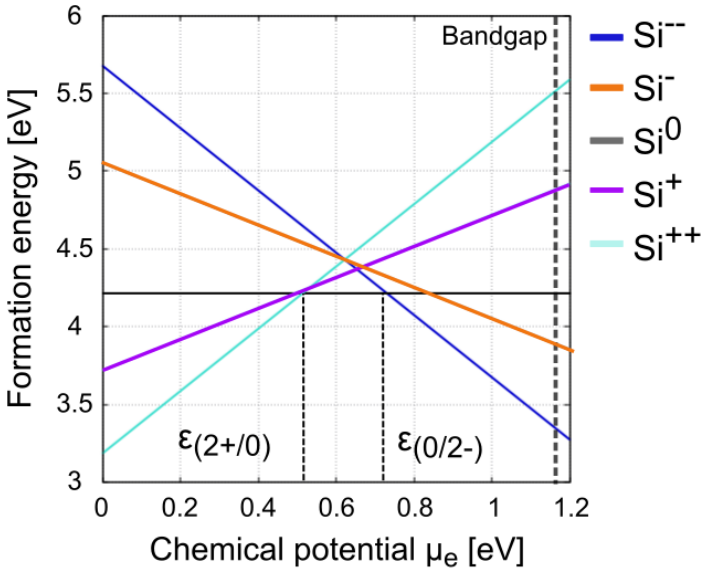

Figure 3.16: Relative formation energies for the interstitial silicon charge states as a function of the chemical potential.The transition levels are indicated.

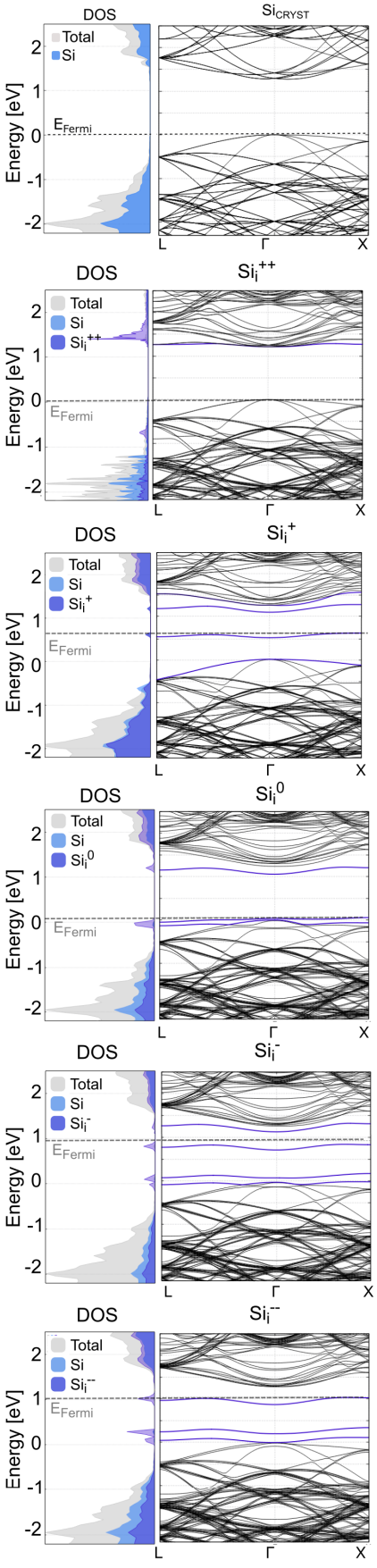

Figure 3.17: Band structure of different charge states of Si_i.

We observe that the transition level $\epsilon(-/0)$is equal to $\epsilon(0/2-)$. The transition between Si_i^{--}, Si_i^{+} and Si_i^{++} occur at the same Fermi level at 0.623 eV.

3.5.1 Electronic properties of Si_i

The different band structures and density of states for the charge states of the silicon-interstitial are presented in Figure 3.17 in comparison to that of crystalline silicon.

The band structure calculations show that the most stable charge state Si_i^{++} does not induce any energy level in the band gap, but only affects the bottom of the conduction band by adding an empty energy level. The Fermi energy of the defective structure containing this defect remains the same as that of crystalline Si. The absence of unpaired electrons in the interstitial Si_i^{++} explains that this defect does not induce any energy level in the band gap; therefore, the additional energy level near the bottom of the conduction band originates from the change in geometry from the crystalline structure to the split [110].

The addition of an electron to this defective structure leads to interstitial Si_i^{+}, and the system does not undergo any change in geometry. The additional electron bonds to the interstitial silicon atom and gives rise to an occupied energy level in the gap, which increases the Fermi energy of the system to 0.63 eV.

An additional electron in this structure pairs with the electron lying in the energy level in the middle of the bandgap, leading to the neutral interstitial Si_i^{0}. Once again, this defect has no unpaired electrons; therefore, there is no energy level in the bandgap. The two extra electrons lie in the valence band, and the system does not experience any change in geometry; thus, the Fermi energy of the system decreases to that of the perfect crystalline structure.

Interstitial Si_i^{-} is obtained by adding an electron to the previous system. In this case, the interstitial defect moves from the split-[110] location to the T_d position. The system will experience a geometry transformation. This additional electron occupies a conduction-band-like state, increasing the Fermi energy of the system to 0.93 eV. This conduction-band-like state will be filled in the presence of an additional electron, which would be the case for interstitial Si_i^{--}.

3.5.2 Formation energy and transition level analysis

The effect of the correction scheme selected in this study on the stability behavior of charge defects is shown in Figure 3.18. Only transition levels that determine the relative stability of the most stable interstitials are shown for each scenario of corrections.

We observed that the band alignment correction $\Delta\epsilon_{TVB}$ modifies the relative stability of the defects (Fig. 3.18(b)) by shifting the position of the transition levels to higher energy values. The transition level $\epsilon(2+/0)$ moves $\sim 2eV$ and determines the behavior of the most stable charge states in this scenario. Figure 3.18(c) results in a much more radical scenario where only the doubly ionized charge states Si_i^{++} and Si_i^{--} are stable. Form Figures 3.18(b) and (c) the electrostatic correction shifts the formation energy differences with respect to the neutral charge state, while the band alignment shifts the transition levels to higher values.

The energy differences between the total energies of each charge state of Si_i are shown in Figure 3.18(d). We observed that the energy difference between a charge state and that containing an extra electron is approximately constant (~ 1 eV). This indicates that the total energy differences are about equivalent to the energy required to add an electron to a bulk supercell using the same set of computational parameters.

Several *ab inito* studies based on DFT have considered the case of interstitial silicon and their different charge states. In Figure 3.19 we compare the relative formation energies obtained for Si_i charge states in our study with the results of Ref. [119], where the LDA Hamiltonian and GW

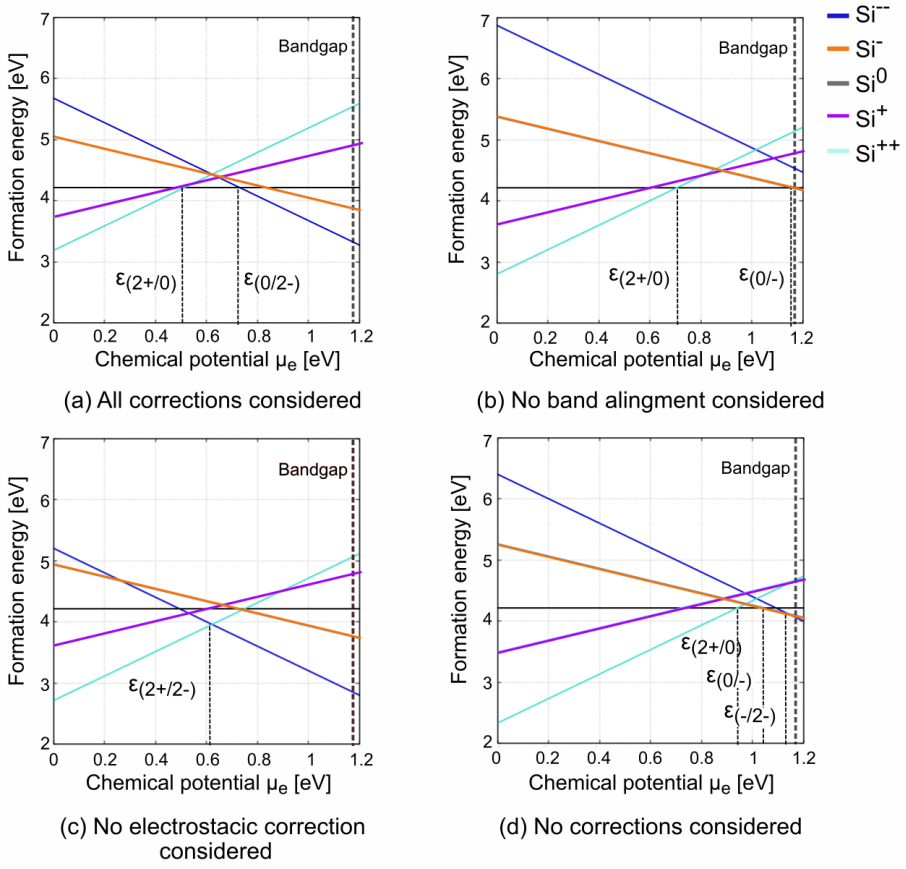

Figure 3.18: Formation energy dependency on the chemical potential. Comparison between different corrections schemes.

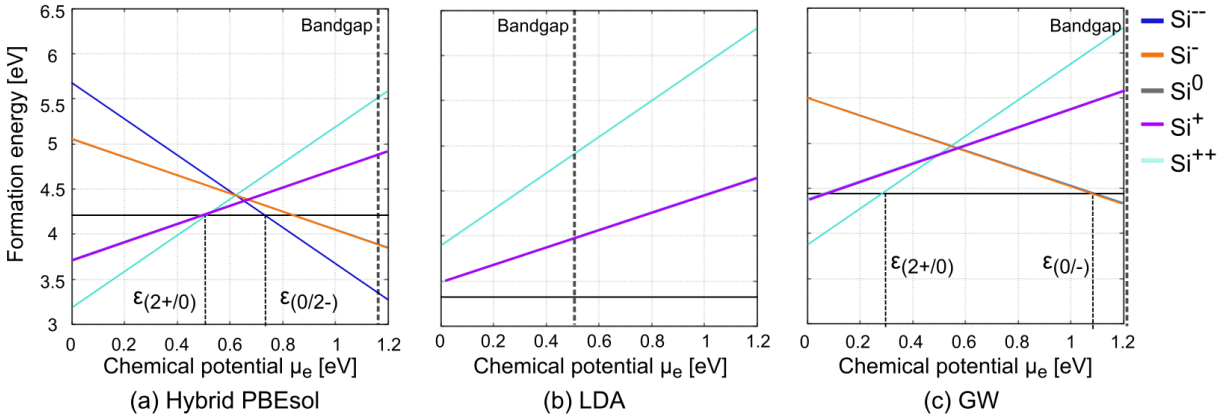

Figure 3.19: (a) Relative formation energies obtained for Si_i charge states as a function of the chemical potential μ for a converged supercell with 216 atoms using $PBEsol_{12.5}$. (b),(c)The results of LDA and GW [119] are presented in comparison.

method are used. The three approaches present different transitions between the most stable charge states for each Hamiltonian. LDA underestimates the formation energies of Si_i^+ and Si_i^0 with respect to Si_i^{++} [119] whereas we seem to underestimate the value of the formation energy of Si_i^{++} and Si_i^+ with respect to the rest of the charge states of Si_i in comparison to the the GW approach, resulting in different behaviors. In particular, the energy range where the neutral charge states is stable is shorter in our results with respect to the GW approach.

In both correction schemes, ours and the GW one used in [119], the electrostatic correction is defined according to the Markov Payne formulation. However, the band alignment in [119] was performed by considering the electron affinities of each charge system. Electron affinities were computed using Hedin's GW method [120]. The correction regarding the alignment with respect to the electron affinity is a function of charge for each defective structure, unlike our correction in the core band alignment, where $\Delta\epsilon_{TVB}^q$ has not a explicit relation with respect to q.

Table 3.9 shows a comparison of the transition levels computed with respect to those obtained using the GW method [119] and $PBEsol_{12.5}$ within a different correction scheme, obtained in [98]. In the last one, the correction scheme involves two aspects. First, the formation energies were computed with respect to the Fermi level, which was aligned to the experimental valence band edge. This procedure is included in our calculations by referencing ϵ_{TVB} to vacuum (ionization energy) using equation 2.29. Second, the transition levels were computed according to

Transition level	$PBEsol_{12.5}$ [eV]	$PBEsol_{12.5}$ [eV] $\Delta^D(L)$ [98]	**GW** [eV]] [119]
$\epsilon(2+/0)$	0.512	0.887	0.282
$\epsilon(2+/+)$	0.529	1.176	0.498
$\epsilon(+/0)$	0.498	0.605	0.061
$\epsilon(0/-)$	0.842	1.122	1.083
$\epsilon(-/2-)$	0.623	1.702	—-

Table 3.9: Transition levels obtained in our calculations ($PBEsol_{12.5}$) compared to different *ab initio* studies. In all the cases, ϵ_{TVB} was referenced to 0.

Defect	**Dielectric constant ϵ**	$\Delta_{\epsilon\%}$	ΔE_Γ **[eV]**	**Bandgap**
Si_i^{++}	11.240	4.442	1.209	Direct
Si_i^{+}	11.456	6.451	0.622	Direct
Si_i^{0}	11.273	4.752	1.221	Indirect
Si_i^{-}	11.985	11.363	0.352	Indirect
Si_i^{--}	14.608	30.717	0.321	Direct
Crystal	10,762	0	1.171	Indirect

Table 3.10: Dielectric constatn and ΔE_Γ Relative formation energies and band gap values for supercells of different sizes containing interstitial silicon charge states.

$\Delta^D(q-1 \leftrightarrow q, L) = \Delta^D(q-1, L) - \Delta^D(q, L)$, where $\Delta^D(L) = \Delta^D(L \rightarrow \text{inf}) - \frac{A_1}{L} + \frac{A_3}{L^3}$. The term $\frac{A_1}{L} = \Delta E_{elec}$ whereas $\frac{A_3}{L^3} = \frac{\alpha e^2((q-2)^2 - q^2)}{4\epsilon}$ is the next term in the Makov-Payne series, not considered in our scheme. Nevertheless, the work in [119] lacks alignment between the defective structures, leading to important differences from our results.

3.5.3 Charge recombination properties of the self-silicon interstitial

An additional investigation of the optoelectronic properties of Si_i was carried out. The variations in the dielectric constant and ΔE_Γ of the structures containing different charge states of Si_i is presented in Table 3.10. Even if the structure Si_i^{++} is recombination-inactive, it exhibits a change in the dielectric constant of 4% which is attributed to the change of geometry with respect to the crystalline Si.

From the analysis of the formation energies of the different charge states of Si_i, considering the influence of our correction scheme, we observe that the $\epsilon(2+/0)$,$\epsilon(2+/+)$ and $\epsilon(+/0)$ lie around the same Fermi level. This indicates that the charge state Si_i^{++} remains stable with an increase in the electron density (increase in the chemical potential) until two electrons are bound to give rise to Si_i^0. The transition $Si_i^+ \rightarrow Si_i^0$ occurs in the same region, indicating that Si_i^+ may occur as intermediate fast transitions of $Si_i^{++} \rightarrow Si_i^0$. Si_i^0 is stable and it is likely to acquire two additional electrons and stabilize as Si_i^{--}. The fact that the transition level $\epsilon(0/-)$ lies near $\epsilon(0/2-)$ indicates that Si_i^- might also be a fast transition state of $Si_i^0 \rightarrow Si_i^{--}$.

Our conclusion that charge states inducing energy levels that are singly occupied in the band gap occur only as fast transitions suggests that charge carrier recombination is a punctual process that stabilizes the silicon interstitials. However, these transitions do not appear to induce recombination.

3.6 Conclusions

The study of hydrogen impurities and self-silicon defects, such as single vacancies and interstitial hydrogen, in crystalline silicon was performed to understand the origin and dynamics of LeTID degradation. These defects were chosen as a first approach to understand this degradation because they are common in silicon wafers grown using different methods, and LeTID degradation

has been observed as a universal degradation in silicon-based modules. The study of these defects within the DFT approach has not yet been tackled in the LeTID understanding scheme, even if their structural and electronic properties have already been analyzed by ab initio studies.

Significant discrepancies have been observed between earlier ab initio studies on hydrogen impurities and self-silicon defects. To properly analyze our results and justify the differences between our results and existing experimental values, we compared our results with previous experimental and theoretical studies. We worked with the Hamiltonian $PBEsol_{12.5}$ and used a well-defined correction scheme.

Our results were carefully compared with other ab initio studies because several parameters, especially the choice of the Hamiltonian, significantly affect the results concerning the relative stability of the defects. These differences arise from the well-known bandgap problem associated with the DFT approach. Some ab initio studies have corrected this issue by scaling or shifting their results [48, 49]; that is, for a charge defect, the formation energy and transition level values within the bandgap are multiplied by a correction factor that corresponds to the factor that adjusts the value of the DFT bandgap to the experimental value. In addition, one of the transition levels lying in the bandgap is usually shifted to its experimental value; thus, the ensemble of formation energies and transition levels of different charge states of the defect is more likely to agree with the experiments. This is the case in Refs. [49, 106]. However, this procedure results in an inaccurate methodology that, rather than providing reliable results and physical insight, seeks to fit DFT energies to experiments. In our study, a hybrid functional is used to avoid the bandgap problem. Some previous DFT studies that have used hybrid functionals to study self silicon defects still rely on experimental values, as they reference the DFT energies by the use of the so called "maker method"[106, 119]. In our case, the hypotheses of the marker method are already included in our correction scheme, without the need to reference any value to experimental measurements.

In order to properly study point defects in crystalline silicon, we propose a methodology in which the correction scheme is well defined and independent of experimental measurements. The correction scheme is described in detail in sections 2.4.2 and 2.4.4. Within our correction scheme, the range in which the transition levels could vary was approximately 0.25 eV for hydrogen, interstitial silicon, and vacancy defects. Even if this range is large compared to the value of the silicon bandgap (1.17 eV), the relative stabilities obtained in all cases were consistent. Our results are in good agreement with the experiments for the three defects, which ensures the reliability of the Hamiltonian and the correction scheme. An analysis of this type has not been reported for hydrogen and self-silicon defects using a correction scheme that does not only fit the experimental data.

According to our results, hydrogen-induced recombination is likely to occur in bulk silicon and cause LeTID. Our results show that interstitial silicon and vacancies might act as charge carrier traps as well, nevertheless, these structures are likely to interact with other impurities. within crystalline silicon. For example, it has been recently proposed from experimental observation that the defect responsible for LeTID might be a dangling bond in a silicon vacancy with H atoms in its vicinity and oxygen backbonds [121]. The cases of structures containing hydrogen interacting with dangling bonds in vacancies or interstitial silicon, treated in works like [100], remain to be studied within our methodology.

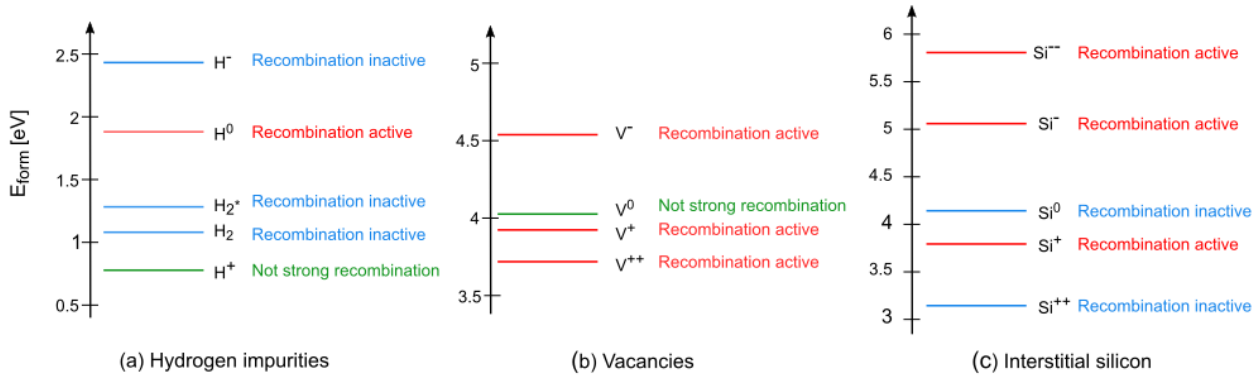

Figure 3.20: Formation energy and recombination properties of hydrogen impurities, silicon vacancieans and interstitial silicon atoms.

To propose the evolution of the different configurations of the studied defects for LeTID dynamics, the silicon defects were classified into three configurations based on the model described in Section 1.4: defects in the initial state **A** and recovery phase **C** are stable and unable to recombine with charge carriers, whereas defects in degradation phase **B** are in configurations with higher formations energies than those in **A** and **C** and can recombine with charge carriers. This required to classify the studied defects according to their recombination properties:

- *Inactive to recombine* refers to defects that do not induce energy levels on the bandgap; therefore, with $\Delta E_\Gamma > 0.9$ eV.
- *Not strong recombination* groups defects that induce energy levels near the bangap edges, so that they satisfy $0.7 < \Delta E_\Gamma < 0.9$.
- *Recombination active* refers to defects induce energy levels near the middle of the bandgap and satisfy$\Delta E_\Gamma E < 0.7$.

Even if these recombination categories are defined in arbitrary ranges of ΔE_Γ, they are convenient to propose the evolution of impurities formation that follow the conditions of LeTID conditions. It is observed from Figure 3.20(a) that H_2 and H_2^* are found to be more stable than H^0 and H^-, which suggests these two configurations constitute states **A** and **C** from our LeTID model, while H^0 represents a defect in state **B**. Figure 3.20(b) shows that a possible LeTID scenario concerning vacancies would involve V^0 to be considered in states **A** and **C**, while V^- would be attributed to state **B**. However, further research is necessary to examine the recombination ratio of neutrally charge vacancies to validate this model. Concerning interstial silicon defects, Figure 3.20 shows that the charge states Si^0 and Si^{++} can be classified as configurations in states **A** and **C**. From an analysis of the formation energy as a function of the chemical potential we see that the charge defects Si^- and Si^+ are never the most stable defect for a given chemical potential value within the bandgap, therefore, we suggest that Si^{--} is attributed to state **B**.

CHAPTER 4

The role of metal defects on LeTID

The recombination activity caused by the deep states associated with transition metal impurities in Si is well known [10]. In particular, a comprehensive experimental analysis comparing the occurrence of LeTID in samples containing metallic impurities versus samples where these impurities were passivated is presented in [46] and has proven that the LeTID extent decreases with the amount of active metallic impurities. In addition, it has been observed that the degradation caused by metallic impurities is not only dependent on their thermodynamic activity but also on their diffusivity, where impurities with higher diffusivity tend to degrade cell efficiency more significantly [122].

Interstitial metal-hydrogen complexes have been postulated as a possible cause of LeTID, given the crucial role of hydrogen as a precursor for this phenomenon, as well as the hypothesis that this defect may bind to other impurities[15, 30, 37, 43, 44, 45, 46]. This hypothesis has been supported by different experimental studies [46, 123] and has led to two models described by three phases: phase 1 corresponds to the initial state of the LeTID defects, phase 2 corresponds to the degradation, and phase 3 corresponds to the regeneration processes.

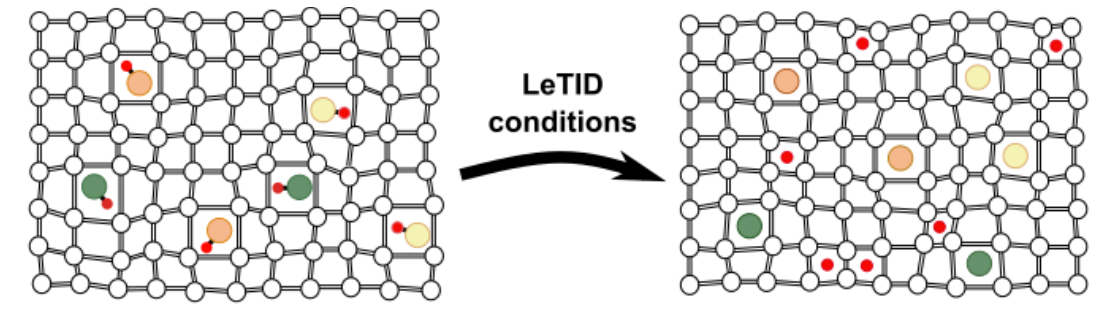

Figure 4.1: LeTID model 1: It is suggested that degradation is caused by dissociation of a metal-hydrogen ($M_i - H$) complex. The hydrogen is introduced during firing and initially passivates the metal impurities M_i. During excess carrier injection and increased temeprature, the $M_i - H$ complex dissociates and recombination-active M_i centers limit the lifetime [46].

MODEL 1 (Fig. 4.1)

1. **Phase 1**.H is released from the passivation layers during the fast firing process and passivates the metal impurities, located in an interstitial position (M_i). Such $M_i - H$ complexes are not strong recombination centers and may even be completely recombination-inactive.

2. **Phase 2**: During illumination at enhanced temperature, the $M_i - H$ complex dissociates, leading to isolated M_i, which is assumed to be highly recombination-active. Hydrogen atoms either form H_2 or attach to other defects that are abundant in silicon.

3. **Phase 3**: M_i defects are passivated, either with hydrogen atoms or by diffusing toward grain boundaries or interfaces.

An alternative LeTID mechanism considering metal-hydrogen complexes suggests that each metal atom is bound to several hydrogen atoms. These complexes would evolve in the following manner:
MODEL 2 (Fig. 4.1)

1. **Phase 1**. The interstitial metallic impurity M_i is initially passivated with several hydrogen atoms.

2. **Phase 2**: During LeTID some of the hydrogen atoms detach. The remaining recombination-active centers are not isolated M_i but metal-hydrogen complexes possessing an energy level within the silicon band gap.

3. **Phase 3**: $M_i - H$ complexes are passivated, either with hydrogen atoms or by diffusing toward grain boundaries or interfaces.

Some studies consider that lifetime regeneration is attributed to the diffusion of the recombination-active impurity to the wafer surface, where it is permanently trapped[52]. By modeling the lifetime dependence of the wafer thickness measured experimentally, the diffusion coefficient of the impurity was determined to be in the range of $(5 \pm 2) \times 10^{-11} cm^2 s^{-1}$ at a temperature of 75ºC [52]. The cobalt and nickel diffusion coefficients were found to fit the model, indicating that these defects play a role in LeTID degradation. Although these defects are known to be detrimental to

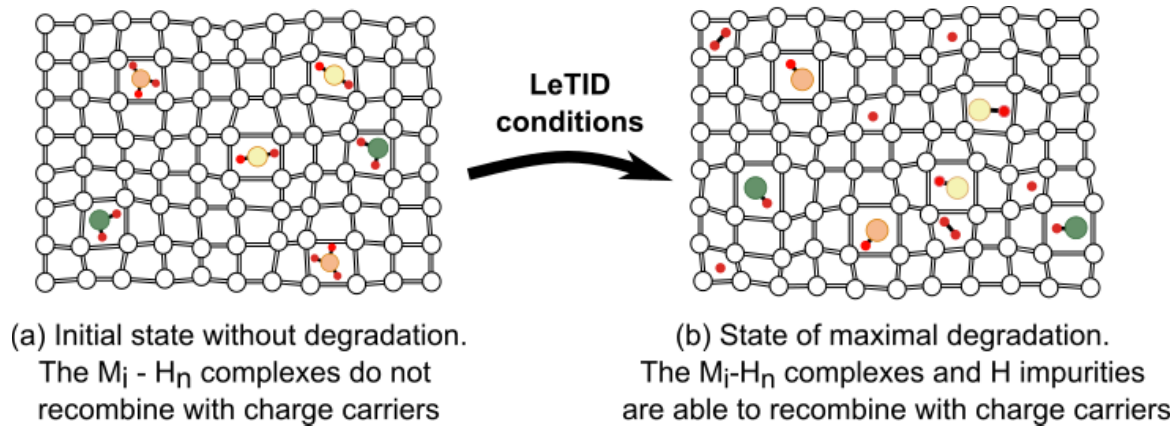

Figure 4.2: LeTID model 2: Hypothesis considering $M_i H_n$ defects as a cause of LeTID [46].

silicon materials, there is little information about the stability and transition levels of these impurities when they occupy interstitial positions. Nickel, cobalt, and their complexes with hydrogen have been primarily studied as substitutional defects [94, 124, 125, 126]. Experimentally,interstitial Ni or Co has been observed by means of deep level transient spectroscopy (DLTS) measurements [126], probably because of their fast diffusion in silicon. Nevertheless, it has been observed that transition metals coming from the silicon synthesis process occupy an interstitial position and can be repositioned as substitutional defects in the presence of excess vacancies [123].
At the microscopic scale, a first-principles study of point metallic defects in crystalline silicon to explore the causes of LeTID has not yet been presented. To provide theoretical insight into both models, this chapter addresses the study of nickel and cobalt impurities and their respective hydrogen complexes using the $PBEsol_{12.5}$ hybrid functional. First, an analysis of metals in both interstitial and substitutional positions was performed. Subsequently, the complexes were considered to be metallic atoms bound to one hydrogen atom in any of the three charge states or to an H_2 molecule. Finally, to investigate the potential diffusion of metal-hydrogen complexes toward grain boundaries or interfaces, the study was extended to consider three different types of simple dislocations: simple dislocations, dislocation edges, and twin-type grain boundaries.

4.1 Nickel impurities in silicon

To understand the behavior of an isolated nickel atom in silicon and its interactions with other impurities, it is necessary to investigate the stability of various configurations, including interstitial (Ni_i) and substitutional (Ni_s) configurations. Therefore, this study re-examine the properties of nickel defects in these two configurations. Unlike Chapter 3, this section does not study the different charge states of the impurity, and it focuses exclusively on neutral nickel impurities Ni_s and Ni_i. Indeed, experimental evidence suggests that nickel cannot induce charge carrier recombination on its own [125]. It has been measured experimentally that substitutional nickel exists in different charge states in silicon and that the transition levels are located at $\epsilon(2-/-) = \epsilon_{BCB} - 0.08$, $\epsilon(-/0) = \epsilon_{BCB} - 0.39$, and $\epsilon(0/+) = \epsilon_{TVB} + 0.15$ [124]. The position of the transition level $\epsilon(2-/-)$ suggests that the double-charged state is never the most stable charge state of substitutional nickel. From the position of $\epsilon(-/0)$ it is inferred that the neutral charge state of Ni_s is the most stable state for a large range of chemical potentials within the bandgap; therefore, it is

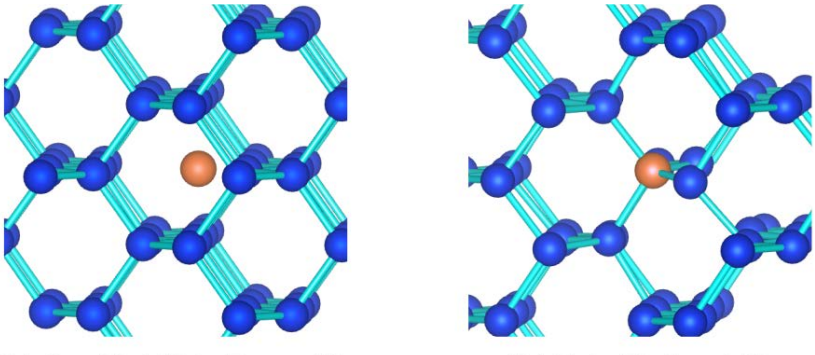

Figure 4.3: Defective structure of interstitial and substitutional nickel in crystalline silicon

unlikely that it will self-induce recombination.
The stability of nickel impurities is studied by analyzing the formation energy. We compute the formation energy for a nickel impurity in an interstitial position as

$$E_{form}[Ni_i] = E_{TOT}[Si, Ni_i] - E_{TOT}[Crystal] - E_{atom}[Ni] \tag{4.1}$$

where $E_{form}[Ni_i]$ is the formation energy of the defective structure containing interstitial nickel, $E_{TOT}[Si, Ni_i]$ is the total energy of the system with the nickel atom, and $E_{TOT}[Crystal]$ is the energy of the perfect crystalline structure and $E_{atom}[Ni]$ is the energy of an isolated nickel atom in vacuum. The formation energy of the substitutional configuration is calculated using the same approach, but with an additional term that reflects the removal of one Si atom from the crystal structure, which is given by $\frac{N-1}{N}E_{TOT}[Crystal]$.The formation enregy for Ni_s is given by

$$E_{form}[Ni_s] = E_{TOT}[Si, Ni_s] - \frac{N-1}{N}E_{TOT}[Crystal] - E_{atom}[Ni] \tag{4.2}$$

To ensure the accuracy of the obtained results, the convergence of the formation energy and bandgap values were evaluated in relation to the size of the supercell. It was obtained for supercells containing 216 atoms for the susbtitutional and interstitial configurations. For all defective structures, computations were performed with and without considering spin depending on the electronic configuration of the considered defects or complexes. The total energies were compared to determine the most stable spin configuration for each charge state. In both cases, the most stable structures were obtained with closed shell calculations.
The structures containing the metallic impurities are presented in Figure 4.3. We observe that Ni_i occupies an interstitial position and it is found to be located at a distance of 2.395 Å from the nearest neighboring silicon atoms. The distance between the $Si-Si$ atoms surrounding the interstitial nickel impurity remain at 2.350 Å, meaning that the crystalline structure is not importantly affected because the perfect crystalline silicon is 2.352 Å. In the case of the substitutional nickel impurity Ni_s the distance with respect to its neighboring atoms is 2.221 Å, which compared to the $Si-Si$ distance in crystalline silicon, corresponds to a change of 5.56%.
The formation energies and lattice parameters of a supercell containing 216 Si atoms are listed in Table 4.1. Results show that the interstitial position is approximately ~ 1.3 eV more stable than the substitutional configuration of Ni. However, Ni_i has not been observed in silicon by experimental studies, contrary to Ni_s [125].
To investigate the possibility of nickel atoms substituting silicon atoms in the presence of vacancies, we constructed a structure with a nickel atom initially in a T_d position adjacent to a neutral silicon vacancy. Relaxation of the host atoms around the impurity was allowed by minimizing the energy with respect to the atomic positions and cell deformations. After this optimization, the

	E_{form} **[eV]**	**Lattice parameter** a [Å]	Δa[%]	**Lattice angles** [°]
Ni_i	-6.730	15.293	-6.149	90
Ni_s	-5.347	16.255	0.245	89.992

Table 4.1: Properties of nickel impurities: relative formation energy, lattice parameter and percentage change of the lattice parameter for supercells with 216 Si atoms.

nickel atom did not occupy the substitutional position. The total energy of such a structure was found to be −4.048 eV, ~ 1 eV higher than the formation energy of Ni_s, indicating the existence of a potential barrier that the nickel atom has to overcome in order to be located in a substitutional configuration. These findings reinforce the hypothesis of model 1 and 2 [46] where an interstitial metallic impurity, such as nickel, might be involved in LeTID.

4.1.1 Electronic properties of nickel impurities

From the band diagram of the nickel impurities presented in figure 4.4 it is observed that interstitial nickel does not affect the band structure of crystalline silicon, as it does not induce any energy level in the bandgap and it only increases the band gap value by 2.7% (Table 4.2). Contrary to Ni_i, Ni_s induces an energy level in the band gap located 0.639 eV above the top of the valence band. The energy level within the bandgap attributed to Ni_s can be explained by a Jahn-Teller distortion experienced by Ni_s [125]. We observe that this energy level is empty.

We define ΔE_Γ as the energy difference at the Γ-point between the Fermi level and the first unoccupied energy level. This variable turns out to be convenient to analyze the change of the dielectric constant of each structure. Indeed, an increase in the dielectric constant can be related to the existence of energy levels in the band gap. The lower the value of ΔE_Γ, the higher the probability of recombination, resulting in an increase in the dielectric constant.

Table 4.2 shows that Ni_s exhibits an increase in ϵ caused by the decrease of ΔE_Γ. Therefore, Ni_s might act as a charge recombination center.

	ΔE_Γ [eV]	**Bandgap**	**Dielectric constant** ϵ
Ni_i	1.139	Indirect	10.92
Ni_s	0.639	Indirect	11.44
Si	1.171	Indirect	10.762

Table 4.2: Electronic properties of nickel impurities. ΔE_Γ refers to the energy difference at the Γ-point between the Fermi level and the first unoccupied energy level.

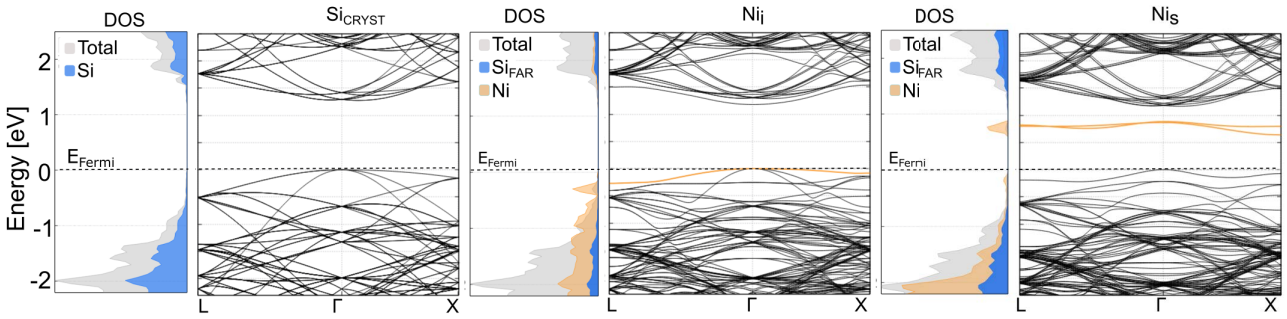

Figure 4.4: Band structure of crystalline silicon and defective structures containing Ni_i and Ni_simpurities.

4.2 Interstitial NiH_n complexes

The hypothesis proposed by [46] concerning interstitial metallic impurities bound to hydrogen atoms is investigated in this section, which examines the $Ni_i - H^q$ and $Ni_i - H_2$ complexes. To investigate the possible evolution of these complexes, the formation energies of metal-hydrogen and metal-hydrogen dissociated defects in crystalline silicon were studied. The term *"metal and hydrogen dissociated defects"* refers to structures in which the metal and hydrogen impurities are situated far apart from one another, thus preventing any electronic interaction between them, as illustrated in Figure 4.5(b). The average distance between nickel and hydrogen in our calculations was set to the maximum distance inside the supercell, which was approximately ~ 12Å. On the other hand, the term *"metal-hydrogen complex"* refers to a metal and one or several hydrogen atoms bonded to each other, as illustrates in figure 4.5 (a).

A comparison between the total energies of the dissociated impurities and the complexes inside crystalline silicon is presented in Table 4.3. We observed that the Ni-H complexes were more likely to form complexes rather than remaining as dissociated impurities. These energy differences indicate that nickel acts as a hydrogen "captor."

The stability of Ni-H complexes was analyzed by computing the formation energies which is given by:

$$E_{form}[Ni_i - H_n^q] = E_{TOT}[Si, Ni_i - H_n^q] - E_{TOT}[Crystal] - E_{atom}[Ni] - \frac{n}{2}E_{atom}[H_2] - q(\epsilon_{TVB} - \epsilon_F) + \Delta E_{elec} \tag{4.3}$$

In Equation 4.3 the coefficient n refers to the number of hydrogen atoms in the metal-hydrogen complex. For supercells of this size, the electrostatic correction was computed as $\Delta E_{elect} = -q^2 \times 0.118eV$, whereas the band alignment was $\Delta\epsilon^+_{TVB} = -0.054$ eV for $Ni_i - H^+$ and $\Delta\epsilon^-_{TVB} = -0.489$ eV for $Ni_i - H^-$. It is worth noting that calculations using the closed-shell approach resulted in the

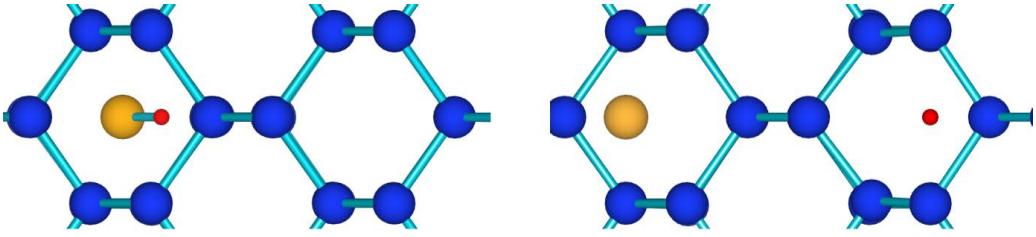

(a) Ni-H complex (b) Ni and H dissociated

Figure 4.5: Case of a metal hydrogen complex and a dissociated metal and hydrogen defects.

Complex	$E_{TOT}[dissociated] - E_{TOT}[complex]$ **[eV]**
$Ni_i + H^+$	0.291
$Ni_i + H^0$	1.014
$Ni_i + H^-$	0.455

Table 4.3: Energy differences between dissociated and complexes containing nickel and hydrogen inside crystalline silicon

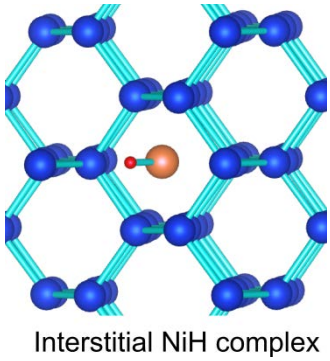

Figure 4.6: Defective structure of interstitial NiH in crystalline silicon

most stable configurations for the charged complexes. However, the complex $Ni_i - H^0$ is considered to have a spin $n_\alpha - n_\beta = 1$.

Figure 4.6 shows the position of the $Ni - H^q$ complex. The formation energy of each complex, along with the distance between nickel and hydrogen $d(Ni - H)$ and lattice parameter, are presented in Table 4.4. We observed that the $Ni_i - H^0$ complex presented the longest Ni-H interatomic distance. The increase in the lattice parameter of $Ni_i - H^-$ can be explained by the Coulombic repulsion between H^- and neighboring silicon atoms. Regarding the stability of the defects, the complex containing the positive charge state of hydrogen was the most stable, and as electrons were added to the complex, the formation energy of the complexes increased.

The case of $Ni - H_2$ structures was also studied. In order to obtain the most stable structure, three different configurations of the $Ni - H_2$ were considered, taking into account that the H_2 molecule exists in two different configurations in crystalline silicon. In Figure 4.7(a), the H_2 molecule was initially located at a tetrahedral interstitial site oriented along the [100] direction, while Figure 4.7(b) and Figure 4.7(c) consider the H_2^* structure around the nickel atom and one of the neighboring Si atoms, respectively.

For the $Ni - H_2$ complex, our calculations produced a bond length of 0.782Å, which is slightly longer than the bond length in free space reported to be 0.74Å [100], which is 0.002Å shorter than the bond length of the isolated H_2 molecule inside crystalline silicon, which was found to be 0.784Å. One of the hydrogen atoms was at a distance of 2.279Å while the other was at a distance of 3.056Å. The change in the positions of the nearest Si neighbors is negligible, as can be observed from the change in the lattice parameter.

In the $Ni_i + H_2^*$ structure with H_2^* around Si, the silicon atom was located asymmetrically between two hydrogen atoms, one at a distance of 1.832Å and the other at 1.5845Å. The nickel atom was located at a distance of 1.6862Å from the nearest hydrogen atom. This distance differs from the

Complex	E_{form} [eV]	$d_{(Ni,H)}$ [Å]	Lattice parameter$a$ [Å]	Δa [%]	**Lattice angles** [°]
$Ni_i + H^+$	-6.092	1.428	16.280	0.092	90.011
$Ni_i + H^0$	-5.820	1.518	16.303	0.049	89.989
$Ni_i + H^-$	-5.317	1.506	16.326	0.190	89.941

Table 4.4: Formation energies of different $Ni - H^q$ complexes, along with the structural deformation of the crystalline structure.

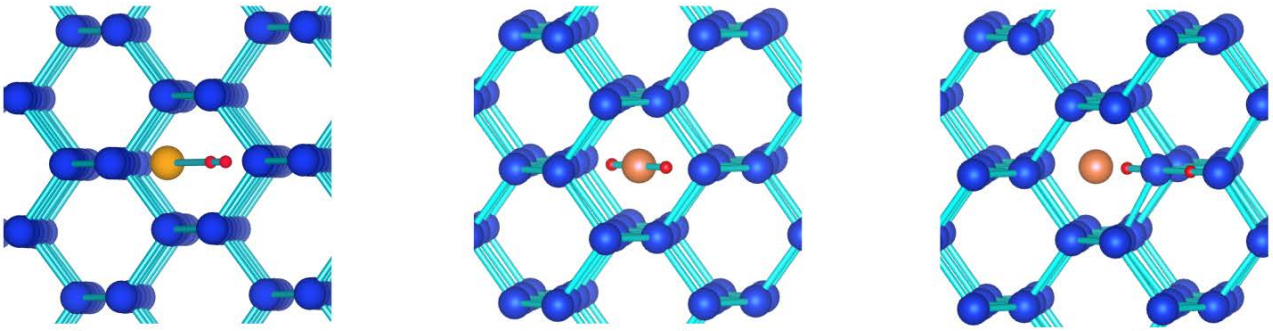

Figure 4.7: Defective structure of interstitial NiH_2 in crystalline silicon

Complex	E_{form} [eV]	Lattice parameter a [Å]	Δa [%]	**Lattice angles** [°]
$Ni_i + H_2$	-5.608	16.300	0.030	89.967
$Ni_i + H_2^*$ [Ni]	-5.680	16.308	0.079	90.077
$Ni_i + H_2^*$ [Si]	-5.231	16.313	0.110	90.050

Table 4.5: Formation energies of different $Ni - H^q$ complexes, along with the structural deformation of the crystalline structure for a supercell with 216 atoms.

case of the isolated H_2^* molecule, where we found that the position of the hydrogen in the BC is not symmetrical, as it is closer to one of the two nearest silicon atoms, lying at distances of 1.920Å and 1.547Å.

The formation energies and lattice parameters of the 216 Si atom supercell are presented in Table 4.5. We observe that the difference between $Ni - H_2$ and $Ni_i + H_2^*$ is $\sim 0.4eV$ which is similar to the energy difference between H_2 and H_2^* ($\sim$ 0.3 eV) in crystalline silicon. Among the three complexes, the most stable configuration corresponded to $Ni_i + H_2^*$ around the nickel atom.

4.2.1 Electronic structure of interstitial $Ni - H_n$ complexes

Figure 4.8 shows the band diagram and density of states for interstitial nickel-hydrogen complexes. Complexes $Ni_i - H_2$ and $Ni_i - H_2^*[Si]$ do not induce any energy level in the bandgap, but they in-

	ΔE_Γ **[eV]**	**Bandgap**	**Dielectric constant** ϵ
$Ni_i - H^+$	0.558	Direct	10.976
$Ni_i - H^0$	1.066	Indirect	10.990
$Ni_i - H^-$	0.658	Indirect	11.255
$Ni_i - H_2$	1.124	Indirect	10.948
$Ni_i - H_2^*$	0.877	Direct	10.959
$Ni_i - H_2^*[Si]$	1.084	Indirect	10.973
Si	1.171	Indirect	10.762

Table 4.6: Bandgap properties and dielectric constants of interstital $Ni_i - H_n$ complexes. ΔE_Γ refers to the energy difference at the Γ-point between the Fermi level and the first unoccupied energy level.

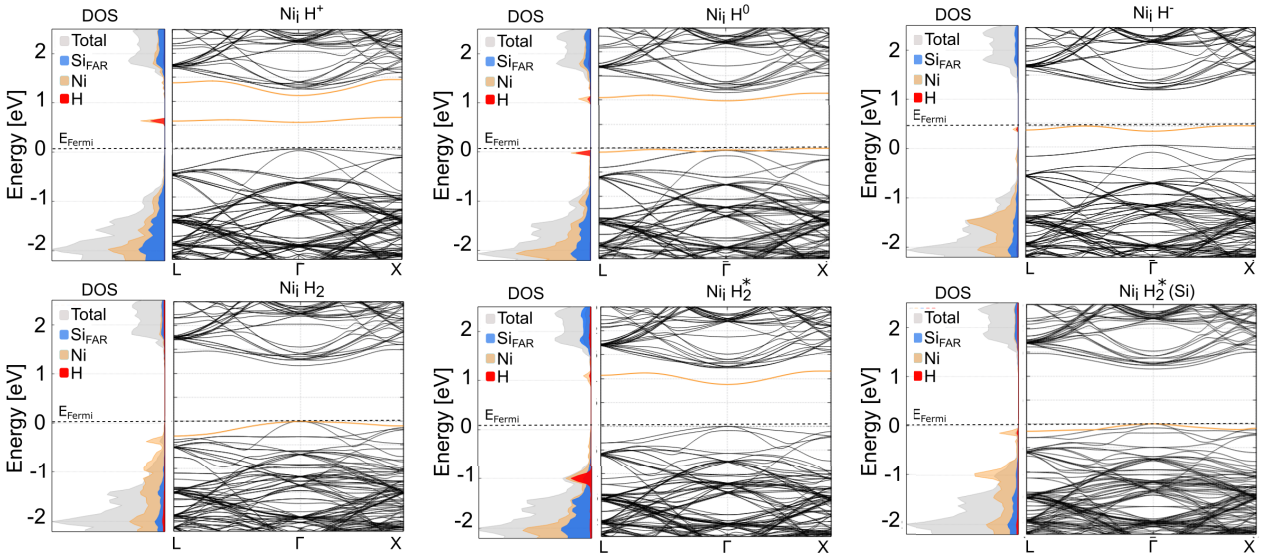

Figure 4.8: Band structure of defective structures containing $Ni - H^q$, $Ni - H_2$ and $Ni - H_2^*$ interstitial complexes.

duce an energy level at the top of the valence band. In contrast, $Ni_i - H_2^*$ induces an empty energy level 0.25 eV below the bottom of the conduction band. According to Table 4.6, the changes in the dielectric constants of $Ni_i - H_2$ and $Ni_i - H_2^*[Si]$ are similar, as they both leave the bandgap unchanged. For $Ni_i - H_2^*$, the presence of an additional level in the bandgap changes ΔE_Γ, inducing a change in the dielectric constant, which is only slightly higher than that of $Ni_i - H_2^*[Si]$, suggesting that neither of the complexes containing two hydrogen atoms act as recombination centers.

Regarding interstitial complexes that contain only one hydrogen atom, we observe that the $Ni_i - H^+$ and $Ni_i - H^-$ structures induce an energy level in the middle of the band gap at approximately the same position, ~ 0.6 eV, above the top of the valence band. For the complex $Ni_i - H^+$ this level is occupied, unlike the energy level induced by $Ni_i - H^+$. Both structures present an increase in the dielectric constant, which is more important for $Ni_i - H^+$ because of the change in the nature of the bandgap from indirect to direct. These two complexes may act as recombination centers.

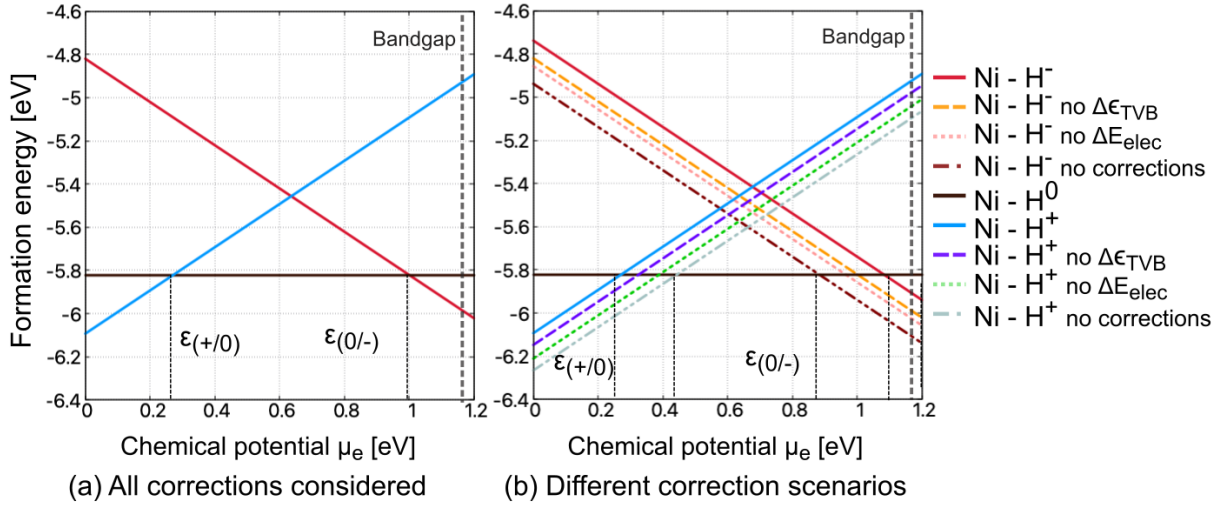

Figure 4.9: Formation energy as a function of the chemical potential for the interstitial $Co_i - H_n$ complexes.

The $Ni_i - H^0$ complex gives rise to two energy levels, one in the proximity of the valence band maximum and the other near the bottom of the conduction band. This complex does not appear to function as a recombination center.

The formation energies of the different charge states of the Ni_i complexes as functions of the chemical potential are presented in figure 4.9. The acceptor and donor levels were located 0.275 eV and 1 eV above the TVB, respectively. The donor level indicates the energy at which the transition of the positively charged state to the neutral state occurs. An analysis of the correction scheme used in this work shows that it impacts the position of the formation levels at 0.1 eV with respect to a study where no corrections were taken into account.

4.3 Substitutional $Ni - H_n$ complexes behavior

Few ab initio studies have been carried out to study the case of nickel- hydrogen complexes in crystalline silicon, in particular, they only address the case of nickel in a substitutional position [125] because these impurities have been explored in detail experimentally. In this section, we consider $Ni_s - H^q$ and $Ni_s - H_2$ complexes; however, the structure obtained for the complex $Ni_i - H^-$ is unlikely to be stable and therefore it is not included in this study.

The formation energies of metal-hydrogen and metal–hydrogen-dissociated defects in crystalline silicon were examined to investigate the potential evolution of these complexes. Our calculations show that $Ni_s - H^+$ presented an energy difference $E_{dissociated} - E_{complex}$ = 9.757 eV while it was 2.164 eV from $Ni_s - H^0$. Results suggest that nickel will act as a hydrogen "captor" in the substitutional position. It is observed that the energy difference $E_{dissociated} - E_{complex}$ is considerably higher for $Ni_s - H^q$ with respect to interstitial nickel.

The stability of $Ni_s - H^q$ complexes was analyzed by computing the formation energies which is given by:

$$E_{form}[Ni_s - H_n^q] = E_{TOT}[Si, Ni_s - H_n^q] - \frac{N-1}{N} E_{TOT}[Crystal] - E_{atom}[Ni] - \frac{n}{2} E_{atom}[H_2] - q(\epsilon_{TVB} - \epsilon_F) + \Delta E_{elec} \tag{4.4}$$

For a supercells with 216 Si atoms the electrostatic correction was evaluated as $\Delta E_{elect} = -q^2 \times 0.118eV$, whereas the band alignment was determined to be $\Delta\epsilon^+ TVB = -0.027$ eV for $Ni_s - H^+$.

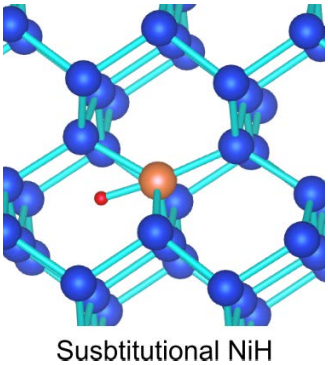

Figure 4.10: Defective structure of substitutional $Ni_s - H^q$ in crystalline silicon

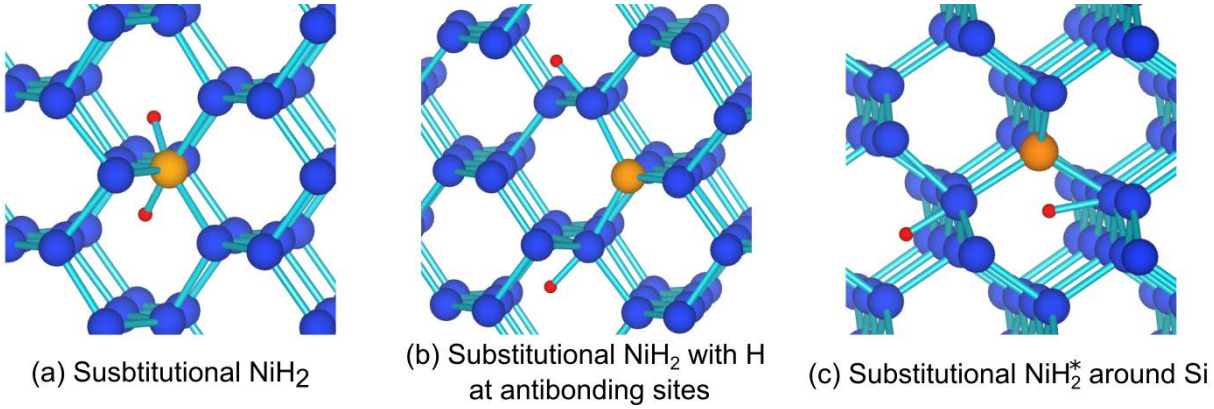

Figure 4.11: Defective structure of substitutional $Ni_s - H_2$ in crystalline silicon

Notably, the utilization of the closed-shell approach resulted in the most stable configurations of the charged complexes, whereas the complex $Ni_s - H^0$ was considered to have a spin $n_\alpha - n_\beta = 1$. Figure 4.10 shows the position of the $Ni_s - H^q$ complex. The formation energy of each complex, along with the lattice parameter is presented in Table 4.7. We determined that the distance between the Ni and hydrogen atoms was $d_{(Ni,H^+)} = 1.529$Å for the $Ni_s - H^+$ complex, which is approximately ~ 0.1 Å longer than that of interstitial nickel. The complex $Ni_s - H^0$ presents $d_{(Ni,H^0)} = 1.506$Å, which is approximately the same as that found for interstitial nickel$Ni_i - H^0$. The fact that $d_{(Ni,H^+)} > d_{(Ni,H^0)} = 1.506$ indicates that the additional electron shortes the $Ni - H^0$ bond owing to Coulombic attraction. Nevertheless, as shown in Table 4.7 there is a Coulombic repulsion between the hydrogen atoms and the surrounding Si atoms because the lattice parameter of $Ni_i - H^0$ is greater than that of $Ni_s - H^+$. This behavior was also observed for the interstitial $Ni_i - H^q$ complexes. The energy of the $Ni_s - H^q$ structures increases with the addition of electrons to the complex.

To study $Ni_s - H_2$ complexes, different $Ni_s - H_2$ configurations were considered to determine the most stable structure. The initial complex containing a H_2 molecule oriented toward [110] in a T_d position next to the nickel atom led to the same relaxed configuration as that of the H_2^* molecule around Ni_s, presented in Figure 4.11(a). In such a complex, the distance between the nickel and hydrogen atoms is $d_{(Ni,H)} = 1.500$Å for both hydrogen atoms. The change in the positions of the nearest Si neighbors was negligible, as can be seen from the lattice parameters in Table 4.7, which differs from the crystalline lattice parameter less than 0.1%.

Figure 4.11(c) shows the $Ni_s - H_2^*[Si]$ complex obtained after geometrical optimization of the H_2^*

Complex	E_{form} [eV]	Lattice parameter a [Å]	Δa [%]	**Lattice angles** [°]
$Ni_s - H^+$	-5.892	16.276	0.117	89.982
$Ni_s - H^0$	-5.611	16.286	0.055	89.958
$Ni_s - H_2$	-6.175	16.275	0.123	89.985
$Ni_s - H_2$ [AB]	-3.831	16.284	0.068	89.982
$Ni_s - H_2^*$ [Si]	-4.875	16.275	0.123	90.009

Table 4.7: Formation energies of different $Ni_s - H_n$ complexes, along with structural deformation of the crystalline structure for a supercell with 216 Si atoms.

structure around a neighboring Si atom. One H atom was initially positioned in the bound center between the Ni and Si atoms, and the other H atom was in the T_d position adjacent to the Si atom. After relaxation of the atomic positions, this structure leads to a configuration with two hydrogen atoms in the T_d position. The hydrogen atom furthest away from Ni is located at 1.570Å from the nearest Si atom. The other hydrogen atom is at a 1.715Å distance from the Si atom and 1.529Å from Ni. This distance differs from that of the isolated $Ni_i - H_2^*$ complex.

According to [125], two H atoms located at the antibonding (AB) sites of the nearest neighbors of nickel constitute the most stable configuration for the $Ni_s - H_2^*$ complex. The structure obtained for this configuration is illustrated in Fig. 4.11(b). We find that the distance between the Si and H atoms is 1.577Å and the distance between the hydrogen atoms is 6.451Å, which slightly differs from the distances obtained in [125], which are 1.557Å between the H and Si atoms and 7.3Å between the H atoms. In addition, calculations show that the structures $Ni_i - H_2$ and $Ni_i - H_2^*$ have formation energies 2.3 and 1.0 eV lower than that of $Ni_i - H_2$ [AB]. This difference with respect to [125], where a spin polarized LDA approach was used, can be explained by the used Hamiltonian.

4.3.1 Electronic structure of substitutional $Ni_s - H_n$ complexes

Figure 4.12 presents the band diagram and density of states of all the studied $Ni_s - H_n$ structures. We observe that the Ni_s impurity induces an energy level 0.63 eV above the top of the valence band and that this energy level remains at the same position for the $Ni_s - H^+$ and $Ni_s - H_2$ structures. In the case of $Ni_s - H^+$ this can be explained by the fact that this structure has no additional electrons with respect to the Ni_s impurity, and the system does not undergo a symmetry change, even when the atom positions are barely affected. This is similar to the case of $Ni_s - H_2$ which does not affect the symmetry of the Ni_s structure as in the case of the H_2 molecule in crystalline silicon.

For the $Ni_s - H^0$ complex, we observe that it induces an occupied energy level near the top of the valence band. This additional energy level slightly modifies the position of the energy level in-

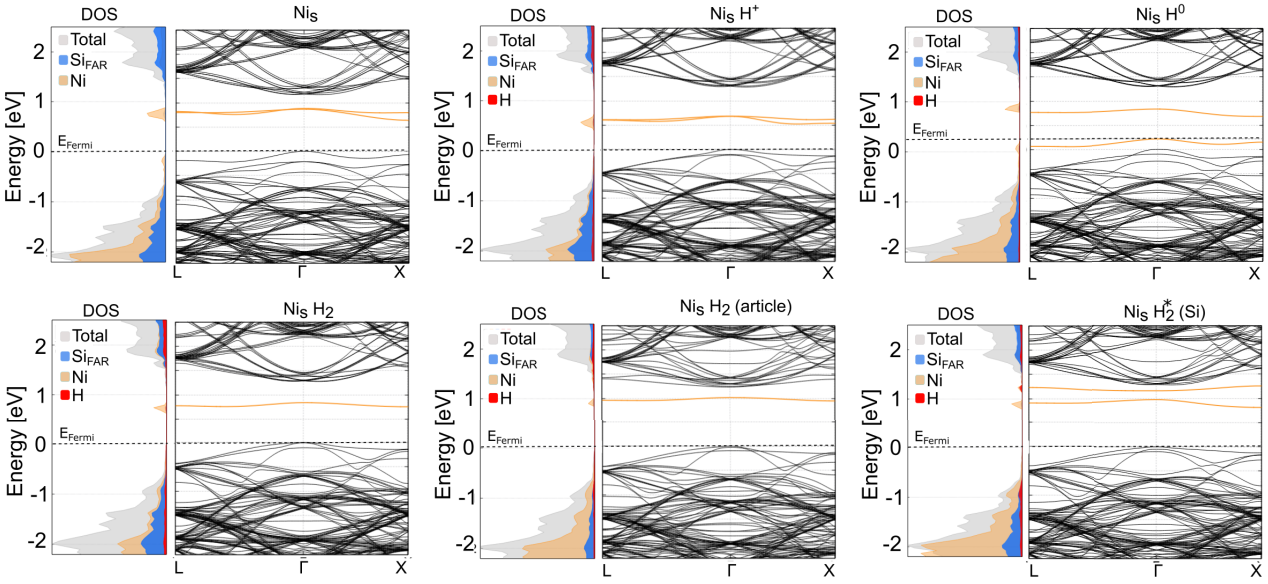

Figure 4.12: Band structure of defective structures containing $Ni_s - H^q$, $Ni_s - H_2$ and $Ni_s - H_2^*$ subsititutional complexes.

	ΔE_Γ **[eV]**	**Bandgap**	**Dielectric constant** ϵ
$Ni_s - H^+$	0.663	Indirect	12.062
$Ni_s - H^0$	0.602	Indirect	11.478
$Ni_s - H_2$	0.645	Indirect	11.230
$Ni_s - H_2$ [AB]	0.860	Indirect	11.243
$Ni_s - H_2^*$ [Si]	0.808	Indirect	11.225
Si	1.171	Indirect	10.762

Table 4.8: Electronic properties of substitutional nickel complexes. ΔE_Γ refers to the energy difference at the Γ-point between the Fermi level and the first unoccupied energy level.

duced by Ni_s. $Ni_i - H_2$ [AB] and $Ni_s - H_2^*$ [Si] increase the energy level induced by Ni_s to ~ 1 eV above the top of the valence band, which explains the higher formation energy of these structures with respect to $Ni_s - H_2$. Furthermore, $Ni_i - H_2^*$ [Si] induces an additional energy level approximately 0.18 eV lower than the bottom of the conduction band. The Fermi level of all substitutional $Ni_s - H_n$ structures is located at the top of the valence band.
Table 4.8 presents the energy difference ΔE_Γ and dielectric constant values of the Ni_s–H_n complexes. It is observed that the dielectric constant value increases as the energy difference ΔE_Γ decreases for all structures except $Ni_s - H^+$. This is because in the case of $Ni_s - H^+$ the Γ-point does not represent accurately the energy difference between the Fermi level and the first unoccupied state of the system. This minimin energy happens around the X-point, it has a value of 0.496 eV and determines the probability of trapping a charge carrier, increasing the value of the dielectric constant up to 12.06. According to the dielectric constant values, this structure, along with $Ni_s - H^0$ will be the most likely ones to act as recombination impurities.

4.4 Cobalt impurities in silicon

Among the transition metals in silicon, cobalt exhibits one of the highest diffusivities and solubilities, making it an impurity that can be easily incorporated into the majority of silicon wafers during thermal processing. Information regarding its energy levels and recombination activity is controversial because the electrical properties of cobalt in silicon remain poorly understood [127]. Both experimental and theoretical studies have been conducted on the issue of cobalt impurities in silicon [126]. Cobalt was found to be present in both n- and p-type silicon [180-185][127] which indicates that cobalt might have at least one donor and acceptor level in the bandgap. Nevertheless, it was found in [126], an ab initio study that used spin-polarized density functional calculations based on the SIESTA code, that interstitial cobalt exists only in silicon in a neutral charge state, whereas substitutional Co can be found in a stable position in neutral and negatively charged states. Investigations of the stability of various configurations, including interstitial and substitutional configurations, are required to understand the behavior of isolated cobalt in silicon and its interactions with other impurities.
Our study re-examines the properties of cobalt defects in the Co_i, Co_s and Co_s^- configurations., as only this cobalt structures have been reported to be stable in crystalline silicon [54]. The initial

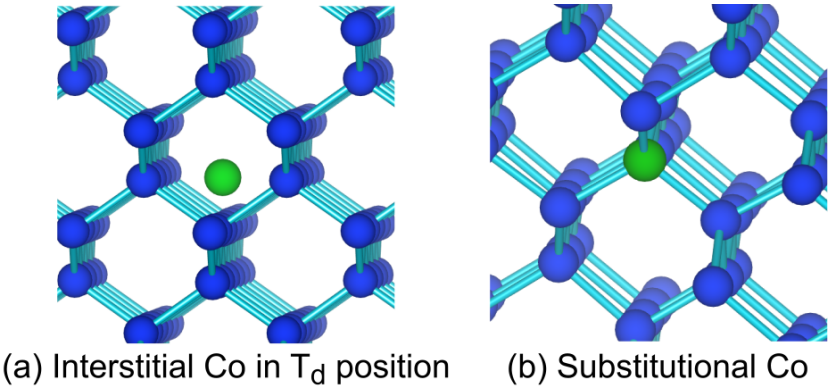

Figure 4.13: Defective structure of interstitial and substitutional cobalt in crystalline silicon

positions of each charge state were selected as the starting points prior to relaxation of the lattice and atomic positions. In the case of Co_i, it was situated in a T_d position were it would disturb the least the position of the host atoms. Co_s^q was located at the position of a crystalline Si in the supercell. The formation energy of a Co impurity in the interstitial position was computed as:

$$E_{form}[Co_i] = E_{TOT}[Si, Co_i] - E_{TOT}[Crystal] - E_{atom}[Co] \tag{4.5}$$

The equation that defines the formation energy for Co_s is equivalent to that of interstitial cobalt; however, it incorporates the term $\frac{N-1}{N} E_{TOT}[Crystal]$ which originates from the removal of one Si atom from the crystal:

$$E_{form}[Co_s^q] = E_{TOT}[Si, Co_s] - \frac{N-1}{N} E_{TOT}[Crystal] - E_{atom}[Co] - (\epsilon_{TVB}^q + \Delta\epsilon_{TVB}^q - \epsilon_F) + \Delta E_{elec} \tag{4.6}$$

In agreement with [126], convergence of the formation energy and bandgap values was achieved for substitutional and interstitial cobalt within supercells comprising 216 atoms. The total energies of different spin configurations were compared to determine the most stable energy for each charge state. It was found that Co_i is more stable with a total spin of 1, contrary to [126], who found that the most stable configuration has a spin $S = 3$, even though the total energy of the configuration with spin $S = 1$ is only 0.06 eV higher. This might be due to the use of a different Hamiltonian. In the case of substitutional Co, we find that the configuration Co_s with spin $S = 1$ has the lowest energy and that Co_s^- is more stable with a total spin $S = 2$, which is in agreement with [126]. The band aligment required a shift of $\epsilon_{TBV} = -0.089$ eV for Co_s^-.
Structures containing metallic impurities are shown in Figure 4.13. We observe that Co_i occupies a

	E_{form}	**Lattice parameter** a [Å]	Δa[%]	**Lattice angles** [°]
Co_i	-4.481	16.295	0.00	89.998
Co_s	-3.590	16.270	-0.15	89.976
Co_s^-	-2.789	16.283	-0.08	90.001

Table 4.9: Properties of cobalt impurities: relative formation energy, lattice parameter and percentage change of the lattice parameter with respect to the crystalline Si structure. Supercells contain 216 Si atoms.

T_d position and is located at a distance of 2.389Å from the nearest neighboring silicon atoms. This result is in good agreement with [126] where the calculated distance between Co_i and the nearest neighbors is 2.424Å. In the case of the substitutional cobalt impurity Co_s the distance with respect to its neighboring atoms is 2.227Å; therefore, we observe that the Si atoms are attracted to the Co atom. This attraction decreases in the case of Co_s^-, for which the distance to the nearest Si atom is 2.241Å. The distances we find are lower than those obtained in [126], where they found that Co_s is 2.245Å from the nearest neighbors and 2.383Å for Co_s^-.

From Table 4.17 we can see that the interstitial impurity Co_i is approximately 1 eV more stable than the substitutional configuration. This is found to be in agreement with [123], where it is suggested that transition metals originating from the silicon synthesis process occupy an interstitial position. We studied the interactions of Co_i with the silicon vacancy to observe whether it would be repositioned as a substitutional defect in the presence of a Si vacancy. After geometrical optimization, in which the atom positions are relaxed to minimize the entropy of the system, the cobalt atom does not relax into the substitutional position, as it stays next to the vacancy in the T_d position. The relaxed structure has a formation energy of −2.324 eV, which indicates that there is a potential barrier that the cobalt atom has to overcome to be located in a substitutional configuration, which is more stable. We also observed that the negative charge state Co_s^- has a higher formation energy than Co_s.

4.4.1 Electronic properties of cobalt impurities

The band diagram of the cobalt impurities is presented in figure 4.14. Contrary to interstitial nickel, the Co_i impurity induces an energy level at the top of the valence band and another 0.37 eV above, close to the middle of the bandgap. This increases the Fermi energy to 0.37 eV above TVB. The energy level in the middle of the bandgap originates from the unpaired electron in the electronic structure of Co_i and not from a geometric transition.

The presence of Co_s in the structure induces three energy levels in the bandgap: the first one is located 0.203 eV above the top of the valence band and coincides with the Fermi energy of the structure.; the second and third one are located 1.01 and 1.22 eV above the TVB.

The band structure of the Co_s^- impurity exhibits three energy levels within the bandgap. The first energy level is situated at a similar position as the energy level induced by Co_i, approximately 0.36 eV above the top of the valence band. The Fermi level of the structure coincides with the energy of this level. The second energy level, caused by this impurity, occurs at approximately 1.02 eV,

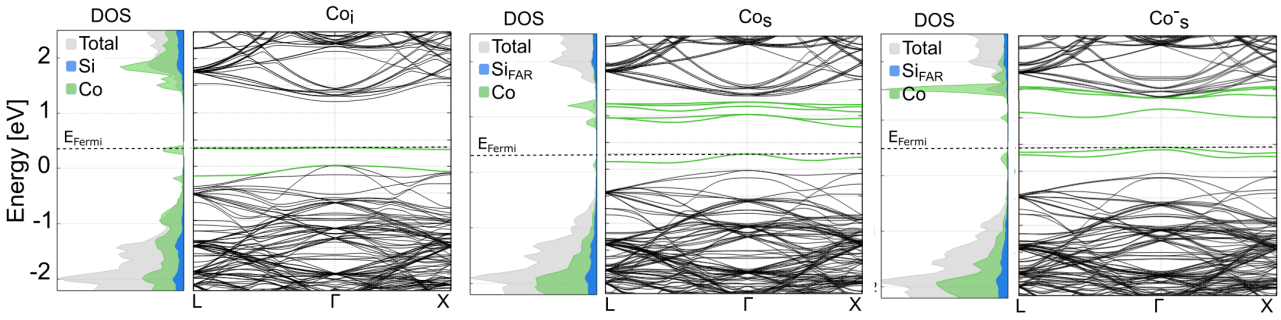

Figure 4.14: Band structure of cobalt impurities.

	ΔE_Γ **[eV]**	**Bandgap**	**Dielectric constant** ϵ
Co_i	0.754	Indirect	10.970
Co_s	0.501	Indirect	11.412
Co_s^-	0.572	Indirect	11.228
Si	1.171	Indirect	10.762

Table 4.10: Electronic properties of cobalt impurities.ΔE_Γ refers to the energy difference at the Γ-point between the Fermi level and the first unoccupied energy level.

which is in proximity to one of the energy levels produced by the neutral charge state of Co_s. The last energy level is located at the same level as the bottom of the conduction band. The crystal containing the Co_s impurity experiences an increase in both the bandgap value and the dielectric constant.

Table 4.10 shows that the dielectric constant increases as ΔE_Γ decreases for the Co impurities. The substitutional impurites Co_s and Co_s^- will be stronger recombination centers than Co_i. In addition, we found that Co_s has a transition level (acceptor level) at $\epsilon(0/-) = 0.58$ eV above the TVB. The different corrections in our approach lead to a shift of ±0.1 eV in the transition level positions. For regions with a chemical potential below $\epsilon(0/-)$ the neutral charge state will be the most stable among substitutional cobalt, while for regions above it, the negative charge state will be more likely to be present. The acceptor level reported in [126] is $\epsilon(0/-) = \epsilon_{BCB} - 0.44$ eV, which is 0.15 eV higher than our result. It is worth mentioning that the methodology used in [126] is based on the marker method with a perfect crystal as the universal marker for all defects. The assumptions of the marker method are already considered in our correction scheme; therefore, the difference between our results and [126] is purely due to the used Hamiltonian.

4.5 Interstitial $Co_i - H_n$ complexes behavior

To examine the theory that interstitial $Co_i - H_n$ complexes are responsible for LeTID, we investigate the stability and electronic characteristics of these impurities in the following. First, we analyze the energy variations of the structures containing cobalt-hydrogen complexes and dissociated Co and H. For the dissociated impurities, the distance between the cobalt and hydrogen atoms was set to the maximum possible separation inside the supercell, considering the periodic conditions, which is approximately 12 Å. The total energies of the structures containing Co-H complexes and dissociated impurities are compared in Table 4.11, confirming that the Co-H com-

Complex	$E_{TOT}[dissociated] - E_{TOT}[complex]$ **[eV]**
$Co_i + H^+$	0.680
$Co_i + H^0$	1.555
$Co_i + H^-$	0.767

Table 4.11: Energy differences between dissociated and complexes containing nickel and hydrogen inside crystalline silicon

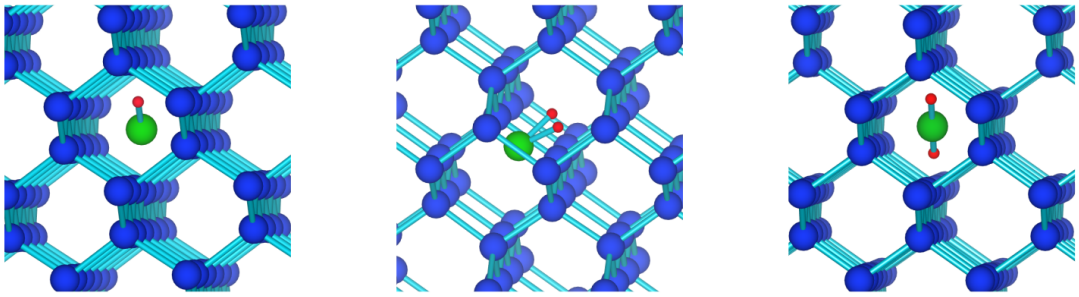

(a) Interstitial CoH (b) Interstitial CoH_2 (b) Interstitial CoH_2^*

Figure 4.15: Defective structure of interstitial $Co_i - H_n^q$ in crystalline silicon

plexes are more stable than the dissociated atoms. In [126], the energies required to bond H^+ and H^0 to Co_i, respectively, are around 0.51 and 0.37 eV, much lower than the results of Table 4.11.
Figure 4.15 shows the positions of the $Co_i - H_n^q$ complexes inside crystalline silicon. To obtain defective structures for the $Co_i - H_n^q$ complexes, the Co_i impurity was initially located in the T_d position, whereas the hydrogen atoms were located at the most stable position in crystalline silicon (BC for H^0 and H^+, and T_d for H^-). In the three cases the hydrogen atom left the BC position and move to a T_d position where it bonded to Co and the nearest Si atom. To obtain the most stable structures of the complex $Co_i - H_2$, the H_2 molecule was initially located at a tetrahedral interstitial site oriented along the [100] direction and we considered the initial structure of H_2^* around the cobalt atom. Both intial structures led to the configuration presented in 4.15(b). The case of H_2^* around one of the neighboring Si atoms led to an unstable configuration.
The stability of $Co_i - H_n^q$ complexes was analyzed by computing the formation energies which is given by:

$$E_{form}[Co_i - H_n^q] = E_{TOT}[Si, Co_i - H_n^q] - E_{TOT}[Crystal] - E_{atom}[Co] - \frac{n}{2}E_{atom}[H_2] - q(\epsilon_{TVB} - \epsilon_F) + \Delta E_{elec} \tag{4.7}$$

The formation energy of the interstitial complexes $Co_i - H_n^q$ was studied for supercells with 216 Si atoms. For the charge states, the electrostatic correction was calculated as $\Delta E_{elect} = -q^2 \times 0.118eV$, and the band alignment was $\Delta\epsilon^+ TVB = -0.075$ eV for $Co_i - H^+$ and $\Delta\epsilon^- TVB = -0.141$ eV for $Co_i - H^-$. The closed-shell approach was used to study $Co_i - H^0$, whereas $Co_i - H^+$, $Co_i - H^-$ and $Co_i - H_2$ were found to have a spin of $n_\alpha - n_\beta = 1$. Table 4.12 presents the formation energy, cobalt-hydrogen distance $d(Co-H)$, and lattice parameter of the defective structure for each complex.

Complex	E_{form} [eV]	$d_{(Co,H)}$ [Å]	Lattice parameter a [Å]	Δa [%]	**Lattice angles** [°]
$Co_i - H^+$	-4.514	1.435	16.2821	-0.081	89.967
$Co_i - H^0$	-4.118	1.436	16.301	0.034	89.981
$Co_i - H^-$	-2.749	1.510	16.323	0.170	90.002
$Co_i - H_2$	-3.510	1.545	16.309	0.083	89.986
$Co_i - H_2^*$ [Ni]	-3.622	1.482	16.310	0.089	89.956

Table 4.12: Formation energies of different $Ni - H^q$ complexes, along with structural deformation of the crystalline structure for supercells with 216 Si atoms.

The increase in the number of electrons in the complex $Co_i - H^q$ leads to an increase in both the distance $d_{(Co,H)}$ between the hydrogen and cobalt atom and the formation energy. The $Co_i + H_2$ and $Co_i + H_2^*$ complexes present a larger distance $d_{(Co,H)}$ than the $Co_i - H^q$ complexes. The complex $Co_i + H^-$ is found to be the least stable among these interstitial impurities.

The bond length $d_{(H,H)}$ in the $Co - H_2$ complex was calculated to be 0.907Å, which is longer than the bond length of the H_2 molecule in free space reported in [100] as 0.74Å, and longer than the bond length obtained for an isolated H_2 molecule in crystalline silicon (0.78Å). The interstitial impurities did not induce any geometry transition in any of the structures.

4.5.1 Electronic structure of interstitial $Co_i - H_n$ complexes

Figure 4.16 shows the band diagram and density of states for interstitial cobalt-hydrogen complexes. Regarding interstitial complexes that contain only one hydrogen atom, we observe that $Co_i - H^+$ forms two additional energy levels with respect to the Co_i impurity near to the bottom of the conduction band. Nevertheless, $Co_i - H^+$ has a Fermi level located at the top of the valence band, contrary to Co_i. The change in the dielectric constant is explained by the decrease in ΔE_Γ, indicating that $Co_i - H^+$ is a recombination center.

The addition of one electron to this complex leads to $Co_i - H^0$, which induces an energy level in the top of the valance band and another at the bottom of the conduction band. This complex does not induce any energy level in the bandgap due to the recombination of the $1s^1$ orbital with the cobalt orbitals. The change in ΔE_Γ and dielectric constant of this defect have a negligible change with respect to the crystalline silicon values.

The addition of an electron to $Co_i - H^0$ results in the formation of a $Co_i - H^-$ complex. The additional electron increases the Fermi level to 0.724 eV. This complex induces three energy levels located between the top of the valence band and the Fermi level of the structure. The addition of this extra electron increases the formation energy of the complex by ~ 1.3 eV, which could be evi-

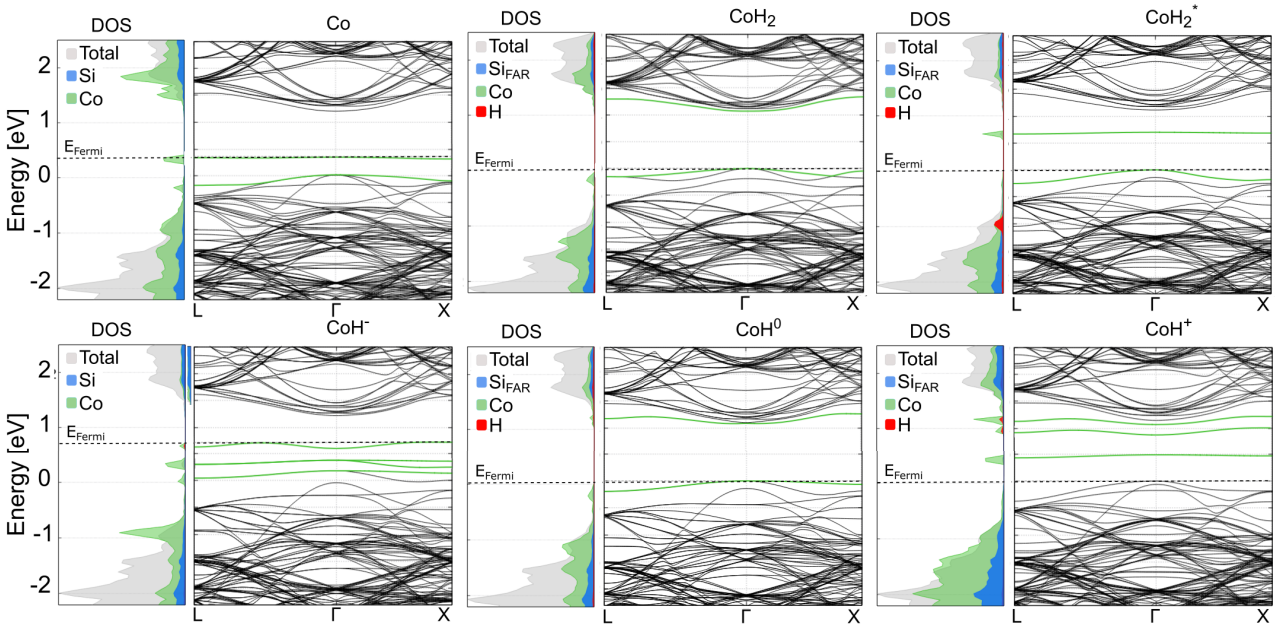

Figure 4.16: Band structure of interstitial $Co_i - H_n$ complexes.

	ΔE_Γ [eV]	Bandgap	Dielectric constant ϵ
$Co_i + H^+$	0.470	Indirect	11.228
$Co_i + H^0$	1.029	Indirect	10.955
$Co_i + H^-$	0.423	Indirect	11.412
$Co_i + H_2$	1.032	Indirect	10.970
$Co_i + H_2^*$ [Ni]	0.696	Indirect	11.068
Si	1.171	Indirect	10.762

Table 4.13: Opto-electronic properties of interstitial $Co_i - H_n^q$ impurities.ΔE_Γ refers to the energy difference at the Γ-point between the Fermi level and the first unoccupied energy level.

dence of the energy levels induced by $Co_i - H^0$ splitting and conforming to the $Co_i - H^-$ complex. The ΔE_Γ value decreases with an increase in the dielectric constant of the system.
The transition levels of the $Co_i - H^q$ complexes are found at $\epsilon(+/0) = 0.98eV$ and $\epsilon(0/-) = 1.094eV$ above the bandgap, according to our analysis of the formation energy as a function of the chemical potential (Figure 4.17.) The acceptor level reported in [126] was located at $\epsilon_{BCB} - 0.18$ eV. This value differs from ours by 0.1 eV. The correction scheme shows that the transition levels can be shifted by up to 0.2 eV according to the different correction scenarios.
The complexes $Co_i - H_2$ does not induce any energy level in the bandgap, but it induces an energy level right at the top of the valence band, and another at the bottom of the conduction band, which increases the value of the dielectric constant of the material, according to Table 4.13. On the other hand, the $Co_i - H_2^*$ induces an empty energy level 0.68 eV above the top of the valence band.

4.6 Substitutional $Co - H_n^q$ complexes behavior

To examine the behavior of substitutional $Co_s - H_n^q$ complexes inside crystalline silicon, we first focused on the stability of these impurities relative to the dissociated Co_s and H. Therefore, we eval-

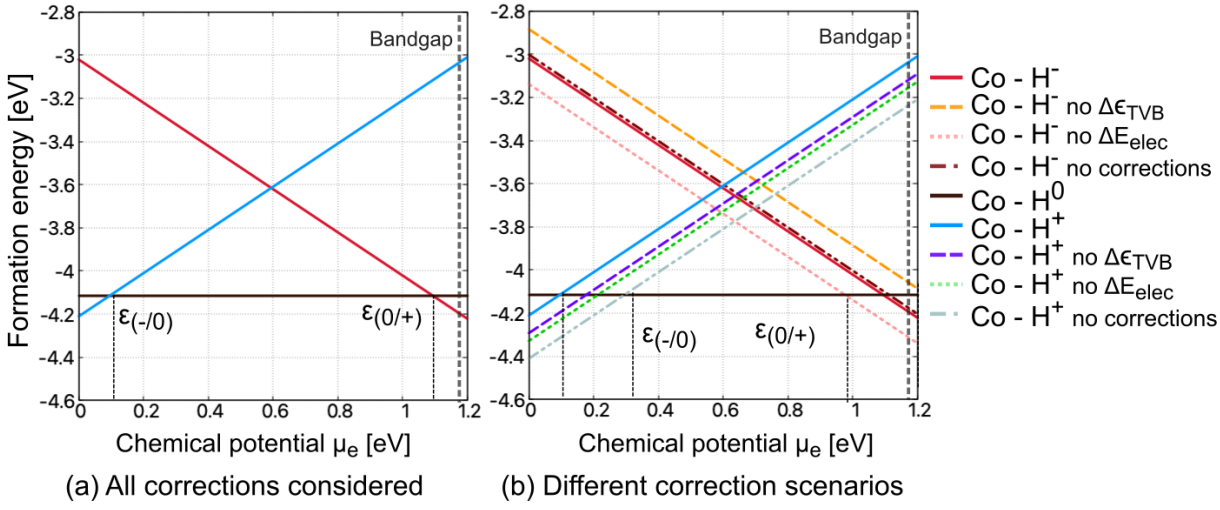

Figure 4.17: Formation energy as a function of the chemical potential for the interstitial $Co_i - H_n^q$ complexes.

uated the energy variations of the structures containing cobalt-hydrogen complexes and dissociated Co and H. The dissociated impurities were simulated with the distance between the cobalt and hydrogen atoms set to the maximum possible separation inside the supercell, accounting for periodic conditions. A comparison of the total energies of structures containing Co-H complexes and dissociated impurities is presented in Table 4.14, which confirms the greater stability of Co-H complexes compared to dissociated atoms. The substitutional complexes also exhibit energy differences with respect to the dissociated atoms, which are higher than the differences presented for the $Co_i - H_n$ impurities. This result is in agreement with [126], where the energies required to bond H^0 to Co_s is reported as 1.43 eV.

The positions of the $Co_s - H_n^q$ complexes inside crystalline silicon are presented in Figure 4.18. For the initial structure of $Co_s - H^q$, the Co_s impurity was placed in a susbtititutional position and the charged hydrogen atoms in the most stable position in the silicon lattice, respectively. The hydrogen atom located at a BC then moved from the BC position to a T_d position where it bonded to Co and the nearest Si atom. To obtain the most stable structure for the $Co_s - H_2$ complex, we placed the H_2 molecule at a tetrahedral interstitial site oriented along the [100] direction, and used the initial structure of H_2^* around the cobalt atom. The resulting structure is presented in Figure 4.18(b). However, the case of H_2^* around one of the neighboring Si atoms led to an unstable configuration.

According to [126], supercells with 216 Si atoms are big enough to analyze the properties of the complexes mentioned. The closed-shell approach was used to study $Co_i - H^0$, whereas $Co_i - H^+$, $Co_i - H^-$ and $Co_i - H_2$ were found to have a spin of $n_\alpha - n_\beta = 1$. The formation energies of $Co_s - H_n^q$ were computed as:

$$E_{form}[Co_s - H_n^q] = E_{TOT}[Si, Co_s - H_n^q] - \frac{N-1}{N} E_{TOT}[Crystal] - E_{atom}[Co] - \frac{n}{2} E_{atom}[H_2] - q(\epsilon_{TVB} - \epsilon_F) + \Delta E_{elec} \tag{4.8}$$

Complex	$E_{TOT}[dissociated] - E_{TOT}[complex]$ **[eV]**
$Co_s + H^+$	1.247
$Co_s + H^0$	1.354
$Co_s + H^-$	2.043

Table 4.14: Energy differences between dissociated and complexes containing substitutional cobalt and hydrogen.

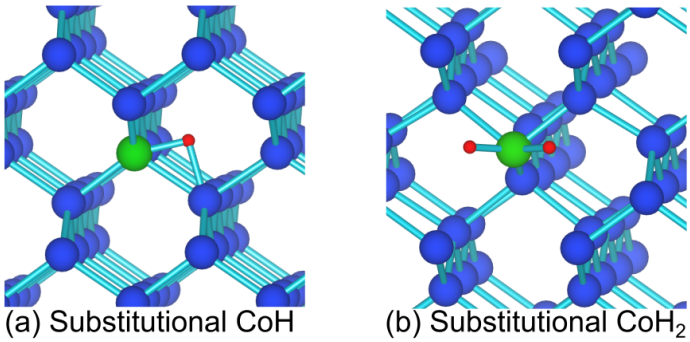

Figure 4.18: Defective structure of substitutional $Co_s - H$ in crystalline silicon

Complex	E_{form} [eV]	$d_{(Co,H)}$ [Å]	Lattice parameter a [Å]	Δa [%]	**Lattice angles** [°]
$Co_s + H^+$	-3.799	1.503	16.270	-0.156	89.969
$Co_s + H^0$	-3.502	1.519	16.282	-0.081	89.988
$Co_s + H^-$	-3.004	1.484	16.304	0.053	89.991
$Co_s + H_2$	-4.228	d_{H_1} =1.505	16.270	0.156	89.978
		d_{H_2} =1.479			

Table 4.15: Formation energies of different $Co_s - H_n^q$ complexes, along with structural deformation of the crystalline structure for a sueprcell with 216 Si atoms.

For the charge states, the electrostatic correction was calculated as $\Delta E_{elect} = -q^2 \times 0.118eV$, and the band alignment was $\Delta\epsilon^+ TVB = -0.109$ eV for $Co_s - H^+$ and $\Delta\epsilon^- TVB = -0.327$ eV for $Co_s - H^-$. Table 4.15 presents the formation energy, cobalt-hydrogen distance $d(Co_s - H)$, and lattice parameter of the defective structure for each complex.

The $Co_s - H_2$ complex has been found to be the most stable substitutional structure, with a formation energy that is 0.5 eV higher than that of $Co_s + H^+$, the most stable charge state of $Co_s + H^q$. Interestingly, this complex displays a slight asymmetry, with one of the hydrogen atoms positioned 0.03 Å further away from the Co_s atom than the other. The bond length $d_{(H,H)}$ in the $Co_s - H_2$ complex was calculated to be 0.907 Å, which is longer than the bond length of the H_2 molecule in free space reported in [100] as 0.74 Å, and longer than the bond length obtained for an isolated H_2 molecule in crystalline silicon (0.78 Å). The interstitial impurities did not induce any geometry transition in any of the structures. This complex induces the greatest change in the lattice parameter.

As electrons are added to the structure, the formation energy of $Co_s - H^q$ complexes increases. The distances $d_{(Co,H^+)}$ and $d_{(Co,H^0)}$ differ by 0.01Å. For H^+ and H^0, the hydrogen atom is positioned at 1.78 and 1.69Å from the closest Si atom, respectively. For the $Co_s + H^-$ structure we observe that the H^- approaches the cobalt atom and it is positioned further away from the nearest Si atom, at 2.92Å, which explains the increment in the lattice parameter with respect to $Co_s + H^+$ and $Co_s + H^0$.

4.6.1 Electronic structure of substitutional $Co_s - H_n^q$ complexes

Figure 4.19 shows the band diagram and density of states for the substitutional cobalt-hydrogen complexes. We observe that the $Co_s - H^+$ complex induces two energy levels located 0.878 eV

	ΔE_Γ	**Bandgap**	**Dielectric constant** ϵ
$Co_s - H^+$	0.867	Indirect	10.889
$Co_s - H^0$	0.350	Indirect	11.929
$Co_s - H^-$	0.805	Indirect	11.025
$Co_s - H_2$	0.691	Indirect	11.403
Si	1.171	Indirect	10.762

Table 4.16: Opto-electronic properties of substitutional $Co_s - H_n$ impurities.ΔE_Γ refers to the energy difference at the Γ-point between the Fermi level and the first unoccupied energy level.

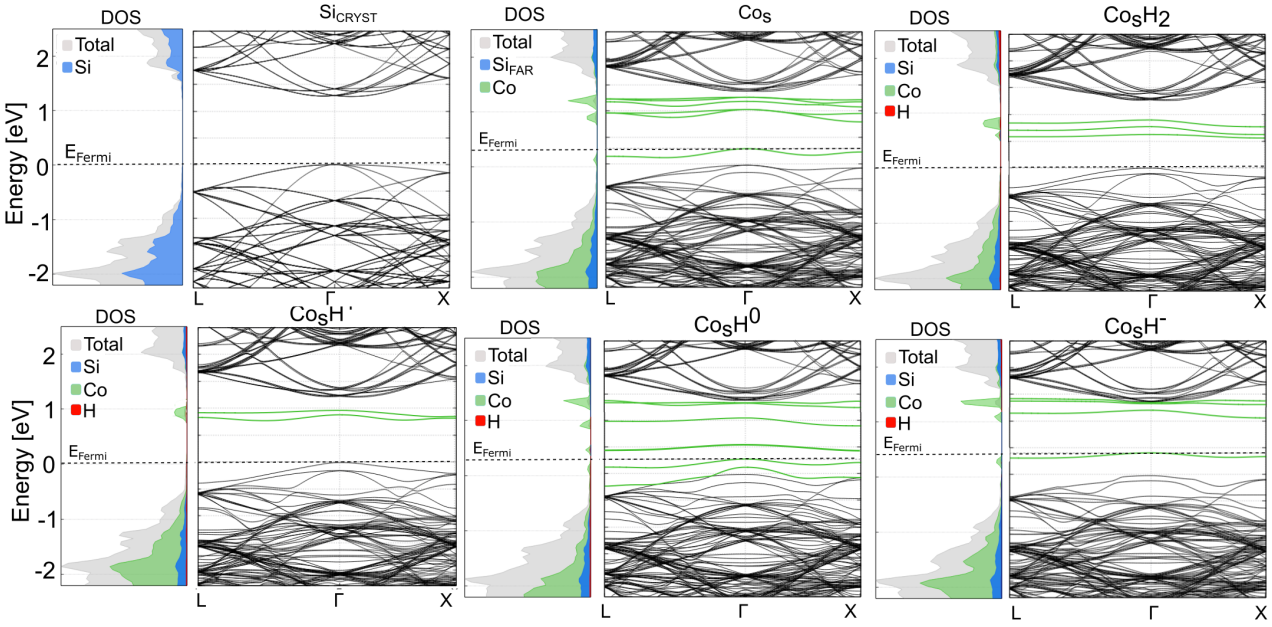

Figure 4.19: Band structure of substitutional $Co_s - H_n^q$ complexes in crystalline silicon.

above the top of the valence band. The values for ΔE_Γ and dielectric constant, presented in Table 4.16, indicate that the dielectric constant of this structure increases slightly compared to that of crystalline silicon. The addition of an electron to the complex generates $Co_s - H^0$, which induces several energy levels in the bandgap. The energy difference ΔE_Γ of the structure undergoes a significant decrease, which increases the dielectric constant of the system. The Fermi energies of both structures were positioned at the top of the valence band. The incorporation of an additional electron resulted in the formation of $Co_s - H^-$. This complex induces two energy levels near to the bottom of the conduction band and an energy level in the middle of the bandgap, which coincides with the Fermi energy of the system. It is observed that the $Co_i - H_2$ structure induces two energy levels in the middle of the bandgap, located 0.75 eV above the top of the valence band. The Fermi level of this structure was located at the top of the valence band. All of these complexes are likely to act as recombination centers.

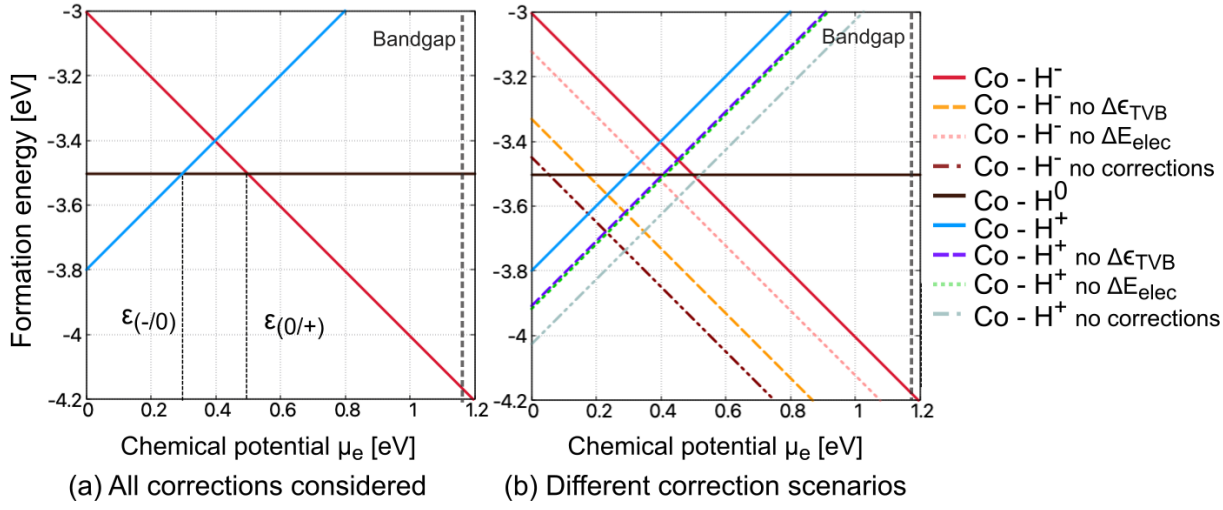

Figure 4.20: Formation energy as a function of the chemical potential for the substitutional$Co_s - H_n^q$ complexes.

Figure 4.20 shows the evolution of the formation energy as a function of the chemical potential for the $Co_s - H^q$ complexes. We found that these complexes have donor and acceptor levels located 0.297 and 0.499 eV above the top of the valence band, respectively. Figure 4.20 shows that all the different correction scenarios locate the acceptor level between the TVB and the middle of the bandgap. Nevertheless, experimental measurements have found that this complex has an acceptor level located at 0.29 eV below the bottom of the conduction band. This value differs from our results in 0.381 eV. In Ref. [126] a better result is obtained as it is found that this complex only has an acceptor level located at 0.42 eV below the bottom of the conduction band.

4.7 Dislocations

To estimate the impact of dislocations or grain boundaries in the presence of metallic impurities, we consider a simple case of studying the behavior of nickel and cobalt in dislocations. Dislocations are line defects or imperfections in the regular pattern of atoms in crystalline structures. They can play an important role in determining the properties of materials near the grain boundaries and interfaces.

Here, we study three cases of dislocations: a simple dislocation, the edge of such a dislocation, and twin grain boundary. A simple dislocation occurs when an extra half-plane of atoms is inserted between the two halves of a crystal, creating a mismatched region that extends along a line. The edge of this dislocation simulates the border of this additional plane. On the other hand, twin grain boundaries are formed by introducing a symmetry axis and performing a reflection of atomic positions with respect to it. Figure 4.21 schematically shows the three different simulated dislocations.

The length of the dislocation in each direction was set to at least 16.295Å, the length of a supercell containing 216 Si atoms, for which the formation energies and electronic properties of defective structures containing either Ni or Co converged. The final structures have 456 Si atoms for simple dislocations, as well as for edge dislocations and 528 atoms for the twin grain boundary. In order to simulate the case where a metallic impurity is trapped in a dislocation, we located the metallic impurity inside of the dislocation, as showen in Figure 4.21.

The formation energy of the metallic structures inside the dislocation is given by:

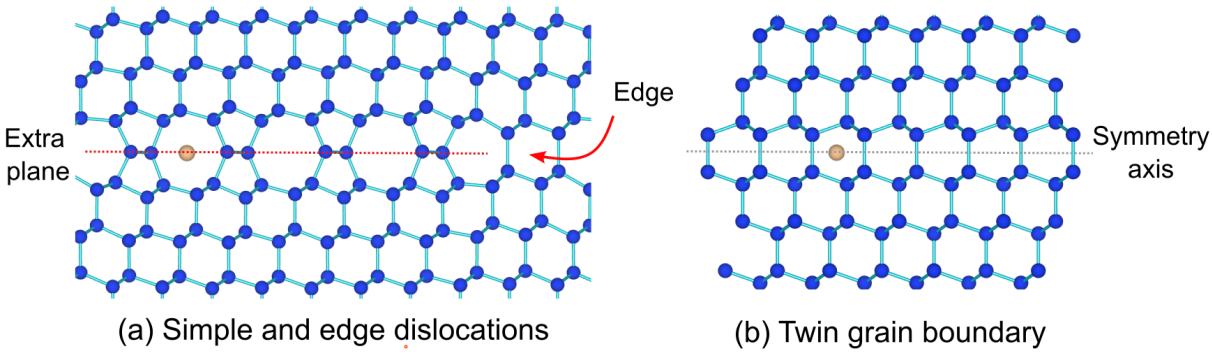

Figure 4.21: Dislocation structures.

Dislocation	Impurity	E_{form} **[eV]**
Simple	Ni_i	-6.681
	Co_i	-3.694
Edge	Ni_i	-6.782
	Co_i	-3.619
Twins	Ni_i	-6.691
	Co_i	-3.482

Table 4.17: Formation energies of metallic impurities inside dislocations

$$E_{form}[M_i] = E_{TOT}[Disloc, M_i] - E_{TOT}[Disloc] - E_{atom}[M] \tag{4.9}$$

Where $E_{TOT}[Disloc, M_i]$ refers to the total energy of the dislocation containing the metallic impurity in an interstitial position, $E_{TOT}[Disloc]$ refers to the total energy of the dislocation and $E_{atom}[M]$ to the energy of the metal atom. The calculations were performed in closed shell for Ni and with a spin $S = 1$ for Co.
The strong formation energies for each metallic impurity inside of each dislocation show that dislocations are likely to trap M_i, proving the hypothesis proposed where metallic impurities diffuse towards interfaces and the wafer's surface [46, 48].

4.8 Conclusions

Several simple models have been proposed to explain LeTID, all of which explain the degradation and recovery phases observed in solar cell performance. In this chapter, we seek to corroborate two models (shown in Figures 4.1 and 4.2) that propose metal-hydrogen complexes as the cause of LeTID [46, 123]. The stability and electronic properties of nickel, cobalt, and their complexes with hydrogen were studied. According to both models, defects in Phases 1 and 3 do not induce strong recombination or are unable to recombine, whereas defects in Phase 2 can recombine with charge carriers. Notably, the degradation phase in LeTID, which corresponds to Phase 2 in the metallic impurity model, is a transient state for recombination defects, implying that the defects in this phase are unstable and evolve into Phase 3 through regeneration. Therefore, defects that act as recombination points and are involved in LeTID must have higher formation energies than those in Phases 1 and 3.
In addition, these models suggest that metallic impurities occupy interstitial positions. However, there is a lack of experimental of evidence of the existence of interstitial Ni and Co[126], reason of which previous research has primarily focused on the study of such impurities in a substitutional positions. To compare the results of this study with available experimental and theoretical data and to test the hypothesis that Ni and Co occupy interstitial positions during LeTID, we investigated both metals in interstitial and substitutional positions.
To spot the metal-hydrogen impurities that can be in Phases 1, 2, or 3 and therefore deduce the dynamics of the impurities causing LeTID, three categories were defined regarding the recombination properties of the complexes. *Inactive to recombine* refers to defects that do not induce

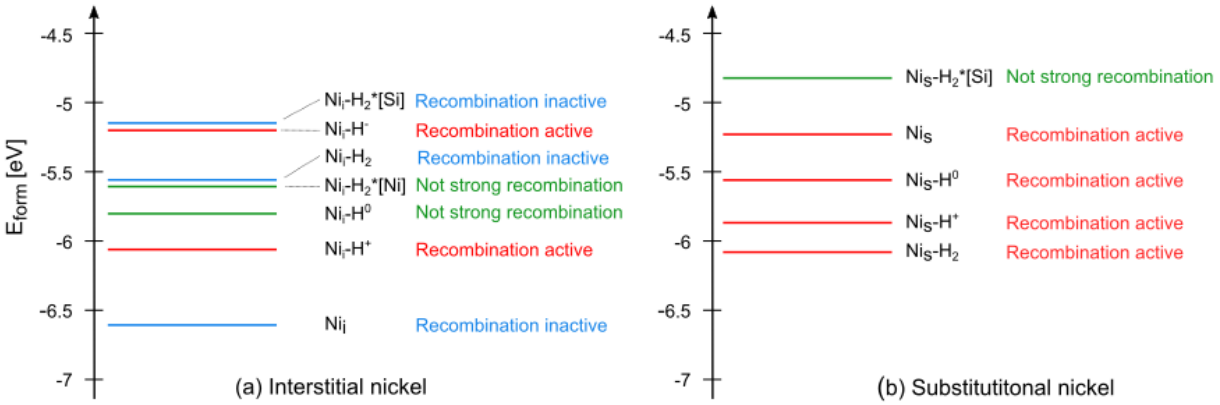

Figure 4.22: Stability and recombination results obtained for Ni.

energy levels in the bandgap; therefore, with $\Delta E_\Gamma > 0.9$ eV. *Not strong recombination* groups defects that induce energy levels near the bangap edges, so that they satisfy 0.7 eV $< \Delta E_\Gamma <$ 0.9 eV. *Recombination active* refers to defects induce energy levels near the middle of the bandgap and satisfy$\Delta E_\Gamma < 0.7$. Even if these recombination categories are defined in somewhat arbitrary ranges of ΔE_Γ, they are convenient to propose the evolution of impurities formation that follow the conditions of LeTID conditions.

The stability and recombination properties obtained for nickel are schematized in Figure 4.22, where the formation energies for each complex are presented along with the ability of the complex to recombine with charge carriers. We observed that among the impurities with interstitial nickel, some of them can react to follow LeTID dynamics. For example, if we consider Ni_i to be the initial recombination inactive defect (Phase 1), it can trap hydrogen and form $Ni_i - H^+$ (Phase 2), and later stabilize into Ni_i again. If we consider $Ni_i - H^0$, $Ni_i - H_2^*$ or $Ni_i - H_2$ as the initial defects in Phase 1, either of these defects can evolve towards $Ni_i - H^-$ during LeTID. The latter can stabilize into any of the recombination inactive or not strong recombination defects that have lower energy.

Substitutional Ni complexes do not respect the LeTID condition of having a defect unlikely to recombine with a formation energy lower than that of a defect that acts as a recombination center. LeTID could be caused by subsititutional nickel if there would be a defect involving Ni_s that is more stable than any of the recombination active Ni_s defects. The positions of the transition levels of Ni_s [124] suggest that the negatively charged state is stable for chemical potential values near the top of the conduction band. This case remains to be studied to discard (or not) Ni_s as a cause of LeTID.

The stability and recombination properties of Co are presented in Figure 4.23. These results show that even if the energy differences between the complexes and dissociated impurities are higher for Co_s, $Co_i - H_n$ complexes are more stable. Nevertheless, previous studies [126] suggested that the $Co_i - H$ pair might not be stable in crystalline silicon at room temperature. In addition, several differences in the transition levels of cobalt impurities between our results and [126] were observed. They might arise from the differences in the Hamiltonian used in each DFT approach. In [126] the marker method based on the properties of the crystalline structure is used. As discussed, this method is considered in our correction scheme and therefore do not represent a source of discrepancy between this work and [126].

Figure 4.23 shows that substitutional cobalt complexes do not behave as a defect involved in LeTID

because all the defects are likely to recombine with charge carriers. On the other hand, interstitial cobalt impurities can behave according to LeTID dynamics: $Co_i - H_2^*$ and $Co_i - H_2$ can be defects in Phase 1, each of these defects will transition to a defect able to recombine and with higher formation energy and Phase 3 can be achieved when any of these defects relaxes towards a defect unlikely to recombine with a lower energy.

These results indicate that interstitial Co and Ni were involved in LeTID. Nevertheless, in contrast to the model that propose metal-hydrogen complexes as the cause of LeTID [46, 123], hydrogen atoms attach to the initial defects to create recombination centers. The fact that the energy differences between the complexes and dissociated impurities were lower for interstitial impurities suggests that substitutional metals are more likely to trap hydrogen. This might indicate that a small fraction of LeTID occurs due to metal-hydrogen impurities. In addition, calculations corroborated that dislocations and grain boundaries trap metallic impurities; while there is no definitive, these results tentatively suggest that Phase 3 could correspond to the diffusion of the LeTID defect towards grain boundaries or interfaces.

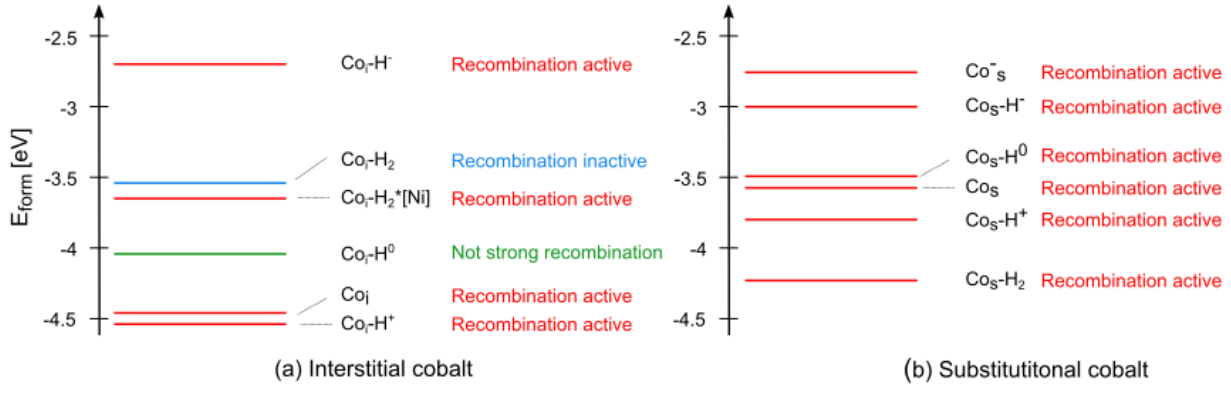

Figure 4.23: Stability and recombination results obtained for Co.

General conclusions and perspectives

At present, the root cause of the degradation and regeneration phases that characterize LeTID has not been determined. At present, it is believed that metal impurities and hydrogen are the key factors affecting LeTID[15, 30, 37, 43, 44, 45, 46]. An experimental study of the lifetime dependence on wafer thickness determined the diffusion coefficient of the impurity to be in the range of $(5 \pm 2) \times 10^{-11} cm^2 s^{-1}$ at a temperature of 75ºC [52]. The diffusion coefficients of hydrogen, cobalt, and nickel were found lay within the same range, indicating that these defects play a role in LeTID degradation.
Attempting to reduce LeTID, different strategies have been applied to reduce the amount of hydrogen or metallic impurities in silicon materials. By changing the thickness of the substrate, the thickness of the film, and the firing process, the hydrogen content in the solar cell can be altered to change the degradation degree of LeTID[37, 47]. Likewise, metallic impurities can be passivated to change the degree of LeTID degradation, using methods such as phosphorus gettering [46]. Nevertheless, LeTID has also been identified in high-purity silicon materials, indicating that it may be induced by intrinsic silicon defects including vacancies or self-interstitial silicon atoms. In either case, the role of hydrogen, metal impurities, and self-Si defects in LeTID has not been determined, and the study of LeTID by other non-metals has not been ruled out.
Simple models have been proposed to explain LeTID dynamics, which consider three main phases of degradation:

A. **Initial defect:** There are impurities in the bulk material in different stable states which are unable to recombine with the charge carriers. Once they are exposed to LeTID conditions, they will cause degradation.

B. **Degradation:** The initial stable impurities evolve toward defects that recombine with the charge carriers. This induces a decrease in the charge carrier lifetime. These defects are said to be in a metastable state as they evolve toward a recovered phase.

C. **Recovery:** Recombination defects are passivated until they reach final stable states.

Considering these LeTID features, the present study proposes a novel approach to identify possible precursors of LeTID using a DFT hybrid functional approach. The choice of crystalline silicon as a bulk material is based on various assumptions of a common defect causing LeTID in different silicon-based wafers [12, 16]. To simulate crystalline silicon, the hybrid functional $PBEsol_{12.5}$ was used because it properly reproduces the structural properties of silicon and its bandgap value.
This study focuses on the electronic properties and stability of hydrogen, self-silicon defects such as vacancies and interstitial Si atoms, and metal-hydrogen impurities containing nickel and cobalt.

The stability of such defects was analyzed by computing the defect formation energy. The electronic properties of the defective structures were analyzed by studying the band diagrams and dielectric constants of the defective structures.
Although several *ab initio* studies have addressed the problem of hydrogen, self-silicon defects, and metallic impurities in silicon, they present important inconsistencies among each others in the description given the use of different Hamiltonians and correction schemes (often not well justified) to compensate for the drawbacks of the DFT methodology. These parameters significantly affect in particular, the results concerning the relative stability of the defects. The approach used in this study considered a correction scheme based on two main corrections:

- **Band edge alignment:** The top of the valence band of the crystalline structure., $\epsilon_{TVB}[Si]$, was estimated to be $7.215eV$ with respect to vacuum. Then, the band edge positions of the defective structures were referenced to that of crystalline silicon by computing the difference between the outer core energy levels of each structures at the $\Gamma-$point.

- **Electrostatic correction:** It corrects the electrostatic interaction between the periodic charge distribution in supercells and the background. According to the Makov-Payne correction to the second order [82] it is given by $\Delta E_{elect} = -\frac{\alpha_m q^2}{2\epsilon L}$, where ϵ is the dielectric constant of the host material, $\alpha_m = 2.885$ is the Madelung constant for Si, and L is the lattice parameter of the studied supercell.

To propose a model for LeTID dynamics, silicon defects were classified into three configurations: defects in the initial state **A** and recovery phase **C** are stable and unable to recombine with charge carriers, whereas defects in the degradation phase **B** are in configurations with higher formation energies (i.e. less stable) than those in **A** and **C**, and can recombine with charge carriers.
Our results demonstrate that hydrogen-induced recombination is likely to occur in bulk silicon via the exchange of electrons between the different charge states of monoatomic hydrogen. In addition, H_2 and H_2^* are found to be more stable than H^0 and H^-, suggesting that configurations with H molecules constitute states **A** and **C** in our LeTID model, whereas H^0 represents a defect in state **B**. H^- does not recombine with charge carriers and therefore do no interact with hydrogen molecules during LeTID.
The study of monoatomic hydrogen atoms was found to be in good agreement with the experimental results on the structural and electronic properties of hydrogen impurities in silicon. Discrepancies were observed between our results and previous first-principles studies that investigated interstitial hydrogen defects in Si using an LDA Hamiltonian[48, 49]. We found a shift of the order of 0.5 eV in our results and those presented in [48, 49] for each transition level. We attribute these difference to the different Hamiltonians and corrections used in [48, 49] and our work. Indeed, these studies used an *a posteriori correction* to bring the bandgap in agreement with the experimental value. This correction consists of a rigid shift in the defect level together with the conduction bands. This procedure results in an inaccurate methodology that, rather than providing reliable and insight-fullx results, seeks to fit DFT energies to the experiments.
The results regarding self-silicon defects were found to be in good agreement with the experimental results. In particular, the positions of the transition levels of the different charge states of the

vacancy differe from the experimental values by approximately 0.1 eV. For interstitial silicon, no reliable experimental information was found regarding the positions of the transition levels. Several inconsistencies were observed in previous DFT studies that treat self silicon defects, in particular, those that use a correction scheme relying on experimental values, as published studies reference the DFT energies by the use of the so called "maker method"[106, 119]. In our case, the hypotheses of the marker method were already included in our correction scheme, without the need to reference any value to the experimental measurements.

Our results show that interstitial silicon and vacancies are likely to act as charge carrier traps depending on their charge states. A possible LeTID scenario concerning vacancies involves V^0 to be considered in states **A** and **C**, whereas V^- is attributed to state **B**. However, further research is necessary to examine the recombination ratio of the neutrally charged vacancies to validate this model. Considering that vacancies are likely to interact with other impurities within crystalline Si, they are more likely to form substitutional defects when interacting with impurities.

In the case of interstitial silicon atoms, the charge states Si^0 and Si^{++} can be classified as configurations in states **A** and **C**, respectively. From an analysis of the formation energy as a function of the chemical potential, we see that the charged defects Si^- and Si^+ are never the most stable defects for a given chemical potential value within the bandgap; therefore, we suggest that Si^{--} is attributed to state **B** (see Fig. 3.15).

Metal-hydrogen complexes in interstitial positions have been proposed as the cause of LeTID degradation in two different models, suggesting that interstitial metallic impurities bound to a different number of hydrogen atoms would constitute states **A, B** and **C** [46, 123]. To corroborate these models, the stability and electronic properties of Ni, Co, and their complexes with hydrogen were studied. To provide a thorough examination, we included an analysis of these structures in the substitutional positions.

Upon investigation of impurities containing nickel, it is suggested that substitutional Ni complexes do not respect the LeTID condition, where a configuration unlikely to recombine has a lower formation energy than any of the recombination-active configurations. However, some configurations containing interstitial nickel were observed to follow LeTID dynamics and are consistent with the proposed LeTId precursor phenomena. For instance, starting with Ni_i as the recombination inactive defect (state **A**), it can react with hydrogen to form $Ni_i - H^+$ (state **B**) and later revert to Ni_i after stabilization. Similarly, starting with $Ni_i - H^0$, $Ni_i - H_2^*$ or $Ni_i - H_2$ as the initial defects in state **A**, they can all evolve toward $Ni_i - H^-$ during LeTID. The $Ni_i - H^-$ defect can then stabilize into any of the recombination inactive or weak recombination defects with lower energy.

The stability and recombination properties of cobalt indicate that $Co_i - H_n$ complexes are more stable than Co_s complexes, even if the energy differences between the complexes and dissociated impurities are higher for Co_s. However, it is worth noting that previous studies [126] have suggested that the $Co_i - H$ pair may not be stable in crystalline silicon at room temperature. Additionally, several differences were observed in the transition levels of cobalt impurities between our results and [126], which may arise from differences in the Hamiltonian used in each DFT approach. Notably, in [126], a marker method based on the properties of the crystalline structure was used. However, this method is considered in our correction scheme and therefore does not represent a source of discrepancy between our work and [126].

Based on these results, it appears that substitutional cobalt complexes are not involved in LeTID because all of the defects are likely to recombine with charge carriers(i.e. they can only account for state **B** but not for **A** and **C**). However, interstitial cobalt impurities can behave according to the LeTID dynamics: $Co_i - H_2^*$ and $Co_i - H_2$ can be defects in state **A**. Each of these defects will transition to a defect that can recombine and has a higher formation energy, and state **C** can be achieved when any of these defects relax toward a defect that is unlikely to recombine and has lower energy.

These results suggest that LeTID involves interstitial Co and Ni. However, in contrast to the model proposing metal-hydrogen complexes as the cause of LeTID [46, 123], hydrogen atoms attach to the initial defects to create recombination centers. The energy differences between the complexes and dissociated impurities were lower for interstitial impurities, suggesting that substitutional metals were more likely to trap hydrogen.

According to [52], recombination-active impurities diffuse into the wafer surface during the regeneration phase. To investigate the potential diffusion of metal-hydrogen complexes toward grain boundaries, interfaces, or the wafer surface, this study was extended to consider three different types ofv dislocations: simple dislocations, dislocation edges, and twin-type grain boundaries. The calculations confirmed that dislocations and grain boundaries trapped metallic impurities. However, these results do not conclusively show that state **C** corresponds to LeTID defects trapped in these structures. Therefore, further investigations are required.

Our proposed configurations for states **A, B** and **C** allow us to propose reactions that cause LeTID degradation. Nevertheless, further investigation is required, such as calculating the probability of the reaction from states $A \rightarrow B$ and $B \rightarrow C$, which would provide more insights into the duration of the degradation and regeneration phases.

The relative stabilities and electronic properties obtained in this study were found to be consistent with the available experimental results, which ensured the reliability of the Hamiltonian and the used correction scheme. An analysis of this type using a correction scheme that does not fit the experimental data has not yet been reported for hydrogen and self-silicon defects. Differences with other ab initio studies indicate a promising direction toward the study of point defects in silicon using a pragmatic DFT Hybrid functional approach. Alternatively, the use of different correction schemes that do not rely on the marker method, as proposed in [128], remains to be explored.

Although the present study provides significant insights into the causes of LeTID aging, there are still several impurity configurations that require further investigation. The experimental results suggest that the defect responsible for LeTID may be a dangling bond in a silicon vacancy with H atoms in its vicinity and oxygen atoms [121]. The cases of structures containing hydrogen-interacting vacancies or interstitial silicon treated in works such as [99, 100] remain to be explored. Regarding metallic impurities, further investigation is necessary to study complexes containing three or four hydrogen atoms in metallic impurities, particularly those that involve nickel. It has been suggested experimentally that these complexes might be stable in crystalline Si [124]. The case of impurities containing gallium is also of great interest, as Ga-doped modules have recently shown a significant decrease in the extent of LeTID compared with other silicon-based modules.

To complement our results, a study using molecular dynamics (MD) would be useful to analyze the dynamic properties of the configurations involved in LeTID under thermal change.This would

allow for the analysis of the capture cross-section of each defect, which can provide valuable information regarding their impact as recombination centers. Computation of the thermal activation energies would result in a more detailed description of LeTID dynamics and would allow comparison to corroborate that the thermal activation energies of the impurities that we suggest are involved in LeTId lie in the range recently measured experimentally [129].

In conclusion, the results of this research suggest a promising DFT methodology to study the effect of point defects on LeTID degradation, a phenomenon that has been mainly studied experimentally, and proposes a physical model that explains the dynamics of LeTID. At the industrial level, such a model is useful for determining and optimizing mitigation processes. For example, even if the suppression of hydrogen impurities in the crystalline material would stop hydrogen induced recombination, it is not a realistic LeTID mitigation strategy for two reasons: first, hydrogen has a high mobility in silicon and it is very complicated to eliminate, and second, hydrogen is widely used to passivate deep-level defects, such as those caused by transition-metal impurities, and to saturate dangling bonds at surfaces, vacancies, and grain boundaries. The need for hydrogen in silicon materials is such that important increases in the lifetime of various types of silicon can be achieved by advanced hydrogenation methods that control the charge state of hydrogen and use it to passivate problematic defects [130]. Excess interstitial hydrogen can be harmful and cause Hydrogen-Induced Degradation (HID) in solar cells. Therefore, criteria regarding the measurement of hydrogen content and the amount of this impurity that is beneficial in the solar module must be determined.

Even though in the past years the extent of LeTID has been observed to decrease for certain materials that contain fewer impurities, the relationship between LeTID and current-induced degradation is unknown. This implies that, under operation conditions, it could be harmful if the module is exposed to a particular current.Therefore, understanding the physical causes of the degradation process is vital to eventually identify LeTID risk under specific ambient or working conditions and for a given module.

Finally, the adoption of such a model can give some insight in the identification of the optimal testing parameters, that seek to improve the efficacy of accelerated testing protocols. Indeed, accelerated tests use increased temperature, and a laser for illumination tens, if not hundreds, of times brighter than the sun as a way to test for LeTID on small samples in minutes rather than hundreds of hours [22]. Therefore, it is not clear up to which extent LeTID can be precisely reproduced using accelerated tests.

BIBLIOGRAPHY

[1] S. Mahajan, "Defects in semiconductors and their effects on devices," *Acta Materialia*, vol. 48, no. 1, pp. 137–149, 2000.

[2] M. A. El-Rashidy, "An efficient and portable solar cell defect detection system," *Neural Comput. Appl.*, vol. 34, p. 18497–18509, nov 2022.

[3] Energy, "In focus: Solar energy – harnessing the power of the sun," *European Comission*, 2022.

[4] P. Würfel, *Physics of Solar Cells: From Basic Principles to Advanced Concepts*. Physics textbook, Wiley, 2009.

[5] P. Basore, "Defining terms for crystalline silicon solar cells," *Progress in Photovoltaics: Research and Applications*, vol. 2, pp. 177–179, 1994.

[6] A. Ndiaye, A. Charki, A. Kobi, C. Kébé, P. Ndiaye, and V. Sambou, "Degradations of silicon photovoltaic modules: A literature review," *Solar Energy*, vol. 96, pp. 140–151, 10 2013.

[7] D. Bredemeier, D. Walter, S. Herlufsen, and J. Schmidt, "Lifetime degradation and regeneration in multicrystalline silicon under illumination at elevated temperature," *AIP Advances*, vol. 6, no. 3, p. 035119, 2016.

[8] Y. Yoshida and G. Langouche, *Defects and Impurities in Silicon Materials: An Introduction to Atomic-Level Silicon Engineering*. Lecture Notes in Physics, Springer Japan, 2016.

[9] G. Coletti, P. C. P. Bronsveld, G. Hahn, W. Warta, D. Macdonald, B. Ceccaroli, K. Wambach, N. Le Quang, and J. M. Fernandez, "Impact of metal contamination in silicon solar cells," *Advanced Functional Materials*, vol. 21, no. 5, pp. 879–890, 2011.

[10] J. Mullins, S. Leonard, V. P. Markevich, I. D. Hawkins, P. Santos, J. Coutinho, A. G. Marinopoulos, J. D. Murphy, M. P. Halsall, and A. R. Peaker, "Recombination via transition metals in solar silicon: The significance of hydrogen–metal reactions and lattice sites of metal atoms," *physica status solidi (a)*, vol. 214, no. 7, p. 1700304, 2017.

[11] A. Cuevas and D. Macdonald, "Measuring and interpreting the lifetime of silicon wafers," *Solar Energy*, vol. 76, no. 1, pp. 255–262, 2004. Solar World Congress 2001.

[12] L. Ning, L. Song, and J. Zhang, "Research progress of light and elevated temperature-induced degradation in silicon solar cells: A review," *Journal of Alloys and Compounds*, vol. 912, p. 165120, 2022.

[13] D. Lausch and C. Hagendorf, "Influence of different types of recombination active defects on the integral electrical properties of multicrystalline silicon solar cells," *Journal of solar Energy*, vol. 2015, p. 159584, Mar 2015.

[14] T. Trupke, B. Mitchell, J. Weber, W. McMillan, R. Bardos, and R. Kroeze, "Photoluminescence imaging for photovoltaic applications," *Energy Procedia*, vol. 15, pp. 135–146, 2012. International Conference on Materials for Advanced Technologies 2011, Symposium O.

[15] A. Ciesla, S. Wenham, R. Chen, C. Chan, D. Chen, B. Hallam, D. Payne, T. Fung, M. Kim, S. Liu, S. Wang, K. Kim, A. Samadi, C. Sen, C. Vargas Castrillon, U. Varshney, B. Vicari Stefani, P. Hamer, G. Bourret-Sicotte, and M. Abbott, "Hydrogen-induced degradation," pp. 0001–0008, 06 2018.

[16] D. Chen, M. Vaqueiro Contreras, A. Ciesla, P. Hamer, B. Hallam, M. Abbott, and C. Chan, "Progress in the understanding of light- and elevated temperature-induced degradation in silicon solar cells: A review," *Progress in Photovoltaics: Research and Applications*, pp. 1–22, 2020.

[17] K. Ramspeck, S. Zimmermann, H. Nagel, A. Metz, Y. Gassenbauer, B. Birkmann, and A. Seidi, "Light induced degradation of rear passivated mc-si solar cells," *Proc. 27th Eur. Photovolt. Sol. Energy Conf.*, vol. 2DO.3.4, p. 861–865, 2012.

[18] F. K. M. B. F. F. B. K. J. M. K. Petter, K. Hubener, "Dependence of letid on brick height for different wafer suppliers with several resistivities and dopants," *Proceedings of the 9th Int. Work. Cryst. Silicon Sol. Cells*, p. 1–17, 2016.

[19] B. Hallam, S. Wenham, P. Hamer, M. Abbott, A. Sugianto, C. Chan, A. Ciesla, M. Eadie, and G. Xu, "Hydrogen passivation of b-o defects in czochralski silicon," *Energy Procedia*, vol. 38, pp. 561–570, 12 2013.

[20] J. Schmidt, A. G. Aberle, and R. Hezel, "Investigation of carrier lifetime instabilities in cz-grown silicon,"

[21] M. A. Jensen, A. E. Morishige, J. Hofstetter, D. B. Needleman, and T. Buonassisi, "Evolution of letid defects in p-type multicrystalline silicon during degradation and regeneration," *IEEE Journal of Photovoltaics*, vol. 7, no. 4, pp. 980–987, 2017.

[22] D. N. R. Payne, C. E. Chan, B. J. Hallam, B. Hoex, M. D. Abbott, S. R. Wenham, and D. M. Bagnall, "Acceleration and mitigation of carrier-induced degradation in p-type multi-crystalline silicon," *physica status solidi (RRL) – Rapid Research Letters*, vol. 10, no. 3, pp. 237–241, 2016.

[23] K. Krauß, A. A. Brand, F. Fertig, S. Rein, and J. Nekarda, "Fast regeneration processes to avoid light-induced degradation in multicrystalline silicon solar cells," *IEEE Journal of Photovoltaics*, vol. 6, no. 6, pp. 1427–1431, 2016.

[24] W. Kwapil, T. Niewelt, and M. Schubert, "Kinetics of carrier-induced degradation at elevated temperature in multicrystalline silicon solar cells," *Solar Energy Materials and Solar Cells*, vol. 173, 06 2017.

[25] D. Sperber, A. Herguth, and G. Hahn, "A 3-state defect model for light-induced degradation in boron-doped float-zone silicon," *physica status solidi (RRL) – Rapid Research Letters*, vol. 11, no. 3, p. 1600408, 2017.

[26] R. E. Pritchard, J. H. Tucker, R. C. Newman, and E. C. Lightowlers, "Hydrogen molecules in boron-doped crystalline silicon," *Semiconductor Science and Technology*, vol. 14, pp. 77–80, jan 1999.

[27] F. Kersten, P. Engelhart, H.-C. Ploigt, A. Stekolnikov, T. Lindner, F. Stenzel, M. Bartzsch, A. Szpeth, K. Petter, J. Heitmann, and J. W. Müller, "Degradation of multicrystalline silicon solar cells and modules after illumination at elevated temperature," *Solar Energy Materials and Solar Cells*, vol. 142, pp. 83–86, 2015. Proceedings of the 5th International Conference on Crystalline Silicon Photovoltaics (SiliconPV 2015).

[28] B. Hammann, J. Engelhardt, D. Sperber, A. Herguth, and G. Hahn, "Influencing light and elevated temperature induced degradation and surface-related degradation kinetics in float-zone silicon by varying the initial sample state," *IEEE Journal of Photovoltaics*, vol. 10, no. 1, pp. 85–93, 2020.

[29] M. A. Jensen, A. E. Morishige, S. Chakraborty, R. Sharma, H. C. Sio, C. Sun, B. Lai, V. Rose, A. Youssef, E. E. Looney, S. Wieghold, J. Poindexter, J.-P. Correa-Baena, D. Macdonald, J. B. Li, and T. Buonassisi, "Do grain boundaries matter? electrical and elemental identification at grain boundaries in letid-affected p-type multicrystalline silicon," in *2017 IEEE 44th Photovoltaic Specialist Conference (PVSC)*, pp. 3300–3303, 2017.

[30] T. Niewelt, F. Schindler, W. Kwapil, R. Eberle, J. Schön, and M. C. Schubert, "Understanding the light-induced degradation at elevated temperatures: Similarities between multicrystalline and floatzone p-type silicon," *Progress in Photovoltaics: Research and Applications*, vol. 26, no. 8, pp. 533–542, 2018.

[31] T. Niewelt, R. Post, F. Schindler, W. Kwapil, and M. C. Schubert, "Investigation of letid where we can control it – application of fz silicon for defect studies," *AIP Conference Proceedings*, vol. 2147, no. 1, p. 140006, 2019.

[32] M. Selinger, W. Kwapil, F. Schindler, K. Krauß, F. Fertig, B. Michl, W. Warta, and M. C. Schubert, "Spatially resolved analysis of light induced degradation of multicrystalline perc solar cells," *Energy Procedia*, vol. 92, pp. 867–872, 2016. Proceedings of the 6th International Conference on Crystalline Silicon Photovoltaics (SiliconPV 2016).

[33] T. Niewelt, M. Selinger, N. E. Grant, W. Kwapil, J. D. Murphy, and M. C. Schubert, "Light-induced activation and deactivation of bulk defects in boron-doped float-zone silicon," *Journal of Applied Physics*, vol. 121, no. 18, p. 185702, 2017.

[34] T. Luka, S. Großer, C. Hagendorf, K. Ramspeck, and M. Turek, "Intra-grain versus grain boundary degradation due to illumination and annealing behavior of multi-crystalline solar cells," *Solar Energy Materials and Solar Cells*, vol. 158, pp. 43–49, 2016. Proceedings of the 6th International Conference on Silicon Photovoltaics.

[35] J. W. Teimuraz Mchedlidze, "Location and properties of carrier traps in mc-si solar cells subjected to degradation at elevated temperatures," *Applications and Materials Science*, vol. 216 (17), p. 1900142, 2019.

[36] C. E. Chan, D. N. R. Payne, B. J. Hallam, M. D. Abbott, T. H. Fung, A. M. Wenham, B. S. Tjahjono, and S. R. Wenham, "Rapid stabilization of high-performance multicrystalline p-type silicon perc cells," *IEEE Journal of Photovoltaics*, vol. 6, no. 6, pp. 1473–1479, 2016.

[37] H. C. Sio, D. Kang, X. Zhang, J. Yang, J. Jin, and D. Macdonald, "The role of dark annealing in light and elevated temperature induced degradation in p-type mono-like silicon," *IEEE Journal of Photovoltaics*, vol. 10, no. 4, pp. 992–1000, 2020.

[38] R. Eberle, W. Kwapil, F. Schindler, M. Schubert, and S. Glunz, "Impact of the firing temperature profile on light induced degradation of multicrystalline silicon," *physica status solidi (RRL) – Rapid Research Letters*, vol. 10, pp. n/a–n/a, 10 2016.

[39] H. C. Sio, H. Wang, Q. Wang, C. Sun, W. Chen, H. Jin, and D. Macdonald, "Light and elevated temperature induced degradation in p-type and n-type cast-grown multicrystalline and mono-like silicon," *Solar Energy Materials and Solar Cells*, vol. 182, pp. 98–104, 08 2018.

[40] F. Kersten, I. Förster, and S. Peters, "Evaluation of spatial ald of al2o3 for rear surface passivation of mc-si perc solar cells," 06 2016.

[41] "Carrier-induced degradation in multicrystalline silicon: dependence on the silicon nitride passivation layer and hydrogen released during firing," *IEEE Journal of Photovoltaics*, vol. 8, no. 2, pp. 413–420, 2018.

[42] D. Sperber, F. Furtwängler, A. Herguth, and G. Hahn, "Does letid occur in c-si even without a firing step?," *AIP Conference Proceedings*, vol. 2147, no. 1, p. 140011, 2019.

[43] A. Zuschlag, D. Skorka, and G. Hahn, "Degradation and regeneration in mc-si after different gettering steps," *Progress in Photovoltaics: Research and Applications*, vol. 25, no. 7, pp. 545–552, 2017.

[44] M. A. Jensen, A. Zuschlag, S. Wieghold, D. Skorka, A. E. Morishige, G. Hahn, and T. Buonassisi, "Evaluating root cause: The distinct roles of hydrogen and firing in activating light- and elevated temperature-induced degradation," *Journal of Applied Physics*, vol. 124, no. 8, p. 085701, 2018.

[45] T. H. Fung, M. Kim, D. Chen, A. Samadi, C. E. Chan, B. J. Hallam, S. Wenham, and M. Abbott, "Influence of bound hydrogen states on carrier-induced degradation in multi-crystalline silicon," *AIP Conference Proceedings*, vol. 1999, no. 1, p. 130004, 2018.

[46] J. Schmidt, D. Bredemeier, and D. C. Walter, "On the defect physics behind light and elevated temperature-induced degradation (letid) of multicrystalline silicon solar cells," *IEEE Journal of Photovoltaics*, vol. 9, no. 6, pp. 1497–1503, 2019.

[47] C. E. Chan, D. N. R. Payne, B. J. Hallam, M. D. Abbott, T. H. Fung, A. M. Wenham, B. S. Tjahjono, and S. R. Wenham, "Rapid stabilization of high-performance multicrystalline p-type silicon perc cells," *IEEE Journal of Photovoltaics*, vol. 6, no. 6, pp. 1473–1479, 2016.

[48] C. G. Van de Walle, P. J. H. Denteneer, Y. Bar-Yam, and S. T. Pantelides, "Theory of hydrogen diffusion and reactions in crystalline silicon," *Phys. Rev. B*, vol. 39, pp. 10791–10808, May 1989.

[49] C. Herring, N. M. Johnson, and C. G. Van de Walle, "Energy levels of isolated interstitial hydrogen in silicon," *Phys. Rev. B*, vol. 64, p. 125209, Sep 2001.

[50] N. E. Grant, J. R. Scowcroft, A. I. Pointon, M. Al-Amin, P. P. Altermatt, and J. D. Murphy, "Lifetime instabilities in gallium doped monocrystalline perc silicon solar cells," *Solar Energy Materials and Solar Cells*, vol. 206, p. 110299, 2020.

[51] D. Lin, Z. Hu, L. Song, D. Yang, and X. Yu, "Investigation on the light and elevated temperature induced degradation of gallium-doped cz-si," *Solar Energy*, vol. 225, pp. 407–411, 2021.

[52] D. Bredemeier, D. C. Walter, and J. Schmidt, "Possible candidates for impurities in mc-si wafers responsible for light-induced lifetime degradation and regeneration," *Solar RRL*, vol. 2, no. 1, p. 1700159, 2018.

[53] K. Graff, *Metal Impurities in Silicon-Device Fabrication*, vol. 24. 01 2000.

[54] T. M. Gibbons, D. J. Backlund, and S. K. Estreicher, "Cobalt-related defects in silicon," *Journal of Applied Physics*, vol. 121, no. 4, p. 045704, 2017.

[55] A. E. Morishige, M. A. Jensen, D. B. Needleman, K. Nakayashiki, J. Hofstetter, T.-T. A. Li, and T. Buonassisi, "Lifetime spectroscopy investigation of light-induced degradation in p-type multicrystalline silicon perc," *IEEE Journal of Photovoltaics*, vol. 6, no. 6, pp. 1466–1472, 2016.

[56] K. Nakayashiki, J. Hofstetter, A. E. Morishige, T.-T. A. Li, D. B. Needleman, M. A. Jensen, and T. Buonassisi, "Engineering solutions and root-cause analysis for light-induced degradation in p-type multicrystalline silicon perc modules," *IEEE Journal of Photovoltaics*, vol. 6, no. 4, pp. 860–868, 2016.

[57] U. Varshney, M. Abbott, A. Ciesla, D. Chen, S. Liu, C. Sen, M. Kim, S. Wenham, B. Hoex, and C. Chan, "Evaluating the impact of sinx thickness on lifetime degradation in silicon," *IEEE Journal of Photovoltaics*, vol. 9, no. 3, pp. 601–607, 2019.

[58] D. Bredemeier, D. C. Walter, R. Heller, and J. Schmidt, "Impact of hydrogen-rich silicon nitride material properties on light-induced lifetime degradation in multicrystalline silicon," *physica status solidi (RRL) – Rapid Research Letters*, vol. 13, no. 8, p. 1900201, 2019.

[59] A. Zuschlag, D. Skorka, and G. Hahn, "Degradation and regeneration in mc-si after different gettering steps," *Progress in Photovoltaics: Research and Applications*, vol. 25, no. 7, pp. 545–552, 2017.

[60] C. Sen, C. Chan, P. Hamer, M. Wright, U. Varshney, S. Liu, D. Chen, A. Samadi, A. Ciesla, C. Chong, B. Hallam, and M. Abbott, "Annealing prior to contact firing: A potential new approach to suppress letid," *Solar Energy Materials and Solar Cells*, vol. 200, p. 109938, 2019.

[61] R. Sharma, A. P. Chong, J. B. Li, A. G. Aberle, and Y. Huang, "Role of post-metallization anneal sequence and forming gas anneal to mitigate light and elevated temperature induced degradation of multicrystalline silicon solar cells," *Solar Energy Materials and Solar Cells*, vol. 195, pp. 160–167, 2019.

[62] D. H. Q. W. Z. N. Y. L. L. S. Zehui Wang, Honglie Shen and H. Qian, "Influence of double current injection annealing on anti-lid effect in mono-like cast silicon perc solar cells," *Journal of Materials Science: Materials in Electronics*, vol. 31, pp. 3221–3227, 2020.

[63] C. F. G. F. Z.-D. I. I. K. D. K. Z.A. Ibrahim, A. Shkrebtii, "Characterization of hydrogen in c-si and a-si:h from ab-initio molecular dynamics: Structure, optics and vibrations," *29th European Photovoltaic Solar Energy Conference and Exhibition*, vol. 1BV.6.26, pp. 127 – 130, 2020.

[64] M. Born and R. Oppenheimer, "Zur quantentheorie der molekeln," *Annalen der Physik*, vol. 389, no. 20, pp. 457–484, 1927.

[65] V. I. Minkin, "Glossary of terms used in theoretical organic chemistry," *Pure and Applied Chemistry*, vol. 71, no. 10, pp. 1919–1981, 1999.

[66] J. C. Slater, "The theory of complex spectra," *Phys. Rev.*, vol. 34, pp. 1293–1322, Nov 1929.

[67] D. R. Hartree, "The wave mechanics of an atom with a non-coulomb central field. part i. theory and methods," *Mathematical Proceedings of the Cambridge Philosophical Society*, vol. 24, no. 1, p. 89–110, 1928.

[68] P. Hohenberg and W. Kohn, "Inhomogeneous electron gas," *Phys. Rev.*, vol. 136, pp. B864–B871, Nov 1964.

[69] W. Kohn and L. J. Sham, "Self-consistent equations including exchange and correlation effects," *Phys. Rev.*, vol. 140, pp. A1133–A1138, Nov 1965.

[70] J. P. Perdew, J. A. Chevary, S. H. Vosko, K. A. Jackson, M. R. Pederson, D. J. Singh, and C. Fiolhais, "Atoms, molecules, solids, and surfaces: Applications of the generalized gradient approximation for exchange and correlation," *Phys. Rev. B*, vol. 46, pp. 6671–6687, Sep 1992.

[71] J. P. Perdew, A. Ruzsinszky, G. I. Csonka, O. A. Vydrov, G. E. Scuseria, L. A. Constantin, X. Zhou, and K. Burke, "Restoring the density-gradient expansion for exchange in solids and surfaces," *Phys. Rev. Lett.*, vol. 100, p. 136406, Apr 2008.

[72] A. D. Becke, "A new mixing of hartree–fock and local density-functional theories," *The Journal of Chemical Physics*, vol. 98, no. 2, pp. 1372–1377, 1993.

[73] A. D. Becke, "A new mixing of hartree–fock and local density-functional theories," *The Journal of Chemical Physics*, vol. 98, no. 2, pp. 1372–1377, 1993.

[74] R. Dovesi, A. Erba, R. Orlando, C. M. Zicovich-Wilson, B. Civalleri, L. Maschio, M. Rérat, S. Casassa, J. Baima, S. Salustro, and B. Kirtman, "Quantum-mechanical condensed matter simulations with crystal," *WIREs Computational Molecular Science*, vol. 8, no. 4, p. e1360, 2018.

[75] E. Tiesinga, P. J. Mohr, D. B. Newell, and B. N. Taylor, "Codata recommended values of the fundamental physical constants: 2018," *Rev. Mod. Phys.*, vol. 93, p. 025010, Jun 2021.

[76] C. Kittel, *Introduction to Solid State Physics*. Wiley, 2004.

[77] F. Lafond, *Hybrid functionals approach for the study of the properties of complex materials for photovoltaic applications*. Theses, Université de Lorraine, Dec. 2019.

[78] V. N. Staroverov, G. E. Scuseria, J. Tao, and J. P. Perdew, "Tests of a ladder of density functionals for bulk solids and surfaces," *Phys. Rev. B*, vol. 69, p. 075102, Feb 2004.

[79] J. E. Ortega and F. J. Himpsel, "Inverse-photoemission study of ge(100), si(100), and gaas(100): Bulk bands and surface states," *Phys. Rev. B*, vol. 47, pp. 2130–2137, Jan 1993.

[80] D. Drabold and S. Estreicher, *Theory of Defects in Semiconductors*, vol. 104, pp. 1–10. 01 2006.

[81] R. Dovesi and R. Orlando, "Convergence properties of the supercell approach in the study of local defects in solids," *Phase Transitions*, vol. 52, no. 2-3, pp. 151–167, 1994.

[82] G. Makov and M. C. Payne, "Periodic boundary conditions in ab initio calculations," *Phys. Rev. B*, vol. 51, pp. 4014–4022, Feb 1995.

[83] T. Renner, *Quantities, Units and Symbols in Physical Chemistry*. The Royal Society of Chemistry, 2007.

[84] J. Endres, D. A. Egger, M. Kulbak, R. A. Kerner, L. Zhao, S. H. Silver, G. Hodes, B. P. Rand, D. Cahen, L. Kronik, and A. Kahn, "Valence and conduction band densities of states of metal halide perovskites: A combined experimental–theoretical study," *The Journal of Physical Chemistry Letters*, vol. 7, no. 14, pp. 2722–2729, 2016. PMID: 27364125.

[85] S. Lany and A. Zunger, "Accurate prediction of defect properties in density functional supercell calculations," *Modelling and Simulation in Materials Science and Engineering*, vol. 17, p. 084002, nov 2009.

[86] J. F. Janak, "Proof that $\frac{\partial e}{\partial n_i} = \epsilon$ in density-functional theory," *Phys. Rev. B*, vol. 18, pp. 7165–7168, Dec 1978.

[87] S. Sanna, T. Frauenheim, and U. Gerstmann, "Validity of the slater-janak transition-state model within the LDA + u approach," *Phys. Rev. B*, vol. 78, p. 085201, Aug 2008.

[88] C. G. Van de Walle and R. M. Martin, "Theoretical study of band offsets at semiconductor interfaces," *Phys. Rev. B*, vol. 35, pp. 8154–8165, May 1987.

[89] F. Kersten, P. Engelhart, H.-C. Ploigt, A. Stekolnikov, T. Lindner, F. Stenzel, M. Bartzsch, A. Szpeth, K. Petter, J. Heitmann, and J. W. Müller, "A new mc-si degradation effect called letid," in *2015 IEEE 42nd Photovoltaic Specialist Conference (PVSC)*, pp. 1–5, 2015.

[90] D. Sperber, A. Herguth, and G. Hahn, "Investigating possible causes of light induced degradation in boron-doped float-zone silicon," 09 2017.

[91] K. Kim, R. Chen, D. Chen, P. Hamer, A. Ciesla nee Wenham, S. Wenham, and Z. Hameiri, "Degradation of surface passivation and bulk in p-type monocrystalline silicon wafers at elevated temperature," *IEEE Journal of Photovoltaics*, vol. 9, no. 1, pp. 97–105, 2019.

[92] J. Fritz, A. Zuschlag, D. Skorka, A. Schmid, and G. Hahn, "Temperature dependent degradation and regeneration of differently doped mc-si materials," *Energy Procedia*, vol. 124, pp. 718–725, 09 2017.

[93] M. A. Roberson and S. K. Estreicher, "Vacancy and vacancy-hydrogen complexes in silicon," *Phys. Rev. B*, vol. 49, pp. 17040–17049, Jun 1994.

[94] W. Jost, J. Weber, and H. Lemke, "Hydrogen - cobalt complexes in p-type silicon," *Semiconductor Science and Technology*, vol. 11, p. 525, apr 1996.

[95] N. Nickel, G. Anderson, and J. Walker, "Hydrogen-induced platelets in disordered silicon," *Solid State Communications*, vol. 99, no. 6, pp. 427–431, 1996.

[96] R. Hull and I. I. service), *Properties of Crystalline Silicon*. EMIS datareviews series, INSPEC, the Institution of Electrical Engineers, 1999.

[97] K. Sueoka, E. Kamiyama, P. Śpiewak, and J. Vanhellemont, "Review—properties of intrinsic point defects in si and ge assessed by density functional theory," *ECS Journal of Solid State Science and Technology*, vol. 5, p. P3176, feb 2016.

[98] J. A. Stewart, N. A. Modine, and R. Dingreville, "Re-examining the silicon self-interstitial charge states and defect levels: A density functional theory and bounds analysis study," *AIP Advances*, vol. 10, no. 9, p. 095004, 2020.

[99] R. Jones, B. Coomer, J. P. Goss, B. Hourahine, and A. Resende, "The interaction of hydrogen with deep level defects in silicon," in *Special Defects in Semiconducting Materials*, vol. 71 of *Solid State Phenomena*, pp. 173–248, Trans Tech Publications Ltd, 10 1999.

[100] C. G. Van de Walle, "Energies of various configurations of hydrogen in silicon," *Phys. Rev. B*, vol. 49, pp. 4579–4585, Feb 1994.

[101] C. G. Van de Walle and J. Neugebauer, "Hydrogen in semiconductors," *Annual Review of Materials Research*, vol. 36, no. 1, pp. 179–198, 2006.

[102] N. M. Johnson, C. Herring, and C. G. Van de Walle, "Inverted order of acceptor and donor levels of monatomic hydrogen in silicon," *Phys. Rev. Lett.*, vol. 73, pp. 130–133, Jul 1994.

[103] M. A. Mohammed, J. Melskens, R. Stabile, F. Pagliano, C. Li, W. M. M. Kessels, and O. Raz, "Metastable refractive index manipulation in hydrogenated amorphous silicon for reconfigurable photonics," *Advanced Optical Materials*, vol. 8, no. 6, p. 1901680, 2020.

[104] M. I. J. Probert and M. C. Payne, "Improving the convergence of defect calculations in supercells: An ab initio study of the neutral silicon vacancy," *Phys. Rev. B*, vol. 67, p. 075204, Feb 2003.

[105] M. J. Puska, S. Pöykkö, M. Pesola, and R. M. Nieminen, "Convergence of supercell calculations for point defects in semiconductors: Vacancy in silicon," *Phys. Rev. B*, vol. 58, pp. 1318–1325, Jul 1998.

[106] A. F. Wright, "Density-functional-theory calculations for the silicon vacancy," *Phys. Rev. B*, vol. 74, p. 165116, Oct 2006.

[107] S. Pantelides, *Deep Centers in Semiconductors*. Taylor & Francis, 1992.

[108] J. Newton, A. Chatterjee, R. Harris, and G. Watkins, "Negative-u properties of the lattice vacancy in silicon," *Physica B+C*, vol. 116, no. 1, pp. 219–223, 1983.

[109] R. M. Nieminen, *Supercell Methods for Defect Calculations*, pp. 29–68. Berlin, Heidelberg: Springer Berlin Heidelberg, 2007.

[110] G. D. Watkins, "An epr study of the lattice vacancy in silicon," *J. Phys. Soc. Japan*.

[111] C. Latham, M. Ganchenkova, R. Nieminen, S. Nicolaysen, M. Alatalo, S. Öberg, and P. Briddon, "Electronic structure calculations for substitutional copper and monovacancies in silicon," *Physica Scripta*, vol. 2006, p. 61, 08 2006.

[112] G. D. Watkins and J. R. Troxell, "Negative-u properties for point defects in silicon," *Phys. Rev. Lett.*, vol. 44, pp. 593–596, Mar 1980.

[113] P. M. Fahey, P. B. Griffin, and J. D. Plummer, "Point defects and dopant diffusion in silicon," *Rev. Mod. Phys.*, vol. 61, pp. 289–384, Apr 1989.

[114] P. J. Kelly and R. Car, "Green's-matrix calculation of total energies of point defects in silicon," *Phys. Rev. B*, vol. 45, pp. 6543–6563, Mar 1992.

[115] V. Milman, M. C. Payne, V. Heine, R. J. Needs, J. S. Lin, and M. H. Lee, "Free energy and entropy of diffusion by ab initio molecular dynamics: Alkali ions in silicon," *Phys. Rev. Lett.*, vol. 70, pp. 2928–2931, May 1993.

[116] R. J. Needs, "First-principles calculations of self-interstitial defect structures and diffusion paths in silicon," *Journal of Physics: Condensed Matter*, vol. 11, p. 10437, dec 1999.

[117] T. Nishimatsu, M. Sluiter, H. Mizuseki, Y. Kawazoe, Y. Sato, M. Miyata, and M. Uehara, "Prediction of xps spectra of silicon self-interstitials with the all-electron mixed-basis method," *Physica B: Condensed Matter*, vol. 340-342, pp. 570–574, 2003. Proceedings of the 22nd International Conference on Defects in Semiconductors.

[118] G. D. Watkins, "Intrinsic defects in silicon," *Materials Science in Semiconductor Processing*, vol. 3, no. 4, pp. 227–235, 2000.

[119] P. Rinke, A. Janotti, M. Scheffler, and C. G. Van de Walle, "Defect formation energies without the band-gap problem: Combining density-functional theory and the gw approach for the silicon self-interstitial," *Phys. Rev. Lett.*, vol. 102, p. 026402, Jan 2009.

[120] L. Hedin, "New method for calculating the one-particle green's function with application to the electron-gas problem," *Phys. Rev.*, vol. 139, pp. A796–A823, Aug 1965.

[121] A. R. Meyer, P. C. Taylor, V. LaSalvia, X. Wang, W. Nemeth, M. Page, D. L. Young, S. Agarwal, and P. Stradins, "Atomic structure of defect responsible for light-induced efficiency loss in silicon solar cells in warmer climates," *Cell Reports Physical Science*, vol. 4, no. 1, p. 101201, 2023.

[122] A. R. Peaker, V. P. Markevich, B. Hamilton, G. Parada, A. Dudas, A. Pap, E. Don, B. Lim, J. Schmidt, L. Yu, Y. Yoon, and G. Rozgonyi, "Recombination via point defects and their complexes in solar silicon (phys. status solidi a 10/2012)," *physica status solidi (a)*, vol. 209, no. 10, 2012.

[123] J. Mullins, S. Leonard, V. P. Markevich, I. D. Hawkins, P. Santos, J. Coutinho, A. G. Marinopoulos, J. D. Murphy, M. P. Halsall, and A. R. Peaker, "Recombination via transition metals in solar silicon: The significance of hydrogen–metal reactions and lattice sites of metal atoms," *physica status solidi (a)*, vol. 214, no. 7, p. 1700304, 2017.

[124] M. Shiraishi, J.-U. Sachse, H. Lemke, and J. Weber, "Dlts analysis of nickel–hydrogen complex defects in silicon," *Materials Science and Engineering: B*, vol. 58, no. 1, pp. 130–133, 1999.

[125] R. Jones, S. Öberg, J. Goss, P. R. Briddon, and A. Resende, "Theory of nickel and nickel-hydrogen complexes in silicon," *Phys. Rev. Lett.*, vol. 75, pp. 2734–2737, Oct 1995.

[126] T. M. Gibbons, D. J. Backlund, and S. K. Estreicher, "Cobalt-related defects in silicon," *Journal of Applied Physics*, vol. 121, no. 4, p. 045704, 2017.

[127] A. S. Kale, W. Nemeth, C. L. Perkins, D. Young, A. Marshall, K. Florent, S. K. Kurinec, P. Stradins, and S. Agarwal, "Thermal stability of copper–nickel and copper–nickel silicide contacts for crystalline silicon," *ACS Applied Energy Materials*, vol. 1, no. 6, pp. 2841–2848, 2018.

[128] C. Freysoldt, J. Neugebauer, and C. G. Van de Walle, "Fully ab initio finite-size corrections for charged-defect supercell calculations," *Phys. Rev. Lett.*, vol. 102, p. 016402, Jan 2009.

[129] D. Chen, P. Hamer, M. Kim, C. Chan, A. Ciesla nee Wenham, F. Rougieux, Y. Zhang, M. Abbott, and B. Hallam, "Hydrogen-induced degradation: Explaining the mechanism behind light- and elevated temperature-induced degradation in n- and p-type silicon," *Solar Energy Materials and Solar Cells*, vol. 207, p. 110353, 2020.

[130] B. J. Hallam, P. G. Hamer, S. R. Wenham, M. D. Abbott, A. Sugianto, A. M. Wenham, C. E. Chan, G. Xu, J. Kraiem, J. Degoulange, and R. Einhaus, "Advanced bulk defect passivation for silicon solar cells," *IEEE Journal of Photovoltaics*, vol. 4, no. 1, pp. 88–95, 2014.

Scientific production

Publications

E. Tejeda-Zacarias, P. Baranek and H. Vach, *"First-principles study on the role of silicon point defects on PERC solar cell degradation,"* 2021 IEEE 48th Photovoltaic Specialists Conference (PVSC), 2021, pp. 0809-0813, doi: 10.1109/PVSC43889.2021.
E. Tejeda-Zacarias *"Mécanismes de dégrada on des panneaux solaires induits par la lumière et les hautes températures"* Techniques de l'ingénieur : Caractérisation et propriétés de la matière, 2022, DOI : 10.51257/a-v1-k736

Talks

First-principles study on the role of silicon point defects on PERC solar cell degradation. Tejeda-Zacarias, E., Baranek P. and Vach H. 4th International Conference on Materials Science and Chemistry. March 29-30, 2021. Présenta on orale (webinar).
First-principles study on the role of silicon point defects on PERC solar cell degradation. Tejeda-Zacarias, E., Baranek P. and Vach H. Interna onal 2021 IEEE Photovoltaic Specialists Conference PVSC-48. Miami, Florida, USA. June 20-25, 2021. Oral presentation.
Multi-scale study of light and elevated temperature induced degrada on (LeTID) in silicon based solar cells. Tejeda-Zacarias, E., Baranek P. and Vach H. EuroCORR 2021 Materials science and advanced technologies for beIer corrosion protec on. 19 - 23 September 2021. Virtual event. Oral presentation.

Poster presentations

Preliminary results on the ab initio approach of the silicon aging due to hydrogen degradation linked to the LeTID. Tejeda-Zacarias, E., Baranek P. and Vach H. Physics of Solar Cells: from basic principles to advanced characteriza on. Les Houches, France, 1-6 March 2020
Point defects in crystalline silicon for the study of light and elevated temperature induced degradation in PERC modules. Tejeda-Zacarias, E., Baranek P. and Vach H. MSSC2020 Abinitio Modeling in Solid State Chemistry. London, UK (Virtual Edi on). September 21-25, 2020

List of Figures

List of Tables

ECOLE DOCTORALE

Titre : Compréhension de la dégradation LeTID : une étude DFT des défauts ponctuels dans le silicium.

Mots clés : Photovoltaïque, LeTID, silicium, défauts, modèle DFT

Résumé : Aujourd'hui, les technologies photovoltaïques occupent une place importante sur le marché des énergies renouvelables. En 2020, 3,1 % de la production mondiale d'électricité provient de celles-ci, qui les place comme la troisième source d'électricité renouvelable derrière l'hydroélectricité et l'éolien terrestre. La recherche de modules photovoltaïques à haute performance, basés sur de nouveaux matériaux convertissant la lumière du soleil plus efficacement est une priorité. Néanmoins, une compréhension de la fiabilité et la durée de vie des technologies déjà opérationnelles sont nécessaires pour obtenir des dispositifs plus efficaces notamment avec de moindres pertes. Le silicium est de loin le semi-conducteur le plus utilisé dans les cellules solaires, représentant environ 90% des modules vendus aujourd'hui. L'un des modes de dégradation des cellules à base de Si qui reste à appréhender est la dégradation induite par la lumière et la température élevée (LeTID). Celui-ci peut entraîner une réduction de la production d'électricité des panneaux solaires de 15 % en quelques mois. Ce travail propose un modèle physique basé sur des méthodes théoriques atomiques de type DFT afin d'expliquer les mécanismes à l'origine de cette dégradation. Un tel modèle serait utile pour déterminer des stratégies d'atténuation de ce mode de vieillissement et une méthodologie pour explorer l'impact des impuretés sur les propriétés des matériaux constituant une cellule solaire.

Title : Understanding LeTID degradation: a DFT study of point defects in silicon

Keywords : Photovoltaic, LeTID, silicon,defects, DFT model

Abstract : Nowadays, photovoltaic technologies hold an important place in the renewable energy market. In 2020, 3.1% of global electricity generation came from photovoltaic devices, which placed it as the third-largest renewable electricity technology behind hydropower and onshore wind. In the quest for high-performance photovoltaic modules, the development of new materials that will convert sunlight into electrical power more efficiently is a priority. Nevertheless, an understanding of the reliability and lifetime of already operational technologies is necessary to lead to more efficient devices that present lower losses in the power output. Silicon is by far the most common semiconductor used in solar cells, representing approximately 90% of the modules sold today. One of the degradation modes of silicon solar cells that remains to be understood is light and elevated temperature induced degradation (LeTID). Such degradation can decrease the electricity production of solar panels by up to 15 % in some months. The present work proposes a physical model based on theoretical atomistic methods, based on DFT, to explain the mechanisms behind this degradation. Such a model would be helpful in proving the current mitigation strategies of this aging and in determining a reliable methodology to explore the impact of impurities on the properties of the materials constituting the solar cells.

Institut Polytechnique de Paris
91120 Palaiseau, France